



Institut für Angewandte Physik
der Universität Bonn

Wegelerstraße 8
53115 Bonn

DIRECT SYNTHESIS OF LIGHT POLARIZATION FOR STATE-DEPENDENT TRANSPORT

von
Anna Hambitzer

Masterarbeit in Physik

angefertigt im
Institut für Angewandte Physik

vorgelegt der
Mathematisch-Naturwissenschaftlichen Fakultät
der Rheinischen Friedrich-Wilhelms-Universität
Bonn

Oktober 2012

1. Gutachter: Prof. Dr. D. Meschede
2. Gutachter: Prof. Dr. M. Weitz

Abstract

This master-thesis investigates a new approach for state-dependent transport of atoms in an optical lattice. It is based on a direct synthesis of light polarization by superimposing two circular polarized beams and employing RF sources integrated with acousto-optic modulators for phase control. An interferometrically stable phase between the two beams is achieved by locking them actively with a heterodyne technique.

The influence of polarization crosstalk and erroneous components on the optical lattice and the phase locked loop are investigated and the quality of the phase locked loop is analyzed.

Compared to conventional methods [25] the direct synthesis method avoids the need of an electro-optic modulator, where rotations on the Poincare sphere are limited by the applicable voltage and restrictions on manufacturing and crystal quality exist. Overcoming these limitations it is expected to reach higher polarization purity and larger shift distances in the new design.

Contents

1	Introduction	1
1.1	Motivation	1
1.2	State-Dependent Transport in Optical Lattices	4
1.2.1	Basics of State-Dependent Trapping	4
1.2.2	Scheme Based on an Electro-Optical Modulator	5
1.2.3	Proposal: Scheme Based on Direct Synthesis	7
1.2.4	Phase Stability	9
2	Basics of Phase Locked Loops	14
2.1	Working Principle	14
2.2	Description of Phase Noise	15
2.3	Laplace Transform and Transfer Functions	16
2.4	Servo-Bumps and Loop-Bandwidth	18
2.5	Experimental Setup: Overview	21
2.6	Summary	22
3	Experimental Setup Part I: Orthogonality and Crosstalk	23
3.1	Effect of Non-Orthogonality on the Phase Lock	23
3.1.1	Needed Extinction Ratio for Beam Separation	24
3.1.2	Orthogonality after Combination	25
3.1.3	Distortion of Orthogonality	27
3.2	Estimation of the Effect of Crosstalk on the Optical Lattice	29
3.2.1	Measurement of Quarterwave-Plate Retardance	29
3.2.2	Estimation of the Influence of Crosstalk and Retardance Error on the Optical Lattice	31
4	Experimental Setup Part II: Elements in the Phase Locked Loop	34
4.1	Reference: Direct Digital Synthesizer	34
4.2	Photodetector	36
4.3	Controlled Oscillators: VCO and AOM	38
4.3.1	Working Principle of the AOM	38
4.3.2	Sensitivity Constant of the VCO	38
4.3.3	Modulation Bandwidth of the Oscillators	40
4.3.4	Measurement of the Modulation Bandwidth	41
4.3.5	AOM as Dead Time Element	42
4.4	Phase Frequency Detector	44
4.5	Filter: PID Controller	47
4.6	Summary	49

5	Analysis and Results	50
5.1	Characterisation of the Phase Locked Loop	50
5.1.1	Calculation of the System Transfer Function	50
5.1.2	Method: Step Response Characteristics	52
5.1.3	Step Response Characteristics of a Second Order System	53
5.1.4	Measurement of the Step Response	55
5.1.5	Transfer Functions of the Phase Locked Loop	57
5.2	Resulting Frequency Controllability	60
5.3	Resulting Phase Stability	63
5.3.1	Methods for Phase Noise Measurements	63
5.3.1.1	Phase Noise Measurement with the Signal Spectrum	63
5.3.1.2	Phase Noise Measurement via the PFD output	64
5.3.2	Phase Noise Measurements	66
6	Conclusion and Outlook	71
A	Stitching Phase Noise Spectra for Different Resolution Bandwidth	74

Abbreviations

AOM	Acousto Optical Modulator
DDS	Direct Digital Synthesizer
PLL	Phase Locked Loop
PFD	Phase Frequency Discriminator
VCO	Voltage Controlled Oscillator
\hbar	Planck constant
e	Electron charge
c	Speed of light
ϵ_0	Dielectric constant

Inventory List

DDS	Analog Devices; Model AD9954
AOM	Crystal Technologies; Model 3080-122
PFD	Designed by Professor Marco Prevedelli (Università di Bologna)
PI ² D Controller	Vescent; Model D2-125
VCO	mini circuits; Model ZX95-78+
Amplifier	mini circuits; Model ZHL-1-2W
Photodiode	Thorlabs; Model PDA 10A - EC
Mixer	mini circuits; Model ZLW-6+

1 | Introduction

1.1 | Motivation

Electrons in a solid material are moving in a landscape given by the crystal-structure of the ions. Experimentally, their dynamics are evolving on a femto second time scale, which makes local probing and observation is difficult. Theoretical models with analytical solutions exist mainly for one dimension, while higher dimensional systems need to be calculated numerically [20] and eventually become intractable.

1982 Feynman suggested the *simulation* instead of the calculation of the Hamilton operator that describes the system of interest [11]. This is done by mapping the Hamiltonian on another, which is easier to observe and control. For instance the electrons motion through the attractive and repulsive crystal potentials could be mapped onto a slower evolving system, governed by the same effective potentials.

For quantum simulation the power of neutral atoms in an optical lattice lies in their weak coupling to the environment [40], while the lattice structure, the atom-atom interaction strength and their tunneling rate to neighbouring lattice sites are tunable parameters. In such a cold atom system the superfluid to Mott insulator transition predicted from the Bose-Hubbard model has been observed with single site resolution [36] and recently potassium atoms in a tunable honeycomb lattice have been used to investigate the behaviour of electrons in Graphene [39].

Quantum information processing with neutral atoms as qubits trapped in optical lattices has been suggested by I. H. Deutsch, G. K. Brennen and P. S. Jessen [10]. On a quantum computer problems like the 3D Ising model become feasible [6].

In a neutral atom system a qubit is encoded in the internal (hyperfine) atom state. Large scale entanglement can be achieved by bringing atoms in different internal states into a controlled collision with each other [26]. To realize such a controlled collision a transport of the atoms depending on their internal hyperfine state can be used - a state dependent transport.

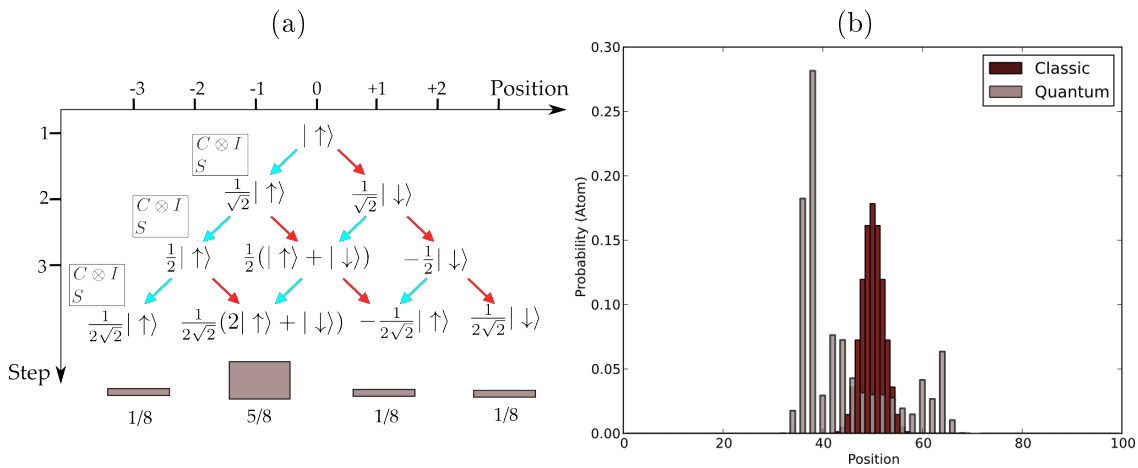
With the ability to transport an atom depending on its internal state one can also experimentally realize a quantum walk [17]. It is defined and motivated as the quantum analogue of the random walk, in which a particle performs a random motion on a graph [1]. The classical random walk is used to describe systems in various fields, such as Brownian motion and stock market prices [17] and it forms the basis of algorithms, e.g. it can be used in Monte Carlo simulations.

To obtain a classical random walk in position space, in each step a coin is flipped and according to the outcome the walker moves to the left or to the right. For a n step random walk this is repeated n times and in the end the probability to find the walker at a certain position is measured.

In the quantum walk, the walker is described by an initial wave function $|\psi_{initial}\rangle$, which has a spatial part that describes the position and a coin part, which describes its internal

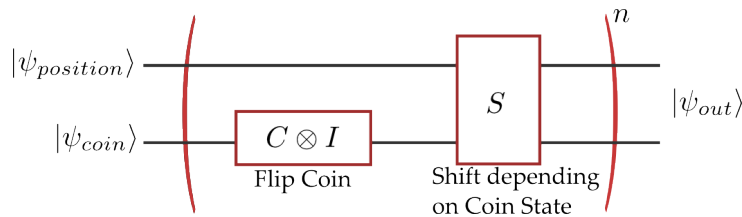
state. Here it is assumed that the internal state can have two values, called $|0\rangle$ and $|1\rangle$. The coin flip is implemented by an operator C . After the coin flip the coin state of the wavefunction is in a superposition of internal states, i.e. of $|0\rangle$ and $|1\rangle$. Applying now a shift operator depending on the internal state will lead to a separation of state $|0\rangle$ and $|1\rangle$. The state after this quantum walk step is described by a new wavefunction (see figure 1.1). Applying the sequence of coin flip and state dependent shift over and over leads to interference of the probabilities. Therefore, the quantum walk obtains its properties from coherence and interference of the walking particle, which creates different distributions compared to a classical random walk after the same number of steps. The exact probability distribution resulting from the quantum walk depends on the initial wavefunction $|\psi_{\text{initial}}\rangle$, the number of steps n and the used coin operator C . An example is shown in figure 1.1.

Figure 1.1 (a): Evolution of an initial wavefunction $|\downarrow\rangle \otimes |0\rangle$ with the Hadamard coin C [19] for three steps. (b): The expected probability distribution for the quantum walk after 20 steps in comparison to a 20 step classic random walk distribution.



The path interference causes the Quantum walk to spread out significantly faster than the classical counterpart [19]. This effect can be used as a general speed up for algorithms based on random walks. The Quantum Walk can be represented as a quantum circuit (see figure 1.2) with a particular output state and a multi-particle quantum walk was shown to be equivalent to a universal quantum computer [5].

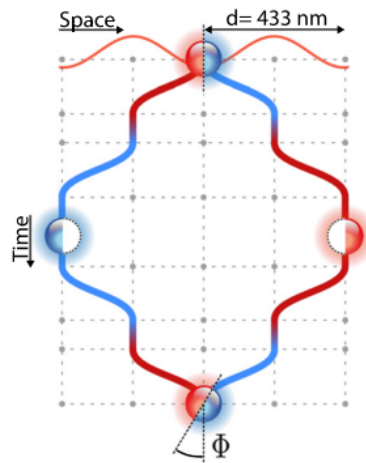
Figure 1.2 Each step in the quantum walk includes a coin operator C which is acting on the coin space and a shift operator S , which shifts the particle depending on its internal state. For a n step quantum walk, this circuit is applied n times to the initial state $|\psi_{\text{initial}}\rangle = |\psi_{\text{position}}\rangle \otimes |\psi_{\text{coin}}\rangle$.



How successful a Quantum Walk can be performed by a system, depends on the preservation of coherence and interference properties of the walker as well as the efficiency and accuracy of coin and shift operator, i.e. the state dependent transport.

Recently a digital atom interferometer has been realized [38]. It uses a single, state dependently shifted atom as an interferometer to probe potential gradients. A basic sequence is illustrated in figure 1.3. The potential gradient between the left and the right path in figure 1.3 leads to the accumulation of a relative phase Φ between them. In case of a linear potential gradient ΔU the accumulated phase rises with enclosed space-time area and therefore with the maximum separation distance and the time before the internal states are transported back to the same position. Therefore, a state dependent transport scheme which can achieve large coherent separations of the internal states would improve the sensitivity of the single atom interferometer.

Figure 1.3 Basic (diamond) sequence in a digital atom interferometer: Initially the atom is brought into a superposition of two internal states. Each of the internal states can be shifted by a state dependent trapping potential. After two shift operations the atom has a distance of 433 nm from its initial position. In this configuration the interferometer is held for a certain time. Potential gradients will lead to a different evolution of the wave function localized on the left compared to the one on the right. The resulting phase difference Φ can be measured by transporting the internal states back to the same position. (The figure is taken from [38].)



1.2 | State-Dependent Transport in Optical Lattices

1.2.1 Basics of State-Dependent Trapping

This section describes how and under which circumstances the confinement of atoms in an optical lattice can be achieved and how an optical lattice can be turned into a state-dependent optical lattice, which is sensitive to the internal state of the trapped atom.

Mechanism for Trapping in an Optical Potential

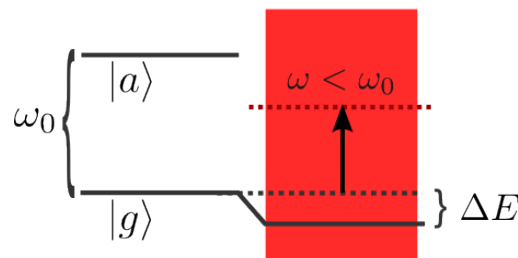
A dilute gas of neutral atoms in an ultrahigh vacuum chamber can be cooled to sub-millikelvin temperatures in a magneto-optical trap as described e.g. in [27].

Subsequently, an attractive optical lattice can be formed by the interference pattern of laser light. The attractive behaviour of the optical lattice can be understood from the Stark-Shift that a two level system experiences in a far off-resonant light field, see figure 1.4. In second order perturbation theory the resulting energy shift of the ground state can be written as

$$\Delta E \sim \frac{|\langle a | \hat{d} \cdot \hat{E} | g \rangle|^2}{\hbar(\omega - \omega_0)},$$

where \hat{d} is the dipole moment of the atom and \hat{E} the electrical light field.

Figure 1.4 The atom is described as a two level system with ground state $|g\rangle$, excited state $|a\rangle$ and a transition frequency ω_0 . Exposition to a far red detuned light field with frequency ω leads to an energy shift ΔE .



There are two possibilities for the shift depending on the detuning. When the frequency is larger than the transition frequency (blue detuned), the level will shift upwards and the atom is repelled from the regions with high intensity. It can be trapped in vacancies of the intensity pattern, as it is used for instance in Donut shaped traps [14].

For frequencies smaller than the transition frequency (red detuned) the energy of the ground state will be lowered, such that the atom is attracted to regions of high intensity. This can be used to align the atoms in the periodic intensity pattern formed in a standing wave.

Mechanism for State Dependent Trapping and Transport

In a state dependent optical lattice internal states of the atom are trapped by different “parts” of the intensity pattern.

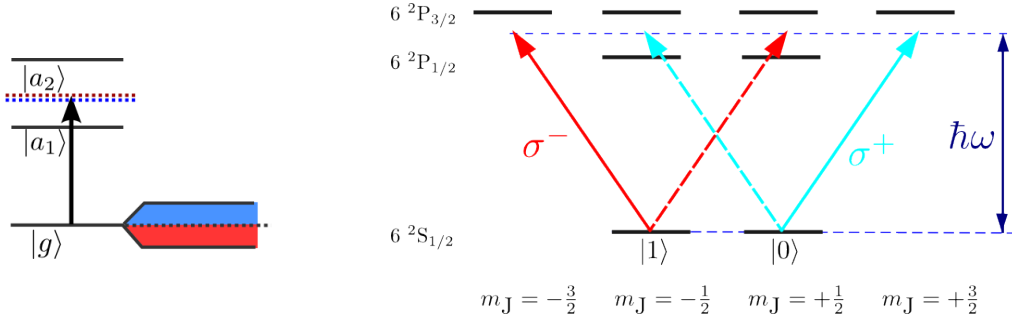
As shown in figure 1.5 for two upper levels the light field will be red detuned with respect to the upper level, causing the ground state energy to shift downwards. This leads to a force which attracts the atom to high intensity regions.

With respect to the lower excited state the laser frequency will be blue detuned, which shifts the level upwards and leads to a repulsive force.

For a certain detuning of the light field from the excited states, the attractive and repulsive force can cancel out and the atom in this state will feel no force at all. The atom won't be trapped by the intensity pattern for such a detuning.

Figure 1.5 Left: For two excited states and a laser frequency lying in between, down- and up-shift of the energy levels can cancel out for a certain wavelength.

Right: The simplified level structure of the $|0\rangle = |F = 4, m_F = 4\rangle$, $|1\rangle = |F = 3, m_F = 3\rangle$ hyperfine state of Cesium can be used for state dependent trapping by left-/right-handed circular polarized light, corresponding to σ^+ , σ^- transitions.



The level structure for certain hyperfine states of Cesium atoms (figure 1.5) leads to a state dependent trapping in the following way:

Circular polarizations σ^+ , σ^- couple levels, which have different magnetic quantum numbers $\Delta m = \pm 1$. One differs between negative circular polarization σ^- ($\Delta m = -1$) and positive circular polarization σ^+ ($\Delta m = +1$).

For state $|1\rangle$ in figure 1.5 the σ^- beam is always creating an attractive potential, since it is red detuned with respect to the excited state $6^2P_{3/2}$.

The σ^+ polarization for state $|1\rangle$ however couples the ground state $|1\rangle$ simultaneously to $6^2P_{3/2}$ and $6^2P_{1/2}$. When the right detuning from these energy levels is chosen, the atom in state $|1\rangle$ won't be trapped by σ^+ polarization.

Then the atom would only be trapped by the σ^- polarized part of the lattice.

By choosing the right frequency – called the characteristic or magic wavelength – it is possible to trap the state $|0\rangle$ by the σ^+ polarization and the state $|1\rangle$ by the σ^- polarization¹.

When a Cesium atom can be brought into one of the hyperfine states $|0\rangle$ or $|1\rangle$ and is exposed to an intensity pattern at a characteristic wavelength of $\lambda_C = 865.9$ nm [18] it is trapped state dependently. State dependent transport is equivalent to a relative displacement of σ^+ to σ^- intensity distribution.

1.2.2 Scheme Based on an Electro-Optical Modulator

A lin- θ -lin polarization configuration means that a standing wave is created by two counter propagating laser beams of linear polarizations with a angle θ relative to each other. This will create circular polarized intensity distributions

$$I_{\sigma^+} \sim \cos^2(kx + \theta/2) \quad I_{\sigma^-} \sim \cos^2(kx - \theta/2), \quad (1.1)$$

for a wavevector $k = 2\pi/\lambda$ at a position x . At a wavelength of $\lambda = 865.9$ nm, each of the internal states $|0\rangle$ and $|1\rangle$ couples to one intensity distribution.

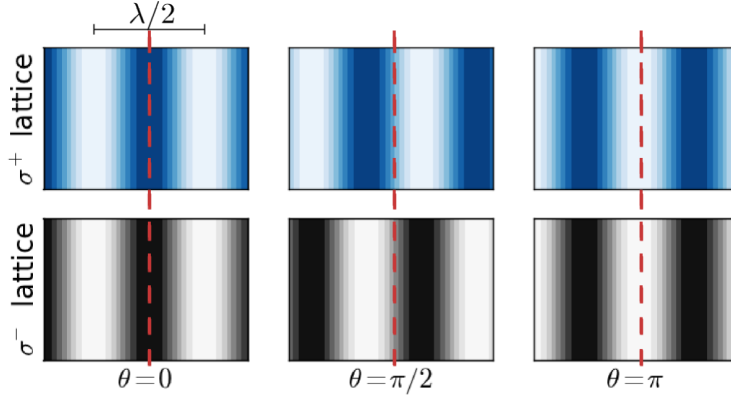
The resulting displacement Δx between the trapping potentials is proportional to the

¹In reality only one ground state will be perfectly trapped by only one polarization and the other one will see a part of the other circular polarization. This will be discussed in section 3.2.

rotation angle θ between the linear polarizations [17]:

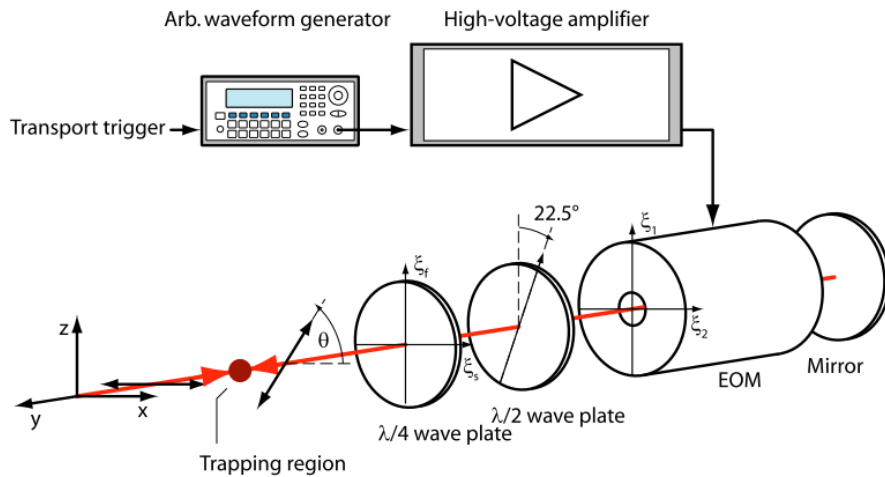
$$\Delta x = \frac{\lambda}{2\pi}\theta. \quad (1.2)$$

Figure 1.6 The intensity maxima in the lin- θ -lin standing wave configuration have a spacing of $\lambda/2$. The intensity distribution of σ^+ and σ^- polarization given by equation 1.1 is plotted for different turning angles θ . For a turning angle $\theta = \pi$ a displacement of one lattice site is reached.



Accordingly, realization of a state-dependent transport is achieved by variation of the rotation angle θ . The rotation of light polarization can be realized by a combination of an electro-optical modulator (EOM) and a quarterwave plate. It contains a nonlinear, electro optical crystal for which the birefringence can be controlled by an electric field. In this way the applied voltage on the EOM will cause a rotation of the polarization direction.

Figure 1.7 A combination of EOM and retardance plates can be used to create a lin- θ -lin standing wave configuration, where the applied voltage controls the rotation angle θ (the figure is taken from reference [18].)



For technical reasons the voltage can only be increased to a certain maximum value, which is approximately the voltage needed for a rotation of the polarization axis of $\theta_{\max} = \pi$. At the maximum voltage the σ^+ and σ^- distribution are overlapped again (see figure 1.6).

This means that an atom which is initially prepared in a superposition of state $|0\rangle$ and $|1\rangle$

will experience a separation of one lattice site at the maximum applicable voltage. Decreasing the turning angle at this moment would lead to bringing the state $|0\rangle$ and state $|1\rangle$ potential back together, while for a quantum walk and a single atom interferometer a larger separation is desired.

To perform transport over several lattice sites experimentally, the roles of $|0\rangle$ and $|1\rangle$ need to be exchanged after each step. This can be achieved by a microwave pulse. The microwave π pulse only transfers the populations with a certain efficiency, which limits the overall transport efficiency [18].

1.2.3 Proposal: Scheme Based on Direct Synthesis

State-dependent transport realized with the EOM-scheme is limited by the efficiency microwave pulse, which needs to be applied in each step of $\lambda/2$ in the state dependent transport.

In a “conveyor belt” [33] configuration atoms are moved in a standing wave as well, but they can be transported over macroscopic distances of one centimeter without application of further microwave pulses.

However, this transport is state independent. This section shows how the idea could be utilized for state dependent transport.

State Independent Transport by a Conveyor Belt

Transport of an atom in a standing wave potential means that the atom is still attracted by the same potential, but in a moving reference frame.

The standing wave in the rest frame is created by two counter propagating waves of same wavevector \vec{k} and frequency ω :

$$E_{\rightarrow} = e^{i(kx - \omega t)} \quad E_{\leftarrow} = e^{i(-kx - \omega t)}.$$

Transformation into a frame moving with velocity \vec{v} , $|\vec{v}| \ll c$ leaves the wavevector invariant $\vec{k}' = \vec{k}$, but the frequency experiences a Doppler shift $\omega' = \vec{k} \cdot \vec{v} + \omega$ [15, page 601].

The counter propagating beams are detuned from their frequency $\omega = 2\pi f_0$ by $2\pi + \Delta f/2$ and $-2\pi\Delta f/2$ respectively. In a reference frame moving with

$$v = \lambda \frac{\Delta f}{2}$$

the Doppler shift compensates the detuning. Once the relative frequency is detuned, the standing wave pattern will keep moving with a speed proportional to the detuning until the frequency of the beams is equalized again.

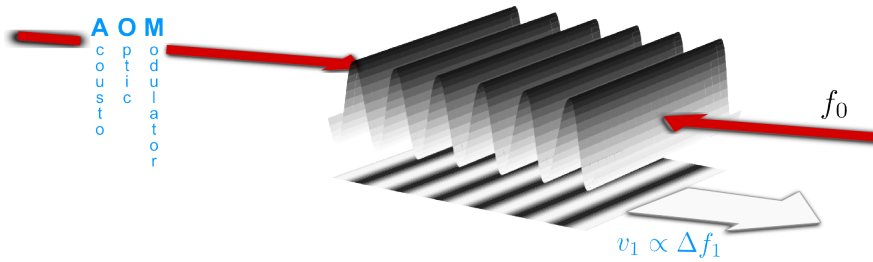
The optical conveyor belt for single neutral Cesium atoms has first been realized in 2001 [33]. A frequency detuning Δf is introduced by an acousto-optical modulator (AOM) (see figure 1.8).

In the state dependent transport realized with the EOM scheme, the typical experimental transportation speed of an atom is

$$v_{typ} \approx \frac{200 \text{ nm}}{10 \text{ } \mu\text{s}} \Leftrightarrow \Delta\nu \approx 50 \text{ kHz}.$$

Acousto-optic modulators operate around a large center frequency which would lead to transportation speeds that are roughly hundred times too large. To achieve a relative

Figure 1.8 An optical conveyor belt is realized by shifting the frequency of one of the counter propagating beams, which create a standing wave with an AOM.

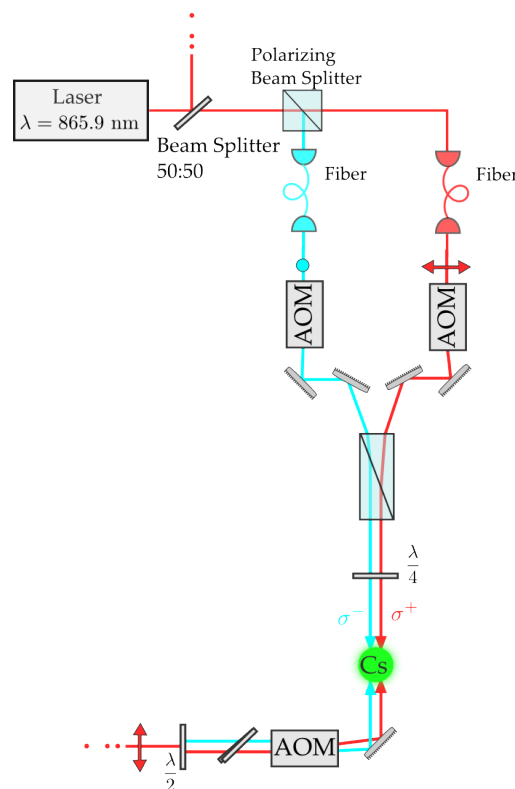


detuning of \sim kHz from the common center frequency an AOM is introduced in each of the counter propagating beams.

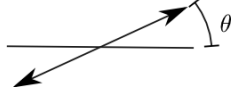
A State Dependent Conveyor Belt

A Cesium atom in hyperfine state $|0\rangle$ ($|1\rangle$) is trapped in a σ^+ (σ^-) polarized potential (section 1.2.1). Thus, to achieve state dependent transport two conveyor belts are needed, one σ^+ and one σ^- polarized (figure 1.9).

Figure 1.9 A state dependent conveyor belt consists of two spatially overlapped conveyor belts of orthogonal circular polarization at the characteristic (or magic) wavelength for the Cesium (Cs) atoms. Half of the intensity is coupled out with a 50:50 beam splitter for the counter propagating linear polarized beam. The other half is split again into orthogonal linear polarizations by a polarizing beam splitter and mode cleaned by optical fibers. Frequency and phase of the linear polarizations are controlled by two separate AOMs before they are recombined again. With a quarterwave plate the vertical \bullet -linear polarization (horizontal \leftrightarrow) is converted to circular σ^- (σ^+) polarization.



In the EOM scheme the state dependent transport is achieved by rotation of the linear polarization of one of the counter propagating beams. The decomposition of a rotated linear polarization $\vec{e}_{\text{lin}, \theta}$ into the circular basis states² $\vec{e}_{\sigma+}$, $\vec{e}_{\sigma-}$ shows that the scheme based on overlapped circular polarized conveyor belts is equivalent to the EOM scheme:



$$\vec{e}_{\text{lin}, \theta} = \begin{pmatrix} \cos \theta \\ \sin \theta \end{pmatrix} = \frac{1}{2} \begin{pmatrix} e^{-i\theta} + e^{i\theta} \\ i(e^{-i\theta} - e^{i\theta}) \end{pmatrix} = \frac{1}{\sqrt{2}} \left(e^{-i\theta} \vec{e}_{\sigma+} + e^{i\theta} \vec{e}_{\sigma-} \right).$$

Superimposing two circular waves with constant phase relation and balanced intensity creates linear polarization. The relative phase $\Delta\phi$ between the circular polarizations determines the rotation angle θ of this linear polarization:

$$\vec{e}_{\text{lin}, \theta} = \frac{1}{\sqrt{2}} \left(e^{i\Delta\phi} \vec{e}_{\sigma+} + \vec{e}_{\sigma-} \right), \text{ where } \theta = \frac{\Delta\phi}{2}. \quad (1.3)$$

The relative phase of the circular polarized beams composing the state dependent conveyor belt determines the rotation angle θ and therefore the transport distance $\Delta x \propto \theta$ (equation 1.2, page 6) A frequency detuning Δf in one of the circular polarized standing waves is equivalent to a relative phase

$$\Delta\phi(t) \propto \int_0^t \Delta\Delta f d\tau = \Delta f t.$$

Therefore, once the frequency is detuned the composed linear polarization will rotate with a speed proportional to the frequency detuning, equivalent to a state dependent transport over several lattice sites.

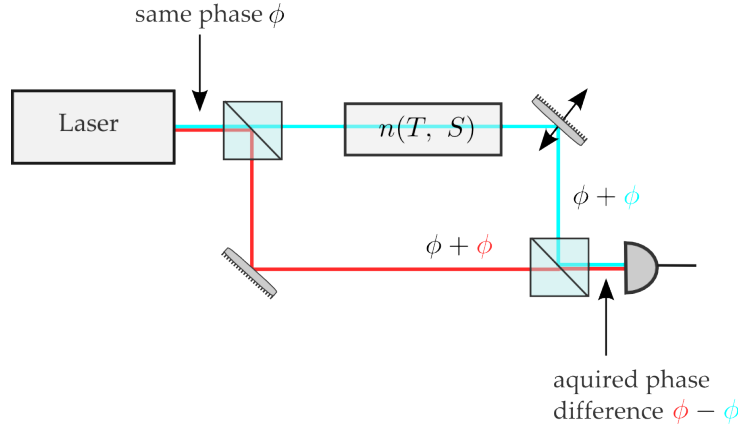
1.2.4 Phase Stability

The difficulty in the proposed state-dependent conveyor belt scheme is the phase stability. Generally, an interferometer is sensitive to temperature fluctuations and vibrations (see figure 1.10).

²In the Jones formalism the circular polarization basis vectors are given by

$$\vec{e}_{\sigma+} = \frac{1}{\sqrt{2}} \begin{pmatrix} 1 \\ i \end{pmatrix}, \quad \vec{e}_{\sigma-} = \frac{1}{\sqrt{2}} \begin{pmatrix} 1 \\ -i \end{pmatrix}$$

Figure 1.10 Beams propagating in different arms of an interferometer (here of Mach-Zehnder type) acquire a relative phase difference due to changes in the optical path length. The phase difference arises from vibrations and the dependence of refractive indices on stress and temperature variations.



This lead already to a disturbance in the interferometer experiment of Michelson-Morley by passing horse traffic [12].

Fluctuations in the relative phase will arise from coupling of vibrations into the optical elements and changes of refractive indices along the optical path by e.g. temperature variations or stress. In particular optical fibers, which are often used to clean the mode profile of the lattice beams are sensitive to temperature and stress [24], as both induce a change in the refraction index.

The upper part of the conveyor belt scheme for state-dependent transport in figure 1.9 can be seen as a Mach-Zehnder type interferometer. The fluctuating relative phase $\Delta\phi$ between the two arms will lead to a change of the rotation angle θ of the resulting linear polarization (see equation 1.3).

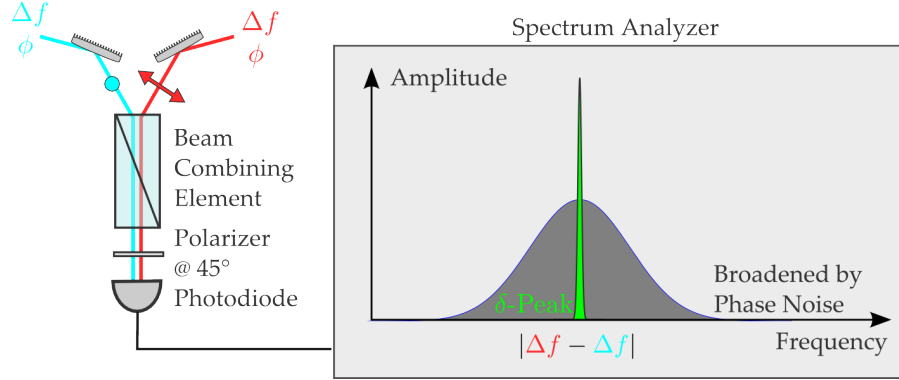
Magnitude and spectral distribution of the relative phase fluctuations can be measured by recording the beat signal of the two beams on a spectrum analyzer (figure 1.11). The polarizer projects the orthogonal linear polarizations on a common axis. This leads to an intensity

$$I(t) \propto \cos(\Delta f t + \Delta\phi(t))$$

on a photodiode, where Δf and $\Delta\phi(t)$ are the frequency and phase difference of the two beams. A spectrum analyzer is used to display the spectral distribution of the intensity $I(t)$. Without phase noise ($\Delta\phi(t) = 0$), the spectral distribution would be the Fourier transform of $\cos(\Delta f t) = \delta(\Delta f)$, i.e. a sharp peak –called the carrier– at the frequency difference.

The phase noise term $\Delta\phi(t)$ will lead to a modulation of this signal and therefore broaden the observed spectrum as indicated in figure 1.11. A sharp spectral feature appears at the carrier frequency with a broadened part caused by the relative phase noise.

Figure 1.11 For the state-dependent conveyor belt setup the relative phase fluctuations can be measured by driving both AOMs in figure 1.9 with stable RF signals. On a spectrum analyzer a beat signal at their frequency difference is observable. Without phase noise a δ -peak at this frequency would be expected and the relative phase noise between the arms leads to a spectral broadening into the grey shape.



For an interferometer on an optical table – under the influence of vibration, temperature fluctuations and stress – the typical rms phase noise between the two interferometer arms is 10° to 15° [22]. The fluctuation in the relative phase of σ^+ and σ^- polarization leads to a relative displacement of their intensity distributions.

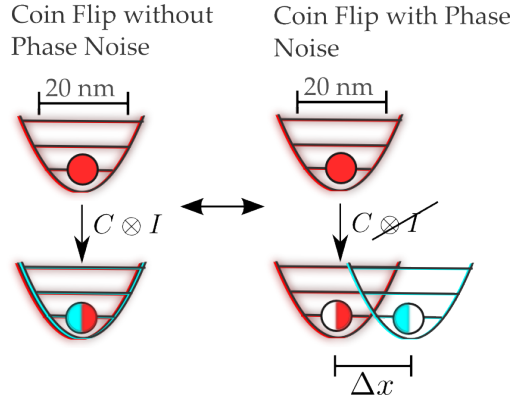
Excitation due to Potential Displacement

For a rms phase noise between σ^+ and σ^- polarization of $10^\circ \dots 15^\circ$ the relative rms position fluctuations of the resulting intensity distributions are $\Delta x = 10 \text{ nm} \dots 18 \text{ nm}$.

This value has to be compared with the spatial extension of the atoms, described by their wave function. The situation of their confinement in the intensity maxima of the standing wave potential can be approximated by a harmonic oscillator potential. The mean population is in of the lowest vibrational states $\bar{n} = 1.2$ [18] and the confinement is described by the trapping frequency $\omega \approx 2\pi \times 120 \text{ kHz}$ [17]. This results a size of 20 nm for the ground state wavefunction.

The coin operation, which should only act on the internal states of the atoms, will actually lead to a shifting term as well, which describes the displacement of the σ^+ and σ^- potentials.

Figure 1.12 A coin flip $C \otimes I$ brings the internal states into a superposition and should leave the spatial part of the wave function unaffected. With displaced potentials due to phase noise the coin flip will no longer be described by a unity action I on the spatial part of the wavefunction.



After the coin flip the atom in motional state $|1\rangle$ will see a displaced harmonic oscillator potential, see figure 1.12. The probability to end in one of the vibrational states in the second, displaced potential can be calculated as the spatial overlap of the initial wave function $|1\rangle$ with the displaced eigenfunctions $|m\rangle$ of the second harmonic oscillator potential [13]. The eigenfunctions displaced by Δx can be written as $\langle m|e^{i\hat{p}\Delta x/\hbar}$, where the momentum operator of the harmonic oscillator is $\hat{p} = i\sqrt{\frac{m\omega\hbar}{2}}(\hat{a}^\dagger - \hat{a})$. Then the overlap with the initial state is given as

$$\langle m|e^{i\hat{p}\Delta x/\hbar}|1\rangle = \langle m|e^{-\frac{1}{\hbar}\sqrt{\frac{m\omega\hbar}{2}}(\hat{a}^\dagger - \hat{a})\Delta x}|1\rangle = \langle m|e^{\alpha(\hat{a}^\dagger - \hat{a})}|1\rangle,$$

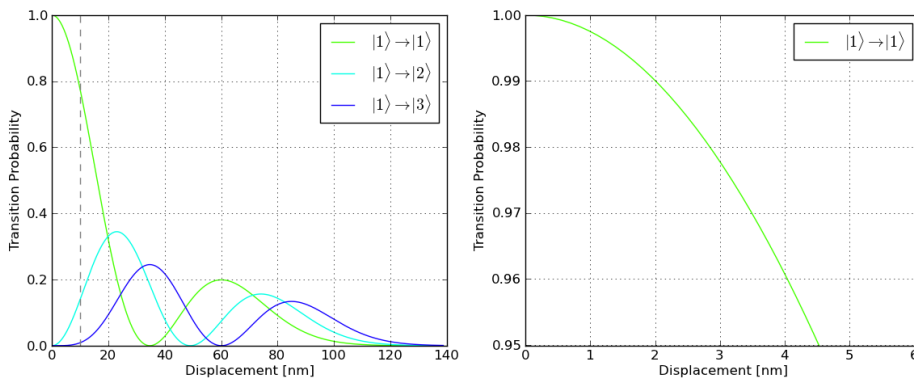
with a parameter $\alpha = \sqrt{\frac{m\omega}{2\hbar}}\Delta x$. This can be solved analytically (e.g. [13, 43]) and the result is known as the Franck-Condon factor

$$\langle m \geq 1|e^{i\hat{p}\Delta x/\hbar}|n = 1\rangle = \sqrt{\frac{n!}{m!}}\alpha^{m-n}e^{-\frac{1}{2}\alpha^2}\mathcal{L}_n^{m-n}(\alpha^2),$$

where \mathcal{L}_n^{m-n} are the generalized Laguerre polynomials.

The excitation probability for the displaced harmonic operator potential is shown in figure 1.13.

Figure 1.13 Excitation probability for a displaced harmonic oscillator potential after the coin shift.



For a displacement of 10 nm the probability to end up in one of the excited states in the second harmonic oscillator potential is about 23 %. The interference ability of the atoms is lost after such an excitation, since the orthogonal eigenfunctions of the harmonic oscillator will not be able to interfere in the subsequent steps. For the excitation probability to be smaller than 99 % an estimated phase stability of $\langle\phi\rangle \approx 1.7^\circ$ equivalent to a relative position fluctuation of $\langle\Delta x\rangle \approx 2$ nm is needed.

The relative phase stability between the interferometer arms for the state-dependent conveyor belt can be improved by a phase locked loop, which is described in the next chapter.

2 | Basics of Phase Locked Loops

To achieve a relative phase stability a phase locked loop will be used. This chapter gives an overview of its working principle and how it can be described by transfer functions in the frequency domain. It is based on the descriptions in [23, 29]

2.1 | Working Principle

Aim of the phase locked loop (PLL) is the stabilization (locking) of an oscillator phase to a reference phase. In a minimal PLL always fulfil four basic functions:

- Reference
- (Controlled) Oscillator
- Phase Detector
- Filter.

A part of the oscillator signal is used to extract the phase information of the oscillator. This part is fed back and compared to the reference phase by the phase detector..

The output of the Phase Detector can be a voltage signal which is connected to the phase difference by a characteristic phase detector constant.

This error signal can be used to change the oscillator phase in the desired way, such that the difference between oscillator and reference phase is minimized. Usually the raw output of the phase detector is not suitable to directly control the oscillator in the desired direction. To obtain a control signal which is fitting to the used oscillator, the error signal created by the phase detector is processed by a filter. A simple filter would be an amplifier, which will simply adjust the amplitude of the error signal, so that it can control the oscillator.

Subsequently the PLL changes the oscillator signal and in an ideal case the controlled oscillator will be stabilized (locked) to the reference.

Once the controlled oscillator is locked, the phases of oscillator and reference have a fixed difference, which is kept constant by the PLL. The residual fluctuations of the oscillator around the reference phase describe the quality of the phase lock.

Since frequency is the derivative of the phase, a fixed phase ratio will imply that the frequencies are proportional to each other as well. Therefore, a phase lock implies a frequency lock.

On the other hand, since the phase is the integral of frequency over time, a frequency lock is not equivalent to being a phase lock.

When the oscillator shows a residual frequency fluctuation around the main frequency in the lock, it can oscillate e.g. faster for a period of time and then return again to the

main frequency. The accumulated phase in this time will be different from the one, that would have been accumulated for running only at the main frequency. Therefore, the phase relation between reference and controlled oscillator has changed, the phase lock is lost at this point.

This leads to a distinctive spectral shape of a phase locked signal with a sharp carrier of a spectral width below 1 Hz.

In the case that the oscillator is locked to the reference, a change in the reference phase should result in a change of the oscillator phase. Since frequency and phase are connected via

$$f = \frac{d\phi}{dt}.$$

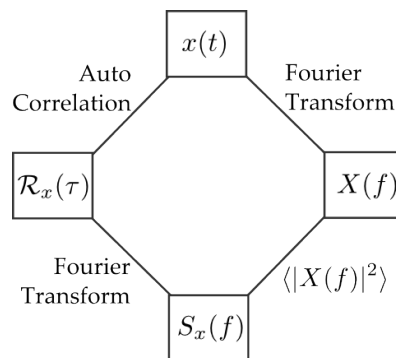
This relation can be used to scan the reference frequency or phase and change the oscillators phase or frequency in the same way. Their phases will stay locked during this process, if the loop can track the changes in the reference and adjust the oscillator behaviour fast enough.

2.2 | Description of Phase Noise

The standard deviation is divergent for noise types which are typically encountered in oscillators with high precision [3]. Furthermore, stationary noise processes $x(t)$ cannot be described in the frequency domain by a Fourier transform, since they are invariant under translation in time and the Fourier transform is only defined for square integrable functions.

The solution is to use the Allan deviation [3] in the time domain or the power spectral density $S_x(f)$ obtained with the Wiener Khinchin theorem in the frequency domain.

Figure 2.1 The Wiener Khinchin theorem can be used to obtain the power spectral density for stationary random processes $x(t)$ for which the Fourier transform is not defined. It connects the power spectral density with the autocorrelation function.

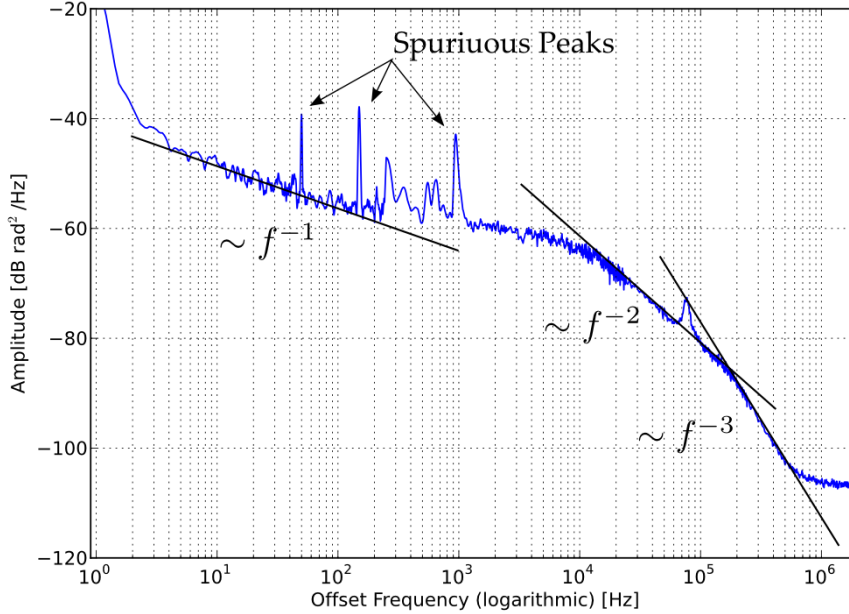


The random phase noise can be described by a power law in the frequency behaviour

$$S_\phi(f) \sim f^\alpha, \tag{2.1}$$

where α can take values from typically $[-3,3]$ [32]. A typical phase noise spectrum with the approximation by a power law is shown in figure 2.2.

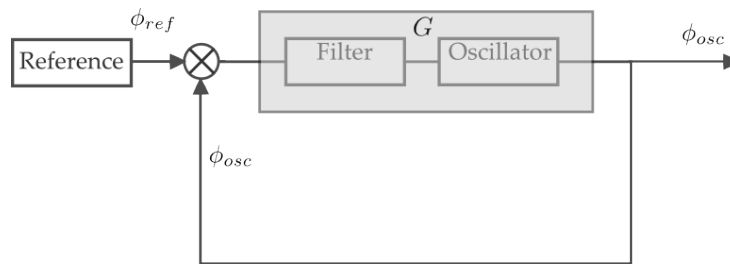
Figure 2.2 A typical random phase noise spectrum $S_\phi(f)$ can be approximated by a power law according to equation 2.1. Additionally the presence of spurious peaks indicates the presence of strong noise sources at this frequencies (e.g. here the presence of power supplies is indicated by a spurious peak at 50 Hz).



2.3 | Laplace Transform and Transfer Functions

In figure 2.3 the layout for the phase locked loop is shown in an equivalent circuit diagram, where the filter and the oscillator have been replaced by a black box G . The following description is adapted from [23, 29].

Figure 2.3 Equivalent circuit diagram of a PLL, where the action of filter and oscillator are described by a function G .



The phase locked loop minimizes the error $\Delta\phi$ between reference and controlled oscillator,

controlled oscillator: ϕ_{osc} reference oscillator: ϕ_{ref} phase error: $\Delta\phi = \phi_{ref} - \phi_{osc}$.

A part of the output signal ϕ_{osc} is used to compare it to the reference signal ϕ_{ref} . The function describing the black box will determine the new output signal. Therefore, the output signal ϕ_{osc} at a time t will depend on the error signal $\Delta\phi$ at a former time $t - \tau$. How strong the influence of $\Delta\phi(t - \tau)$ on the new output signal $\phi_{osc}(t)$ is, is described by the function $G(\tau)$

$$\phi_{osc}(t) = \int_0^t G(\tau)\Delta\phi(t - \tau). \quad (2.2)$$

Therefore the system is described by a convolution in the time domain.

For two reasons it is more convenient to describe the convolution in the frequency domain than the time domain: The initial and resulting phase noise are measured as a power spectral density $S_\phi(f)$. Furthermore, the convolution in the time domain corresponds to a simple multiplication in the frequency domain.

The goal is to describe the behaviour of the system under different circumstances, for example sudden changes in the reference signal. These sudden changes cause certain systems to become unstable which results in a non-zero error $\Delta\phi$. Since the Fourier transform is only defined for signals that drop to zero as $t \rightarrow \infty$, the description in the frequency domain has to take into account such possible unstable behaviour.

This is done by multiplying every signal $f(t)$ with an exponentially decaying part $e^{-\delta t}$ to ensure convergence to zero at infinite time. The Fourier transform of the modified function $f(t)e^{-\delta t}$ is a Laplace transform

$$\mathcal{L}\{f(t)\} = \int_{-\infty}^{\infty} f(t)e^{-st} dt, \quad \text{where } s = \delta + i\omega.$$

With the description in the Laplace domain the oscillator phase and the phase difference are no longer connected by the convolution as described in equation 2.2. They are connected by

$$\phi_{osc}(s) = G(s) \cdot \Delta\phi(s) \quad \Leftrightarrow \quad G(s) = \frac{\phi_{osc}(s)}{\Delta\phi(s)}.$$

The function $G(s)$ is known as the open loop gain. It provides a formal gathering of the transfer functions of the filter action, –possibly more than one– voltage controlled oscillator and other elements within the black box in figure 2.3.

To characterize the PLL it is necessary to know the reaction of the phase locked loop to a change in the reference signal, i.e. the dependence of ϕ_{osc} on ϕ_{ref} and how well an error $\Delta\phi$ can be compensated by the loop. The dependence of the oscillator phase ϕ_{osc} on the reference phase ϕ_{ref} is described by the system transfer function $H(s)$

$$H(s) = \frac{\phi_{osc}(s)}{\phi_{ref}(s)} = \frac{\phi_{osc}}{\Delta\phi + \phi_{osc}} = \frac{G(s)}{1 + G(s)},$$

and the dependence of the phase error $\Delta\phi$ on the reference phase ϕ_{ref} by the error transfer function $E(s)$

$$E(s) = \frac{\Delta\phi(s)}{\phi_{ref}(s)} = \frac{\Delta\phi}{\Delta\phi + \phi_{osc}} = \frac{1}{1 + G(s)}.$$

The ideal case is described by $H(s) = 1$, which means that the phases of reference ϕ_{ref} and controlled oscillator ϕ_{osc} are exactly the same. Then the error $\Delta\phi$ between them is zero, therefore in this case $E(s) = 0$.

2.4 | Servo-Bumps and Loop-Bandwidth

The phase locked loop can not react infinitely fast to a change in the reference signal, since all components have a limited modulation bandwidth and response time. A fast changing signal means a contribution of high frequencies in the Laplace transform. In the case of a fast changing input the error $\Delta\phi(s)$ can not be adjusted immediately.

Mathematically $H(s)$ and $E(s)$ are determined by the dependence on the open loop gain $G(s)$. Both have a pole at $1 + G(s) = 0$, i.e. where the absolute value $|G(s)| = 1$ and the argument $\angle(G(s)) = 180^\circ$ ($e^{-i\pi} = -1$). Divergence of the transfer functions that describes the loop leads to instability of the system. As a measure of system stability the *phase margin* is defined as the difference of $\angle(G(s))$ to -180° at the point of unity gain $|G(s)| = 1$ [23, 29].

For $|1 + G(s)| < 1$ the system can still be stable but loses its ability to follow the reference properly. Therefore controlled oscillator phase and reference phase differ when this condition is met. Therefore, the system transfer function $H(s)$ will drop from unity, while the error transfer function rises $E(s) > 0$ for large s . This is reminiscent of the behaviour of a low- and a high-pass filter when the cut-off frequency is approached.

Following the suggestions of [31, eq. 23] the following form of $G(s)$ is used as an example

$$G(s) = \frac{2\pi f_{\text{bw}}}{s} e^{-sT_{\text{delay}}} \cdot K. \quad (2.3)$$

K is a linear gain constant, which could be for example an amplifier for the error voltage acting as a filter. Usually every element will have a finite bandwidth f_{bw} . Additionally a delay line can occur, e.g. a long cable. The delay results in an additional phase factor of $e^{-i2\pi f T_{\text{delay}}} = e^{-sT_{\text{delay}}}$ of the signal.

Assumed is that the reference oscillator shows stable spectrum $S_{\phi_{\text{ref}}}$, in which phase noise is suppressed up to a high degree. This can be taken into account as rapidly decaying phase noise, described by large negative powers $\alpha = -2$ and $\alpha = -3$ in equation 2.1 (page 15)

$$S_{\phi_{\text{ref}}}(f) \propto f^{-2} + f^{-3}.$$

The phase locked loop aims to minimize the difference spectrum of $\Delta\phi(s)$ to the reference spectrum $S_{\phi_{\text{ref}}}(f)$. The connection between the reference spectrum and the difference of the oscillator to the reference is given by the error transfer function

$$E(s) = \frac{\Delta\phi(s)}{\phi_{\text{ref}}(s)} \Rightarrow S_{\Delta\phi}(f) = |E(2\pi if)|^2 S_{\phi_{\text{ref}}}(f).$$

The observed oscillator spectrum is $S_{\phi_{\text{osc}}}(f) = S_{\Delta\phi}(f) + S_{\phi_{\text{ref}}}(f)$.

Equation 2.3 contains bandwidth f_{bw} and delay time T_{delay} as parameters. Arbitrary values for the bandwidth ($f_{\text{bw}} = 2.5$ MHz) and for the delay time ($T_{\text{delay}} = 600$ ns) are chosen. Now that the reference phase noise spectrum $S_{\phi_{\text{ref}}}(f)$ and the open-loop transfer function are given for this example system, its transfer functions can be calculated.

A plot of the resulting system transfer functions $H(s)$ and $E(s)$ reveals that their Bode plot looks reminiscent to the ones of a low and a high pass filter (figure 2.4).

Figure 2.4 The system transfer function $H(s)$ and error transfer function $E(s)$ are shown for $G(s)$ given by equation 2.3 for different amplification factors K .

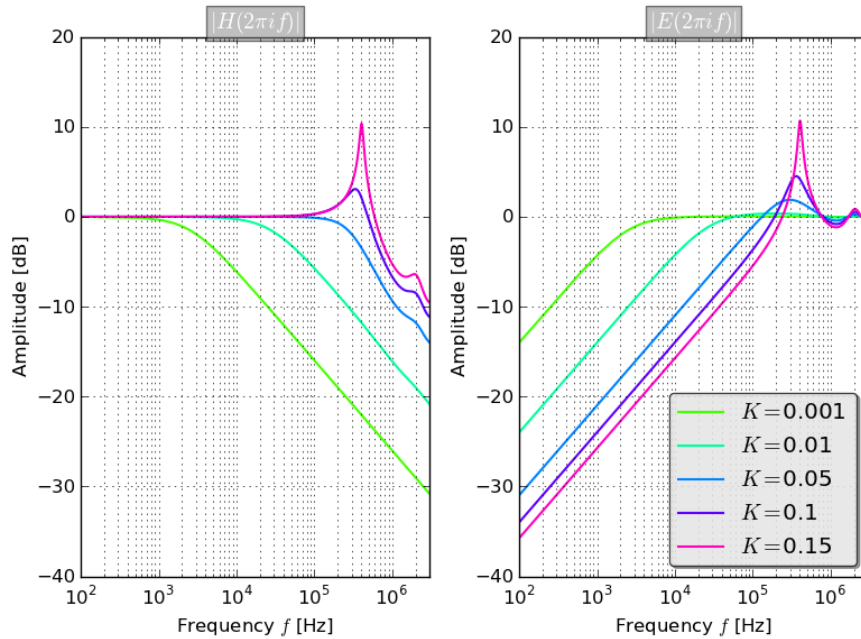
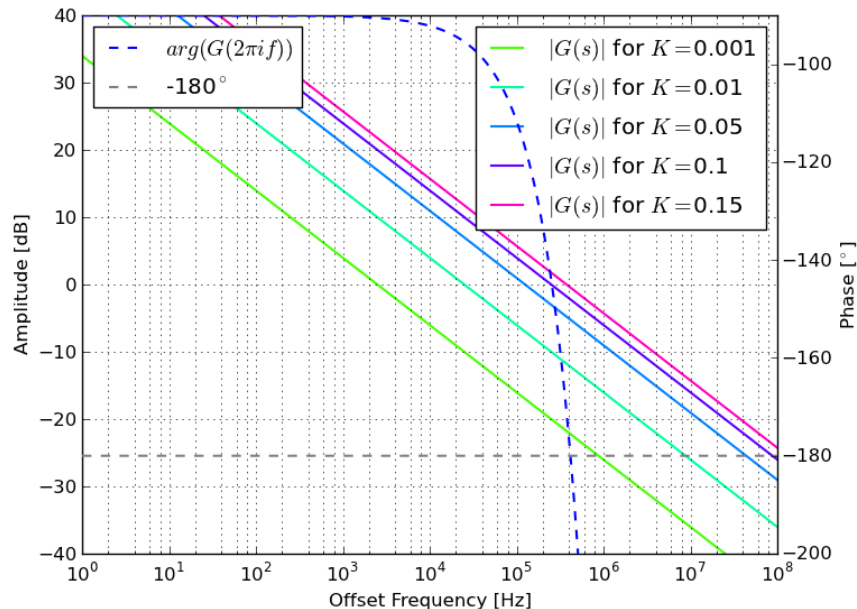


Figure 2.5 Open-loop gain $G(s)$ as given by equation 2.3 for different amplification factors K . The phase $\arg(G(s))$ is the same for different amplification factors, since these only change the absolute value $|G(s)|$.



A very small linear gain K results in a small feedback. In this case error transfer function will be close to unity, which indicates a large error $\Delta\phi$.

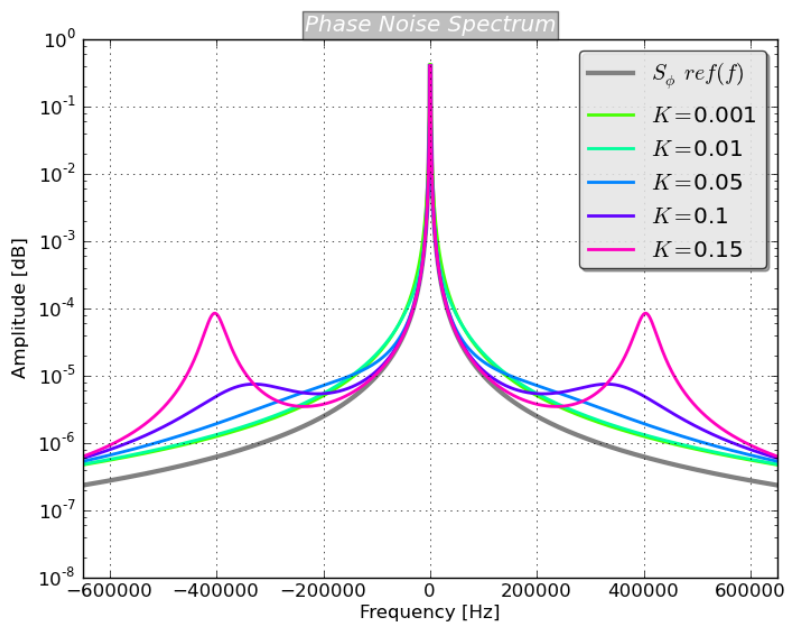
Increasing the linear gain K leads to a suppression of difference to the reference signal in the center region up to about 900 kHz. In the outer region of the spectrum the influence of the delay line becomes visible: The delay leads to an offset frequency dependent additional

phase $\phi_{add} = -2\pi f_{\text{offset}} T_{\text{delay}}$. When an additional phase of $-\pi/2$ is gained, the system starts to enhance phase noise since then the sign of $G(s)$ becomes -1 and a servo bump arises. In this example this would lead to

$$\phi_{add} = -\frac{\pi}{2} = -2\pi f T_{\text{delay}} \Leftrightarrow f = \frac{1}{4T_{\text{delay}}} \approx 420 \text{ kHz.}$$

Whether the system becomes unstable depends on the absolute value $|G(s)|$. In case $|G(s)| = 1$ the servo bump starts to diverge.

Figure 2.6 The phase locked oscillator spectrum will show the typical shape of a sharp carrier at the reference frequency (here chosen as the center frequency) and servo bumps appearing at an offset frequency depending on the open-loop transfer function $G(s)$.



2.5 | Experimental Setup: Overview

Each conveyor belt is composed of two counter propagating beams which create a standing wave of the desired polarization at the position of the ultra cold ^{133}Cs cesium atoms in vacuum. Circular polarization σ^+ (σ^-) is created by a Quarter wave plate $\frac{\lambda}{4}$ from orthogonal linear polarizations \leftrightarrow (\bullet). Each lattice beam contains an AOM which implements relative frequency differences between the beams.

Splitting and recombination is done in a Mach Zehnder interferometer. Phase noise which leads to position fluctuations of the conveyor belts is accumulated in the separate optical paths of the orthogonal linear polarizations before they are overlapped again. After the recombination further phase shifts by optical path variations will be the same for both beams and therefore don't change the relative position. To obtain the relative phase informations $|\varphi_{\leftrightarrow} - \varphi_{\bullet}|$ a beam splitter is used to couple out a small part after combination.

The error signals are beat signals of the respective linear polarization with a part of the counter propagating beam. Each of them contains the information of relative phase changes to the counter propagating beam ϕ_{cp} :

$$PD_{\leftrightarrow} \sim |\phi_{\leftrightarrow} - \phi_{cp}| \quad PD_{\bullet} \sim |\phi_{\bullet} - \phi_{cp}|.$$

The phase locked loop stabilizes each of the signals to an electronic phase stable reference ϕ_{ref} . The feedback is given to the respective AOM driver, so that AOM driver and AOM behave as the controlled oscillator. By changing the phase of polarizations \bullet , \leftrightarrow the differences $|\phi_{\bullet} - \phi_{cp}|$ and $|\phi_{\leftrightarrow} - \phi_{cp}|$ are stabilized to the respective stable reference spectrum

$$|\phi_{\bullet} - \phi_{cp}| \xrightarrow{\text{stabilized to}} \phi_{ref, \bullet} \quad |\phi_{\leftrightarrow} - \phi_{cp}| \xrightarrow{\text{stabilized to}} \phi_{ref, \leftrightarrow}. \quad (2.4)$$

To obtain relative phase stability between the two arms, the references have to be phase stable to each other as well. This is suggested by the common clock signal.

$$\phi_{ref, \bullet} \xleftrightarrow{\text{stable to}} \phi_{ref, \leftrightarrow}. \quad (2.5)$$

Every optical element will only be operating within a certain error range. The size of this error will affect the phase locked loop and the quality of the resulting optical lattice.

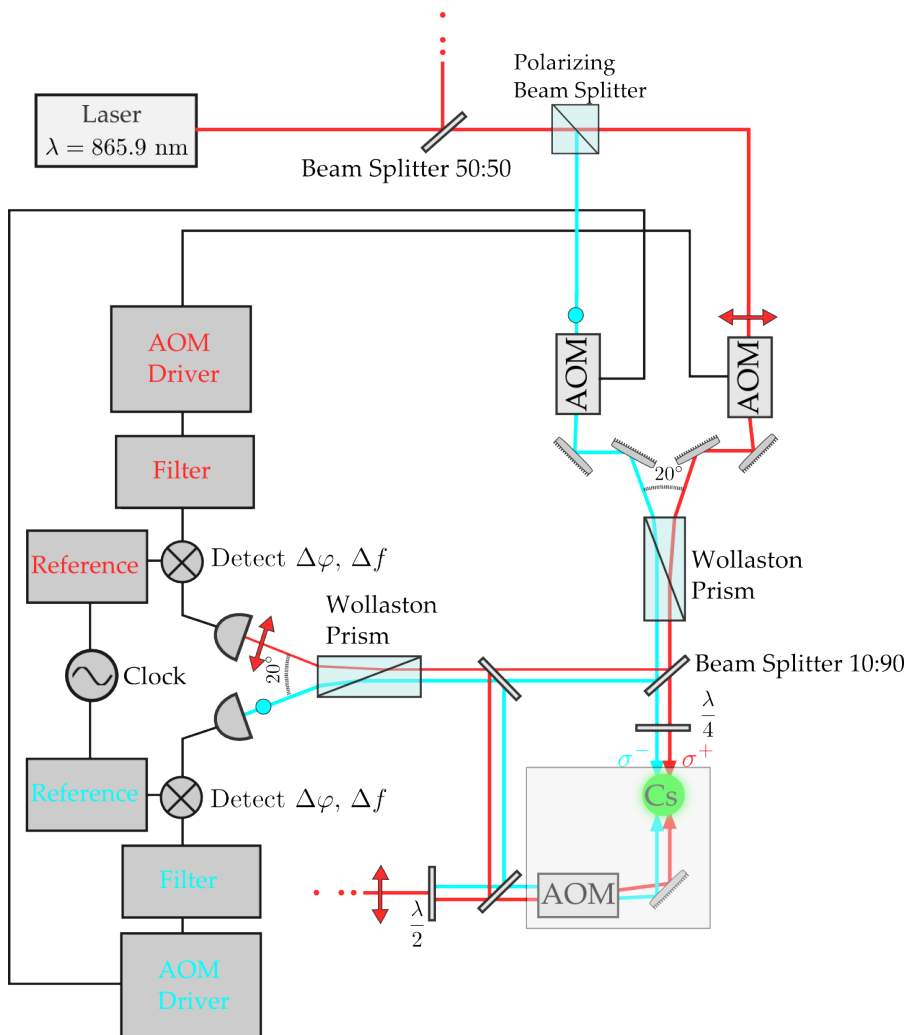
The PLL error signal and the optical lattice which could be created as shown in figure 2.7 rely on

- Orthogonality of the linear \bullet - and \leftrightarrow -polarization after their recombination
- The ability to separate the orthogonal linear polarizations again for the error signal
- A Quarterwave plate which can create σ^+ and σ^- polarization with an acceptable error.

In section 3.1 the error signal creation regarding the crosstalk is discussed. The retardance error of the Quarterwave plate and its influence on the created lattice are discussed in section 3.2.

The dynamic behaviour, i.e. its ability to stabilize and control the phases in equations 2.4 and 2.5 of the loop will be determined by the transfer function of each component in the phase locked loop. They are discussed in chapter 4.

Figure 2.7 The proposed scheme from figure 1.9 extended by the components of two phase locked loops, which stabilize each circular polarization.



2.6 | Summary

The proposed scheme (section 1.2.3) for state-dependent transport relies on two independent conveyor belts, each controlled by one AOM. This configuration is not phase stable (section 1.2.4) and the initial relative phase noise between the channels is $\langle \phi^2 \rangle \approx 10^\circ$, corresponding to relative position fluctuations of 10 nm between the conveyor belts. This will lead to an imperfect overlap of the ground state wave functions of the atoms, which have a width of 20 nm. Experiments like the quantum walk or a single atom interferometer require a phase stability of better than $\langle \varphi \rangle_{rms} < 1.7^\circ$ (section 1.2.4).

As a possible way to stabilize the phase of an oscillator to a reference signal the phase locked loop and its description by transfer functions $G(s)$, $H(s)$ and $E(s)$ is introduced. The power spectral density $S_\phi(f)$ is used to measure phase noise in the frequency domain and the expected spectrum including the appearance of servo-bumps in the oscillator phase noise spectrum in lock is shown by calculation of an example.

The result is the setup for a state-dependent conveyor belt extended by the components needed for the relative stabilization of the circular polarizations shown in figure 2.7.

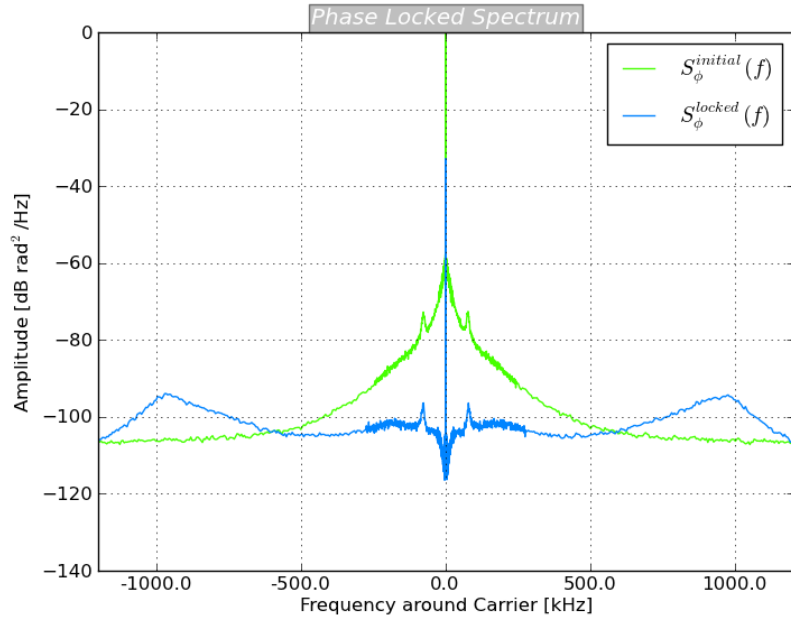
3 | Experimental Setup Part I: Orthogonality and Crosstalk

When the phase locked loop is not switched on the phase noise spectrum $S_{\phi}^{initial}$ shows a shape, which can be compared to the illustration in figure 1.11, consisting of a sharp carrier and modulation by the phase noise.

The phase locked loop is setup as shown in figure 2.7. When the phase lock is switched on (S_{ϕ}^{locked} in figure 3.1), the power is accumulated in the carrier and two servo bumps as in figure 2.6¹.

The functionality of the phase lock will be decreased by crosstalk between the polarizations.

Figure 3.1 When the phase locked loop is switched on the measured phase noise spectral density $S_{\phi}^{locked}(f)$ shows the expected shape of suppressed phase noise compared to the initial phase noise without stabilization $S_{\phi}^{initial}(f)$ close to the carrier and two servo bumps.



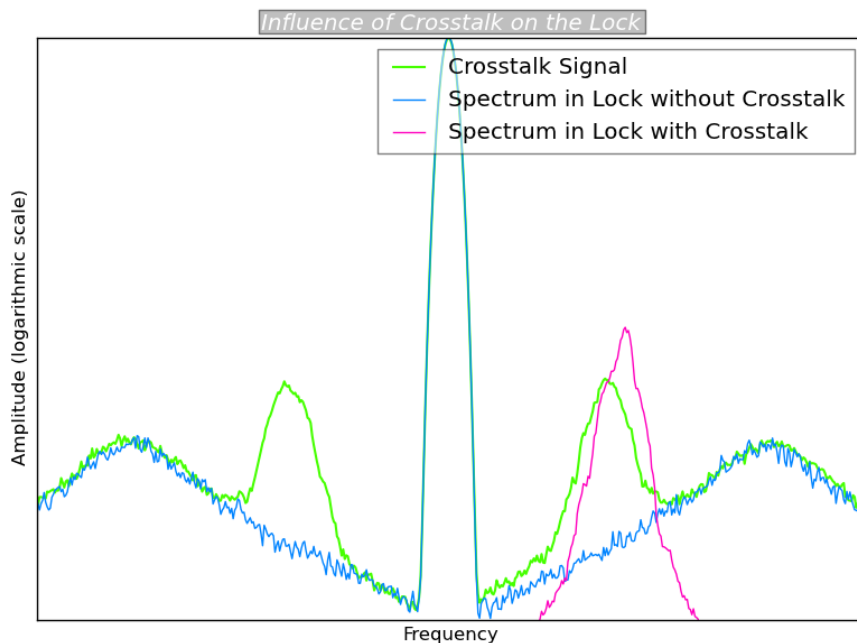
3.1 | Effect of Non-Orthogonality on the Phase Lock

To measure the influence of polarization crosstalk on the phase locked loop the phase locked signal is recorded with crosstalk and without crosstalk.

¹The measurement method and quantitative analysis of the signals is described in section 5.3.

Qualitatively, when the phase locked loop is aiming to reduce the error caused by a signal on which it cannot act, it will actually produce a "mirror"-noise peak on the opposite site of the carrier (see figure 3.2). Therefore crosstalk signals will always appear as actual phase noise.

Figure 3.2 Measurement of the influence of crosstalk on the phase noise spectrum in lock. Compared to a situation without crosstalk, a crosstalk signal from the other polarization leads to the creation of two peaks in the locked phase noise spectrum.



3.1.1 Needed Extinction Ratio for Beam Separation

The most difficult part in the creation of a crosstalk-free error signal is the final separation of the beams (see figure 2.7). To estimate the needed quality of the splitting element in figure 2.7, the beams are assumed to reach it in a perfectly orthogonal state and the crosstalk is only resulting from their separation with a limited extinction ratio.

The information, how well an element can separate orthogonal polarization states is expressed in the extinction ratio. It is the ratio of the wanted polarization intensity versus the unwanted polarization intensity in each output port of a polarizing element. Qualitatively, a splitting element with limited extinction ratio will cause a crosstalk signal as shown in figure 3.2.

Quantitatively, the power outside the carrier (P_{floor}) will be increased by the crosstalk with a certain amount compared to the situation without crosstalk. The resulting phase noise $\langle\phi^2\rangle$ can be calculated by the fraction of power contained in the carrier $P_{carrier}$ [31]

$$\eta = \frac{P_{carrier}}{P_{carrier} + P_{floor}} = e^{-\langle\Delta\phi^2\rangle}.$$

The signal P_{floor} can be rewritten as a fraction ϵ of the carrier signal $P_{floor} = \epsilon P_{carrier}$

$$\eta = \frac{1}{1 + \epsilon} \quad \text{and} \quad \langle\Delta\phi\rangle = \sqrt{-\ln\left(\frac{1}{1 + \epsilon}\right)}$$

The crosstalk signal will appear as an additional peak in the floor, which increases P_{floor} . The change of the rms phase noise $d\langle\Delta\phi\rangle$ with an infinitesimal change in the power

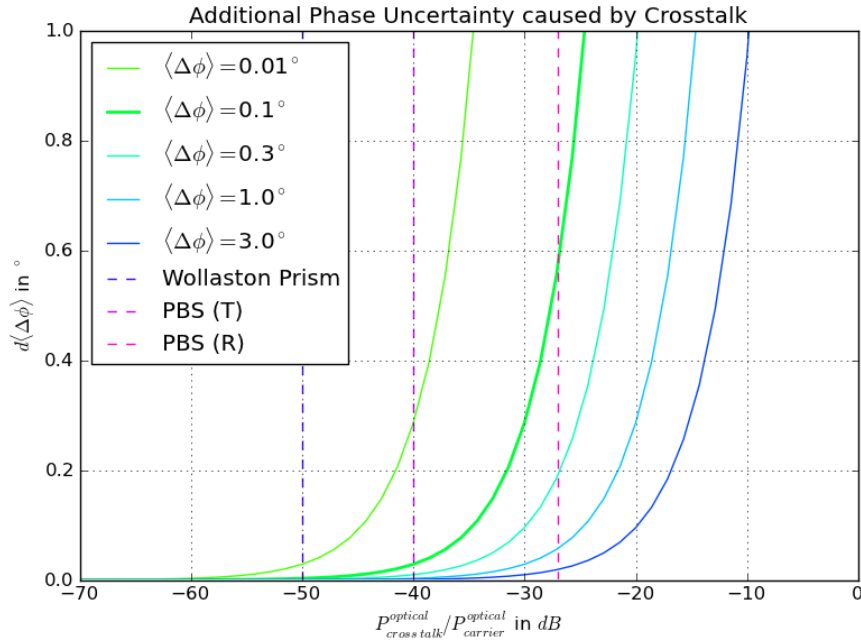
fraction in the carrier $d\epsilon$ is given by

$$d\langle\Delta\phi\rangle = \frac{1}{2(1+\epsilon)\sqrt{-\ln\left(\frac{1}{1+\epsilon}\right)}}d\epsilon = \frac{\eta}{2\langle\Delta\phi\rangle}d\epsilon. \quad (3.1)$$

Crosstalk will cause the power fraction in the carrier to change by $\Delta\epsilon = \frac{P_{\text{cross talk}}}{P_{\text{carrier}}}$. From equation 3.1 follows that the rise of the phase uncertainty depends on the initial phase stability $\langle\Delta\phi\rangle$ without crosstalk. For signals with very high phase stability the crosstalk will cause a larger effect.

A very good polarizing beam splitter cube relying on multiple dielectric coatings can reach an extinction ratio of 1/5000 in transmission and 1/500 in reflection. Calcite prisms as the Glan-Polarizer or the Wollaston prism reach extinction ratios of better than $> 1/100\,000$ for both beams.

Figure 3.3 A crosstalk signal as shown in figure 3.2 will increase the noise floor. The additional phase noise $d\langle\Delta\phi\rangle$ caused for a crosstalk at a suppression level $P_{\text{crosstalk}}/P_{\text{carrier}}$ is plotted for different initial phase fluctuations $\langle\Delta\phi\rangle$. Suppression ratios for typical extinction ratios of a calcite prism and polarizing beam splitters are inserted as dashed lines.

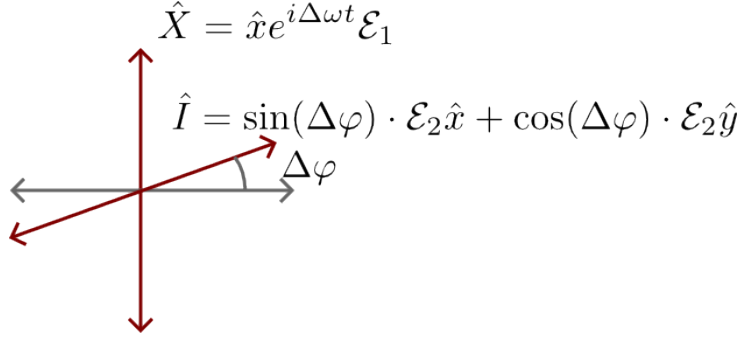


According to figure 3.3 a very good phase stability on the level of $\langle\Delta\phi\rangle \approx 0.1^\circ \dots 0.3^\circ$ can not be achieved with a coated polarizing beam splitter. Even very good polarizing beam splitter would lead to a large additional phase uncertainty of $0.2^\circ \dots 0.6^\circ$ in the reflected beam. A suppression of crosstalk to carrier of larger than -50 dB would be sufficient to reach a phase stability of $\langle\Delta\phi\rangle \approx 0.1^\circ \dots 0.3^\circ$ and can be provided by birefringent calcite prisms like the Wollaston prism.

3.1.2 Orthogonality after Combination

If the polarizations are not orthogonal after their combination, the angle $\Delta\varphi$ in figure 3.4 is unequal to zero, which means that the polarization \hat{I} has a component in \hat{X} direction.

Figure 3.4 After perfect recombination of the beams, the resulting beam contains the two polarizations with $\Delta\varphi = 0$.



The limit set by the acceptable crosstalk level for a phase stability of about 0.1° can be obtained from the estimation in figure 3.3. A crosstalk signal of -40 dB height below the carrier would add acceptable phase noise in the order of 0.03° . According to this the orthogonality has to be better than

$$-40dB \geq 10 \cdot \log \left(\frac{|\sin(\Delta\varphi)\mathcal{E}_2|^2}{|\mathcal{E}_1|^2} \right) \Rightarrow \Delta\varphi \leq 0.57^\circ. \quad (3.2)$$

Measurement of $\Delta\varphi$ with the Residual Beat Signal

The idea is to make use of the fact that signals with a frequency difference and polarization components along a common axis will show a beat signal. This residual beat signal can be used to extract the degree of orthogonality.

$$\hat{X} = \hat{x}e^{i\Delta\omega t}\mathcal{E}_1 \quad I = \sin(\Delta\varphi) \cdot \mathcal{E}_2\hat{x} + \cos(\Delta\varphi) \cdot \mathcal{E}_2\hat{y}$$

For a projection on the \hat{x} -axis (μ is taking the finite spatial overlap into account)

$$P_{AC,res} = |\mathcal{E}_1 \cdot e^{i\Delta\omega t} + \mathcal{E}_2 \cdot \sin \Delta\varphi|_{AC}^2 = 2\mathcal{E}_1\mathcal{E}_2 \cdot \sin(\Delta\varphi) \cos(\Delta\omega t)\mu.$$

The height of the residual beat signal depends strongly on the spatial overlap of the beams. Therefore the information obtained only from the residual beat signal is not sufficient to estimate the orthogonality, but needs to be compared to the maximum beat signal, which is obtained when a polarizer at 45° is inserted. The maximum beat signal is given by

$$P_{AC,45^\circ} = |\mathcal{E}_1 \cdot e^{i\Delta\omega t} + \mathcal{E}_2|_{AC}^2 = \mathcal{E}_1\mathcal{E}_2 \cdot \cos(\Delta\omega t)\mu.$$

Then

$$\sin \Delta\varphi = \frac{P_{AC,res}}{2 \cdot P_{AC,45^\circ}} \pm \sqrt{\left(\frac{\Delta P_{AC,res}}{2 \cdot P_{AC,45^\circ}} \right)^2 + \left(\frac{P_{AC,res} \cdot \Delta P_{AC,45^\circ}}{2 \cdot (P_{AC,45^\circ})^2} \right)^2}$$

On the spectrum analyzer one can directly observe the difference of the peak power Δ_{dB} of the residual beat signal to the one with polarizer in dB^2 . Using the relation above the signal is related to the non-orthogonality by

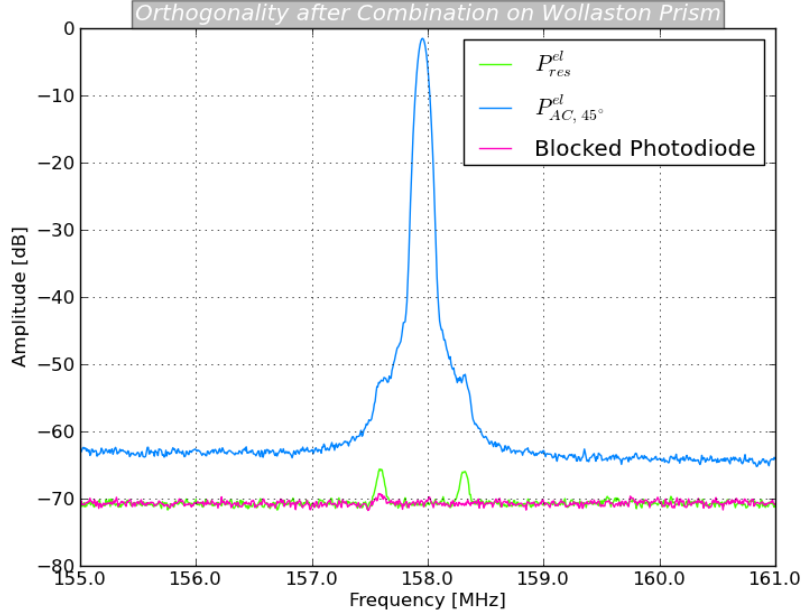
$$\sin(\Delta\varphi) = \arcsin \left(10^{\frac{1}{2}\Delta_{dB}/20} \right).$$

The residual beat signal method is used to measure the resulting orthogonality for combination on the Wollaston prism and the result is shown in figure 3.5.

²Displayed on the spectrum analyzer is the ratio of the electronic powers P_{el} . Optical power $P_{optical}$ and electronic power are related by $P_{el} \propto P_{optical}^2$.

The residual beat signal method is used to measure the resulting orthogonality of the beams and the result is shown in figure 3.5.

Figure 3.5 After combination on the Wollaston prism the orthogonality of the polarizations is measured by comparing the beat signal with ($P_{AC, 45^\circ}^{el}$) and without polarizer (P_{res}^{el}). The underground is recorded by blocking the photodiode.



The residual signal is below the noise floor at -70 dBm. With inserted polarizer the maximum of the beat signal has a power of -2 dBm. This gives a relative suppression of better than $\Delta_{dB} = -68$ dB, and therefore an orthogonality of

$$\Delta\varphi < 0.01^\circ.$$

3.1.3 Distortion of Orthogonality

Once the beams are combined and their orthogonality is measured, this value can be used to identify elements which distort orthogonality of polarization. Distortion of orthogonality means, that the polarization of one beam is changed, so that it obtains a polarization component in the orthogonal direction. The extreme case of such an element is a coated polarizing beam splitter PBS which projects onto a common axis.

In the Jones formalism a rotated coated PBS can be written as

$$R(-\theta) \cdot \begin{pmatrix} 0 & 0 \\ 0 & 1 \end{pmatrix} \cdot R(\theta) \quad R(\theta) = \begin{pmatrix} \cos(\theta) & \sin(\theta) \\ -\sin(\theta) & \cos(\theta) \end{pmatrix},$$

where $R(\theta)$ is the rotation matrix and the PBS has its transmission axis along the y -polarization. A polarizing beam-splitter reflects one polarization $t_x = 0$ and transmits the other $t_y = 1$ completely.

An ideal non-polarizing beam-splitter treats both polarizations completely equal $t_x = t_y$. A general beam splitting element can be written as

$$\begin{pmatrix} t_x & 0 \\ 0 & t_y \end{pmatrix},$$

which describes the polarizing beam splitter in one extreme case and the non polarizing beam splitter in the other. A perfect ($t_x = t_y$), rotated non-polarizing beam splitter is described by

$$\begin{pmatrix} t_x \sin^2(\theta) + t_x \cos^2(\theta) & 0 \\ 0 & t_x \sin^2(\theta) + t_x \cos^2(\theta) \end{pmatrix}.$$

It has no diagonal elements and therefore it wont distort the orthogonality of the polarizations that enter it.

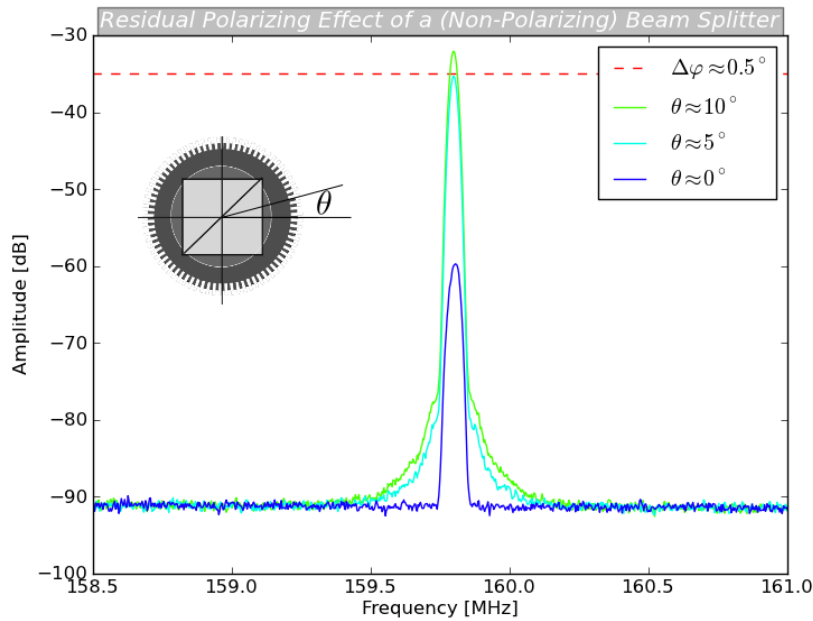
A real beam splitter only achieves equal transmission coefficients for orthogonal polarizations up to 10% (e.g. Thorlabs BS010 beamsplitter), so that $t_x = t_y + \epsilon$ and the rotated beam splitter can be written as

$$\begin{pmatrix} t_y \sin^2(\theta) + (\epsilon + t_y) \cos^2(\theta) & -t_y \sin(\theta) \cos(\theta) + (\epsilon + t_y) \sin(\theta) \cos(\theta) \\ -t_y \sin(\theta) \cos(\theta) + (\epsilon + t_y) \sin(\theta) \cos(\theta) & t_y \cos^2(\theta) + (\epsilon + t_y) \sin^2(\theta) \end{pmatrix}$$

Therefore a beam splitting element with small differences in the transmission of x - and y -polarization needs perfect alignment to a rotation angle of multiples of $\theta = \pi/2$ and it will show residual polarizing properties for every other angle.

Alignment of optical elements can be achieved by using the residual beat signal, which rises for imperfect orientation. In figure 3.6 the signal observed on the spectrum analyzer is shown for different orientations of a non-polarizing beam splitter in a rotary mount. Reference for alignment is the suppression ratio of residual signal without polarizer to the maximum beat signal in decibel. When the beam splitter is well aligned the suppression ratio is equal to the one without beam splitter. For small rotations out of this direction the beat signal rises.

Figure 3.6 Residual polarizing effects of elements like non-polarizing beam splitters, glass plates and substrates can be detected with the measurement method for orthogonality. For slightly misaligned components the beat signal rises rapidly. The residual polarizing effect of the non-polarizing beam splitter cube measured here, can cause non-orthogonality larger than 0.57° .



Other elements like glass plates and substrates have been tested. They all show visible effects on the orthogonality of the polarizations depending on their alignment.

3.2 | Estimation of the Effect of Crosstalk on the Optical Lattice

The linear polarizations are converted to orthogonal circular polarizations by a $\lambda/4$ -plate. As the Jones matrix of any retarding element is unitary it will not distort orthogonality. Nevertheless, it won't create perfectly circular polarization, but polarization with residual ellipticity due to the quarterwave-plate retardance error.

3.2.1 Measurement of Quarterwave-Plate Retardance

When a wave propagates through a birefringent material its polarizations along and perpendicular to the optical axis experience a different phase shift. The difference of these phase shifts is known as retardation Γ :

$$\frac{\Gamma}{2\pi} = \frac{\Delta x}{\lambda} \quad \Delta x = (n_{slow} - n_{fast}) \cdot L.$$

In the Jones formalism a waveplate $\Lambda(\Gamma)$ with its optical axis rotated by θ can be written as

$$R(-\theta)\Lambda(\Gamma)R(\theta) \text{ with } \Lambda(\Gamma) = \begin{pmatrix} 1 & 0 \\ 0 & e^{-i\Gamma} \end{pmatrix}.$$

For $\Gamma = \pi/2$ and a rotation angle of 45° one obtains the Jones matrix of a quarterwave plate, which produces circular polarization from incident linear polarization along the \hat{x} - or \hat{y} -axis.

Now an erroneous quarterwave plate should be considered. Its retardance can be written as the retardance of a quarterwave plate with an additional error ϵ

$$\Gamma = \frac{2\pi}{\lambda} \Delta x = \frac{2\pi}{\lambda} \left(\frac{\lambda}{4} + \epsilon \right),$$

such that the out coming polarization won't be any longer purely circular. Nevertheless, the Jones matrix of any retardance element and therefore any rotated wave plate with arbitrary error is unitary. Since unitary operations preserve the inner product, orthogonality of the polarizations will be preserved as well. This means, that the incoming basis set of linear polarizations will be transformed into a new basis set that can be expressed as a rotation/ linear combination of the purely circular basis:

$$|l_1\rangle = \cos(\alpha)|\sigma^+\rangle - \sin(\alpha)|\sigma^-\rangle \quad |l_2\rangle = \sin(\alpha)|\sigma^+\rangle + \cos(\alpha)|\sigma^-\rangle. \quad (3.3)$$

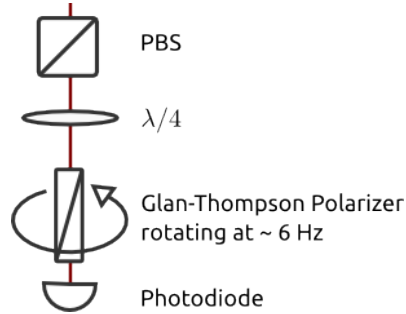
The retardance error of the quarterwave plate and the resulting purity of circular polarization can be measured with a rotating polarizer (figure 3.7).

The measurement results are shown in figure 3.8.

Expectation

When the incoming polarization is linear a rotation of the Glan-Polarizer would lead to periodic minima and maxima of the intensity on the photodiode. Insertion of a perfect quarterwave plate leads to creation of circular polarized light which is composed of equal parts of \hat{x} and \hat{y} linear polarization. The intensity stays at half of the maximum value for any rotation angle. A quarterwave plate with large error is obtained by setting $\Gamma = \frac{2\pi}{\lambda} \left(\frac{\lambda}{4} + \frac{\lambda}{40} \right)$. The calculated produced polarization is elliptical and shows a large residual wiggling.

Figure 3.7 Setup for the measurement of the quarterwave plate retardance error: A first polarizer defines the linear polarization axis. A second polarizer acts as an analyzer after which the intensity is recorded on a photodetector. By rotation of the second polarizer with and without quarterwave plate the retardance error of the quarterwave plate can be determined.



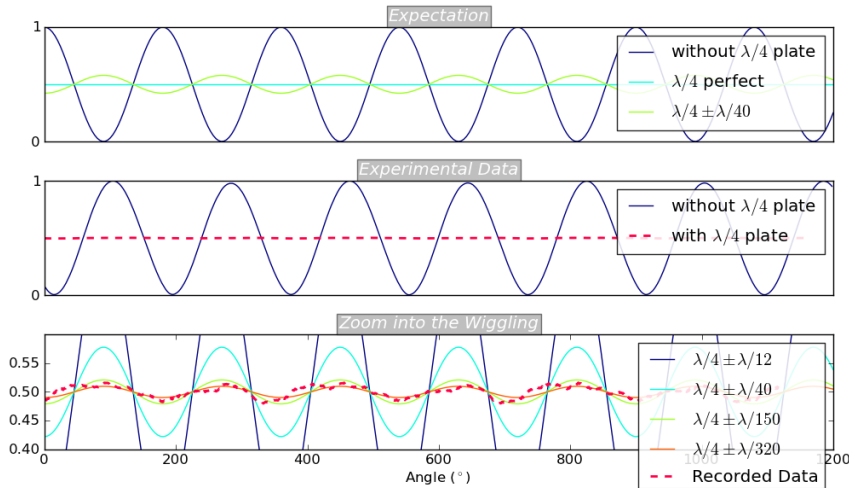
Experimental Data

First the blue trace is recorded without the inserted quarterwave plate. For rotation of the Glan-polarizer a motor with a frequency of 6 Hz is used. Then the quarterwave plate is inserted and the residual wiggling recorded. In this case a zero-order plate has been used and the residual wiggling is on this scale not visible.

Zoom into the Wiggling

To obtain the error of the used quarterwaveplate, the peak to peak amplitude of the residual wiggling is compared to the expectation for different quarterwaveplate errors.

Figure 3.8 Measurement of the quarterwave plate retardance error.



Comparison between the experimental data and the expectation yields a retardance-error of

$$\epsilon \approx \frac{\lambda}{200}.$$

This can be connected to the angle α in equation by projection of the resulting polarization after the erroneous quarterwave plate on the circular basis states. The resulting rotation angle is $\alpha \approx 0.8^\circ$, i.e.

$$\cos^2(\alpha) = 99.98\%,$$

is in the desired circular polarization state for this quarterwave plate.

3.2.2 Estimation of the Influence of Crosstalk and Retardance Error on the Optical Lattice

Non-orthogonality in the linear polarizations before the quarterwave plate and the retardance error of the quarterwave plate will lead to a crosstalk between the circular polarizations, such that a phase shift that should only influence, say the σ^+ lattice will cause a part of the σ^- lattice to shift as well.

The resulting lattice $|l_{ges}\rangle$ is the sum of the single lattices $|l_1\rangle$, $|l_2\rangle$, each of which is controlled by an individual phase locked loop. First, the case without error is considered, i.e. where $|l_1\rangle$ and $|l_2\rangle$ don't show a polarization crosstalk and a beam with twice the intensity propagates in the opposite direction to create a standing wave:

$$|l_1\rangle = e^{ikx}|\sigma^+\rangle \quad |l_2\rangle = e^{ikx}|\sigma^-\rangle \quad |l_{back}\rangle = e^{-ikx}(|\sigma^+\rangle + |\sigma^-\rangle) \quad k = \frac{2\pi}{\lambda}, \quad x : \text{position}.$$

Relative phase changes θ between $|l_1\rangle$ and $|l_2\rangle$ can be considered in the superposition by

$$|l_{ges}\rangle = e^{-i\theta}|l_1\rangle + e^{i\theta}|l_2\rangle + |l_{back}\rangle.$$

Variation of the Trapping Frequency during a Transport Sequence

The different coupling of the states to the σ^+ and σ^- polarization can be taken into account by defining

$$\hat{s}_0 = 0 \cdot |\sigma^+\rangle\langle\sigma^+| + 1 \cdot |\sigma^-\rangle\langle\sigma^-| \quad \hat{s}_1 = \sqrt{\frac{7}{8}} \cdot |\sigma^+\rangle\langle\sigma^+| + \sqrt{\frac{1}{8}} \cdot |\sigma^-\rangle\langle\sigma^-|.$$

The resulting attractive potential seen by an atom in state $|0\rangle$ or state $|1\rangle$ is given by

$$U_{|0\rangle} = \langle l_{ges} | \hat{s}_0^2 | l_{ges} \rangle \quad U_{|1\rangle} = \langle l_{ges} | \hat{s}_1^2 | l_{ges} \rangle. \quad (3.4)$$

Figure 3.9 shows how the potential depth for state $|1\rangle$ varies even without polarization crosstalk due to the sensitivity of the state $|1\rangle$ to both circular polarizations.

During the transport the phase between the two lattices changes, so that minima and maxima no longer overlap. At the point where the phase difference of σ^+ and σ^- potential is 90° the minimum of the σ^- potential coincides with the maximum of the σ^+ potential.

In this configuration the minimum of the state $|1\rangle$ -potential is no longer at zero. The sensitivity of state $|1\rangle$ to the σ^- polarization lifts the minimum to $1/8 = 0.125$. Equivalently, the maximum is decreased to $1 - 1/8$ of the maximum potential value for $\theta = 0^\circ$. Therefore, the effective potential depth is decreases by $2/8$ for $\theta = 90^\circ$.

Since the potential follows the intensity distribution of a standing wave, its periodicity is described by a $\cos^2(kx)$ -function and its amplitude by $U_0(\theta)$ is dependent on the phase θ . In vicinity of the potential minima it can be approximated by a harmonic oscillator

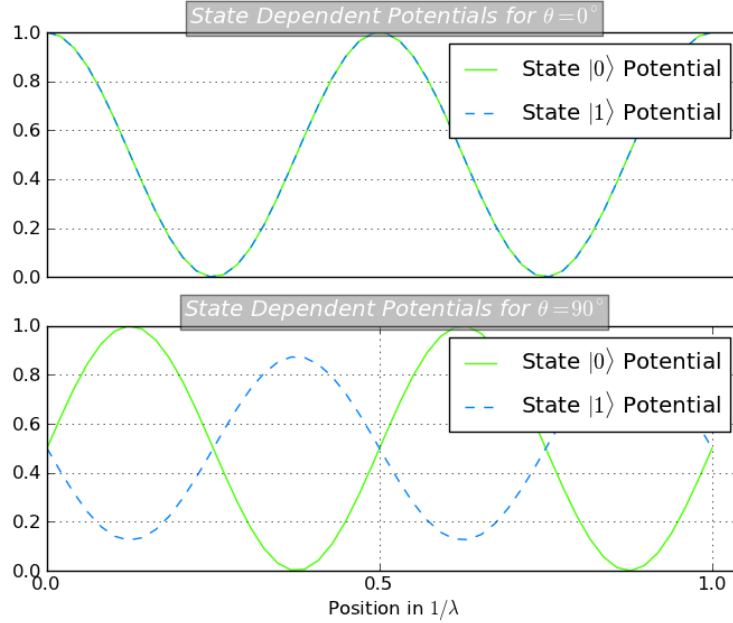
$$U_{Potential}(x) = U_0 \cos^2(kx) \stackrel{\text{minimum}}{\approx} U_0(\theta) k^2 x^2 \quad U_{harmonic}(x) = \frac{1}{2} m_{Cs} \omega_{trap}^2 x^2,$$

with a trapping frequency of

$$\omega_{trap} = 2\pi \sqrt{\frac{2U_0(\theta)k^2}{m_{Cs}}}.$$

ω_{trap} varies with the square root of the effective potential depth during the transport as shown in figure 3.10. For a phase of $\theta = 90^\circ$ state $|1\rangle$ will experience a trapping frequency which is decreased by a factor of $\sqrt{\frac{2}{8}}$ compared to the one for state $|0\rangle$.

Figure 3.9 Shown is the potential for state $|0\rangle$ and state $|1\rangle$ at different positions along the one dimensional lattice created by σ^+ and σ^- polarization with a relative phase shift θ .



Variation of the Trapping Frequency during a Transport Sequency with Quarterwave Plate Errors and Non-Orthogonality

In the scheme based on direct synthesis of light polarization, the trapping frequency dynamic during transport will change due to polarization crosstalk between the two phase locks. Therefore, the $|l_1\rangle$ potential will not be a perfect $|\sigma^+\rangle$ lattice any more, but will contain a $|\sigma^-\rangle$ part, the same holds for the $|l_2\rangle$ potential.

For a lattice crosstalk occurring due to non-orthogonality the resulting states can be rewritten as

$$|l_1\rangle = |\sigma^+\rangle e^{ikx} \quad |l_2\rangle = (\sin \phi |\sigma^+\rangle + \cos \phi |\sigma^-\rangle) e^{ikx}, \quad (3.5)$$

while the quarterwave plate error leads to

$$|l_1\rangle = (\cos \epsilon |\sigma^+\rangle - \sin \epsilon |\sigma^-\rangle) e^{ikx} \quad |l_2\rangle = (\sin \epsilon |\sigma^+\rangle + \cos \epsilon |\sigma^-\rangle) e^{ikx}. \quad (3.6)$$

To stay within a region of 0.5 % of the case without error as shown in figure 3.11 the parameters ϵ and ϕ need to take the following values

$$\epsilon = 0.4^\circ \text{ and } \phi = 0.5^\circ.$$

The required value for orthogonality is very close to the value needed for the phase stability of the lock in equation ($\phi \leq 0.57^\circ$) and was measured to be better than 0.01° (page 27) and with careful alignment of the following glass plates and substrates it can be kept in the same order of magnitude.

The required value for the error of the quarterwave plate of $\epsilon = 0.4^\circ$ corresponds to a percentage of

$$\cos^2(\epsilon) = 99.995^\circ$$

in the right polarization component. To fulfil this requirement, the retardance error of the quarterwave plate has to be smaller than

$$\frac{\lambda}{450}.$$

Figure 3.10 Variation of the trapping frequency for state $|0\rangle$ and state $|1\rangle$ during a transport sequence, i.e. during a variation of the relative phase between the circular polarizations.

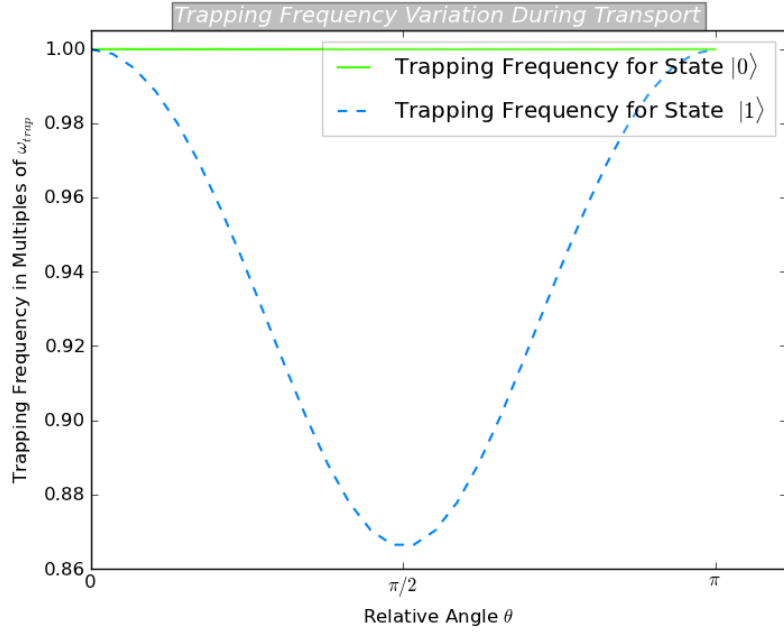
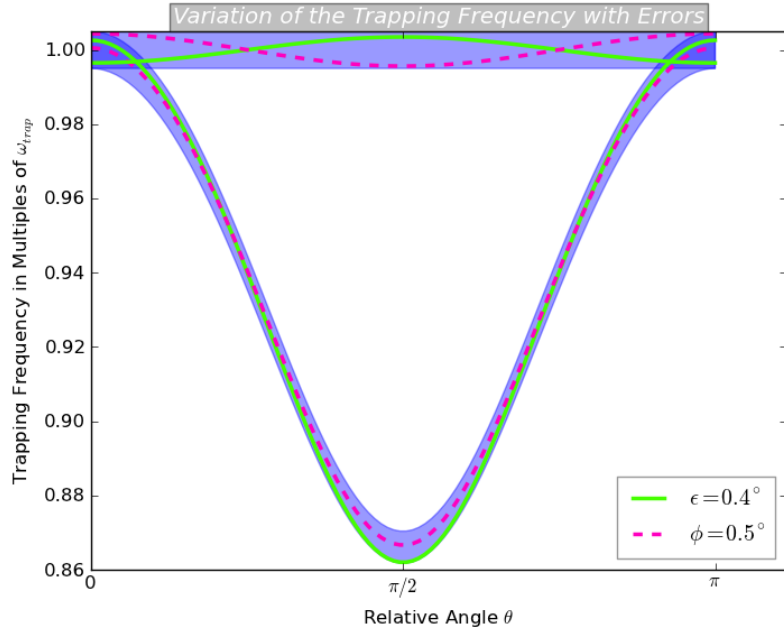


Figure 3.11 The 0.5 % region around the trapping frequency variation without additional errors caused by non-orthogonality and quarterwave plate error is indicated by the blue, filled region. The trapping frequency variation with errors is obtained by inserting equation 3.5 and 3.6 into the expression for the resulting lattice.



This is larger than the error measured for the quarterwave plate (page 30), but quarter-wave plates with a retardance precision of up to $\lambda/1000$ can be achieved [42].

4 | Experimental Setup Part II: Elements in the Phase Locked Loop

4.1 | Reference: Direct Digital Synthesizer

The electronic reference signals for each phase locked loop channel have to be phase stable relative to each other. Each reference should have a output frequency of 80 MHz determined by the resonance frequency of the AOM.

The used model AD9954 [8] generates two sinus-output waves of up to 160 MHz, each with a phase resolution of 0.022° . The sequences for state-dependent transport are controlled by the two reference signals. For the AD9954 phase and frequency of each output can be controlled rapidly –up to 10 million changes per second of frequency and phase– while it offers fine tunability – 0.09 Hz in frequency and 0.022° in phase.

Working Principle and Resolution

A Direct Digital Synthesizer (DDS) provides an output, which is synthesized with help of a phase accumulator. Its way of functioning can be depicted as in figure 4.1. An analogue sine wave is represented as an arrow rotating over the outer circle. The speed with which the arrow rotates gives the frequency and the angle the instantaneous phase.

A digitalized wave is depicted by dividing the continuous outer circle into discrete sections. The number of these sections determines the resolution of the device.

Two values provided by the user of the DDS determine the frequency output value: The system clock f_{sys} (maximally 400 MHz) and the frequency tuning word FTWO.

After each cycle of the system clock the phase accumulator jumps to the next value, which is determined by the FTWO.

When one full cycle is completed the phase accumulator overflows and a new cycle of the sine-wave begins. Two phase accumulators driven with the same reference clock will show a high phase stability to each other.

The generation of the output wave is shown in figure 4.1.

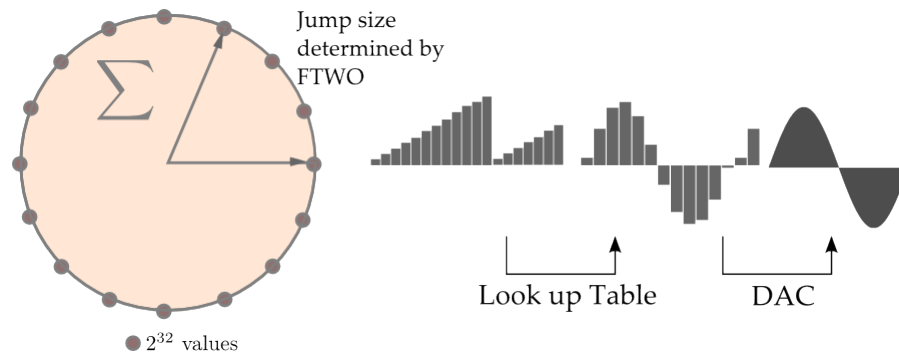
The AD 9954 has a frequency tuning word of 4 byte, i.e. 32 bit length. Therefore the outer circle is divided into 2^{32} values and maximally 2^{32} cycles of the system clock will lead to an overflow. The length of the phase accumulator also determines the frequency resolution to

$$\Delta f = \frac{f_{sys}}{2^{32}} = \frac{400 \text{ MHz}}{2^{32}} = 0.09 \text{ Hz.}$$

Additional to the control of the output frequency via the frequency tuning word FTWO the user has also control over the output phase via the phase word POW.

The phase word has 14 bit length, therefore the output wave can be phase shifted with a

Figure 4.1 At each rising edge of the reference clock the phase accumulator jumps to the next instantaneous phase value. From a look-up table the amplitude belonging to the respective instantaneous phase is pulled and the wave is synthesized with the resolution of the look-up table in the digital domain. A digital to analogue converter creates the output signal.



resolution of

$$\Delta\phi = \frac{360^\circ}{2^{14}} = 0.022^\circ.$$

$$f_{out} = \frac{FTWO \times f_{sys}}{2^{32}} \quad \Phi = \left(\frac{POW}{2^{14}} \right) \times 360^\circ$$

The AD9954 has an on-board RAM memory in which tuning patterns of 1000 steps for frequency and phase tuning words versus time can be written.

4.2 | Photodetector

In a LED the recombination of electrons and holes in a semiconductor pn-junction leads to light emission. Similarly, a photocurrent can be created in the reversed process: by photons, which are absorbed in the depletion region. The efficiency of electron creation per photon is given by the quantum efficiency η . Related to η and commonly found in the data sheet is the ratio of incident light power P_{opt} to created photocurrent I_{PD} as responsivity

$$\mathcal{R}(f) = \frac{I_{PD}}{P_{opt}} \quad \eta = \frac{I_{PD}/e}{P_{opt}/(hf)}, \quad (4.1)$$

where f is the frequency of the light.

Thermal processes in the pn-junction will lead to a dark current I_{Dark} in a direction determined by the bias voltage over the photodiode.

Another important characteristic of the photodetector is its bandwidth $\Delta\nu$. Only alternating optical signals which oscillate slower than the bandwidth can be detected. The reason for limited bandwidth is that the charge distribution in the semiconductor results in a capacitance which will form a low pass filter together with load resistances.

The three main noise contributions in the photodetector are given by (e.g. [2])

$$\sigma_{I_{PD}, shot}^2 = 2e\bar{I}_{PD}\Delta\nu \quad \sigma_{I_{Dark}, shot}^2 = 2e\bar{I}_{Dark}\Delta\nu \quad \sigma_{I_{Thermal}}^2 = \frac{4k_B T}{R}\Delta\nu, \quad (4.2)$$

where \bar{I}_{PD} denotes the average of the photocurrent.

The flow of current is not continuous, but created by single electrons. The statistical description of their motion leads to a Poisson distribution of the current around its mean value, which is known as electronic shot noise $\sigma_{I_{PD}, shot}^2$. The dark current I_{Dark} will lead to shot noise $\sigma_{I_{Dark}, shot}^2$. Thermal noise $\sigma_{I_{Thermal}}^2$ is present in the resistance R of the photodetector.

The noise contributions of thermal and dark current stay constant, while the shot noise associated with the detection process rises with the incident light power. It is assumed, that the incident power will be so large, that the noise contributions of thermal and shot noise can be neglected¹

The beat signal power which is not in the carrier contains the information about the noise. At the point where the signal power outside the carrier drops below the photodiode noise the signal doesn't contain useful error signal information any more.

Quantitative description of the phase noise $\langle\phi^2\rangle$ can be given by the fraction of power in the carrier $P_{carrier}$ compared to the overall signal $P_{carrier} + P_{floor}$ [31]

$$\eta = e^{-\langle\phi^2\rangle} = \frac{P_{carrier}}{P_{carrier} + P_{floor}}. \quad (4.3)$$

From equation 4.3 follows for a phase uncertainty of $\langle\Delta\phi\rangle = 0.1^\circ$ that 99.9996 % of the power are accumulated in the carrier, therefore the noise information is contained in the floor with

$$P_{floor} \approx (1 - 0.999996)P_{carrier}.$$

The carrier signal is created by the beating of the two signals on the photodiode: For two electrical fields E_1 , E_2 with identical polarizations the resulting time dependent optical power $P_{opt}(t)$ on a photodiode with active surface A can be written as

¹This can be justified by comparing the optical power in the calculation with the noise equivalent power of $3.5 \cdot 10^{-11} \text{ W}/\sqrt{\text{Hz}}$ from the photodiode datasheet [35].

$$P_{opt}(t) = I(t) \cdot A = \frac{1}{2} A \epsilon_0 c |E_1(t) + E_2(t)|^2 = \underbrace{P_1 + P_2}_{DC} + \underbrace{2\sqrt{P_1 P_2} \mu \cos(\Delta\omega t + \Delta\varphi(t))}_{AC},$$

where P_i is the optical power of the single fields E_i , $\Delta\omega$, $\Delta\varphi$ denote relative frequency and phase differences between the electrical fields and μ takes their finite spatial overlap into account.

The detected optical signal consists of a DC part which is constant in time and an AC part that oscillates at the difference frequency Δf and contains the relative phase information $\Delta\varphi$.

For the shot noise resulting from this optical power only the average of the resulting photo current is important. Using equations 4.1 and 4.2 this gives

$$\bar{I}_{DC} = (P_1 + P_2)\mathcal{R} \quad \bar{I}_{AC} = 0.$$

Thus, only the DC part contributes to the shot noise, since the oscillating AC signal averages out over time. For the main square fluctuations this gives

$$\sigma_{I_{PD, shot}}^2 = 2e\mathcal{R}(P_1 + P_2)\Delta\nu.$$

The signal is contained in the AC (beating) part and its mean squared current is

$$\langle I_{beat}^2 \rangle = (2\mathcal{R}\sqrt{P_1 P_2} \mu)^2 \langle \cos^2(\Delta\omega t + \Delta\varphi) \rangle = 2\mathcal{R}^2 \mu^2 P_1 P_2.$$

This results in a signal to noise ratio of

$$SNR = \frac{\langle I_{beat}^2 \rangle}{\sigma_{I_{PD, shot}}^2} = \frac{\mathcal{R} \mu^2}{2e\Delta\nu} \frac{P_1 P_2}{P_1 + P_2}.$$

Assuming equal optical powers in the beams ($P_1 = P_2 = P$) and perfect overlap ($\mu = 1$) a $SNR = 1$ for the noise floor power is reached at²

$$P = \frac{SNR = 1}{1 - 0.999996} \frac{4e\Delta\nu}{\mathcal{R}} \approx 53 \mu W.$$

²From the datasheet [35] of the photodiode $\Delta\nu = 150$ MHz, responsivity $\mathcal{R} = 0.45$ A/W.

4.3 | Controlled Oscillators: VCO and AOM

To change phase and frequency of the lattice beams Acousto-Optic Modulators (AOMs) are used, as indicated in figure 2.7 (page 22). A voltage controlled oscillator (VCO) is used to drive the AOM, such that the combination of VCO and AOM becomes the controlled oscillator in the PLL.

The controlled oscillator should show a linear response to the filter voltage, which is verified in section 4.3.2. Phase noise suppression is based on modulation of the frequency of the controlled oscillator, which is characterized by the modulation bandwidth, see 4.3.4. It becomes evident that the main effect of the AOM on the behavior of the PLL consists of the signal delay time (dead time) caused by the traveling time of the sound wave through the AOM crystal to the beam 4.3.5.

4.3.1 Working Principle of the AOM

The working principle of an Acousto-optic modulator is described in detail for instance in [30].

It is illustrated in figure 4.3.1. When an RF-signal is applied to a piezo-electric material it will contract and expand with the frequency of the RF-signal. In the used AOM the transducer is connected to a Tellurium Dioxide crystal [7], in which it will create an acoustic wave. The acoustic wave travels inside the crystal as a modulation of the index of refraction, which results in a moving grating structure. Light propagating through the crystal can be diffracted on this grating into different orders. The used material and the RF center frequency and power depend on the used AOM model. Operated in the Bragg regime the angle of incidence is given by Bragg's law for a diffraction grating, where the spacing between the diffraction planes is the acoustic wavelength. Only one diffraction order is produced in this case.

For the first order diffracted beam follows from momentum conservation for the wave vectors

$$\vec{k}_1 = \vec{k}_0 + \vec{k}_{acoustic} \quad |\vec{k}| = \frac{2\pi f}{v},$$

where f is the frequency of the respective beam and v its velocity.

From energy conservation follows the shift of frequency in the first diffraction order with respect to the incident beam by the RF-frequency

$$f_1 = f + f_{RF}.$$

The incident light has a wavelength of 865.9 nm. The shift of 80 MHz in frequency is equivalent to a change of ≈ 0.2 pm in wavelength.

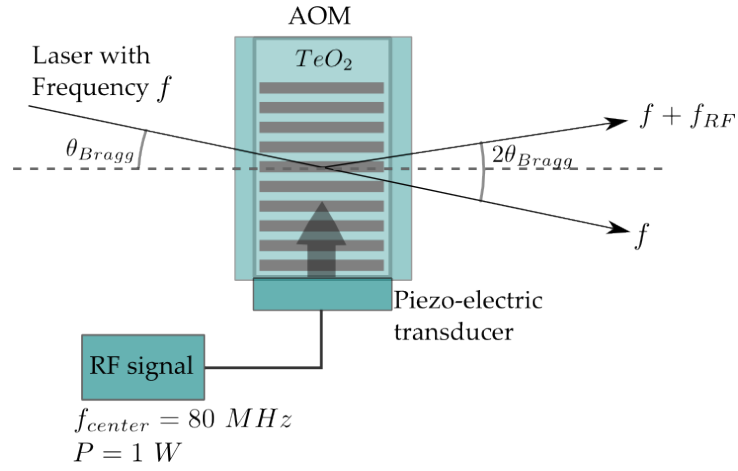
4.3.2 Sensitivity Constant of the VCO

The RF signal applied to the AOM is the amplified output of a VCO. Consequently the frequency in the first diffraction order of the AOM can be varied around the center frequency of 80 MHz by changing the voltage applied to the VCO.

The VCO should be linear in its response to the control voltage: The sensitivity constant K_{VCO} of the VCO relates the frequency change at the output Δf to voltage changes ΔV at the input [41].

For a non-linear controlled oscillator compensation of frequency or phase changes are difficult to achieve in the phase locked loop, since the filter voltage will only depend on the measured error. If the needed voltage to compensate for the error varies, the loop

Figure 4.2 The used AOM contains a Tellurium Dioxide crystal in which a Bragg grating is created by contraction and expansion of a transducer with the frequency of the driving RF-signal. For operation in the Bragg regime one frequency shifted diffraction order will be created.

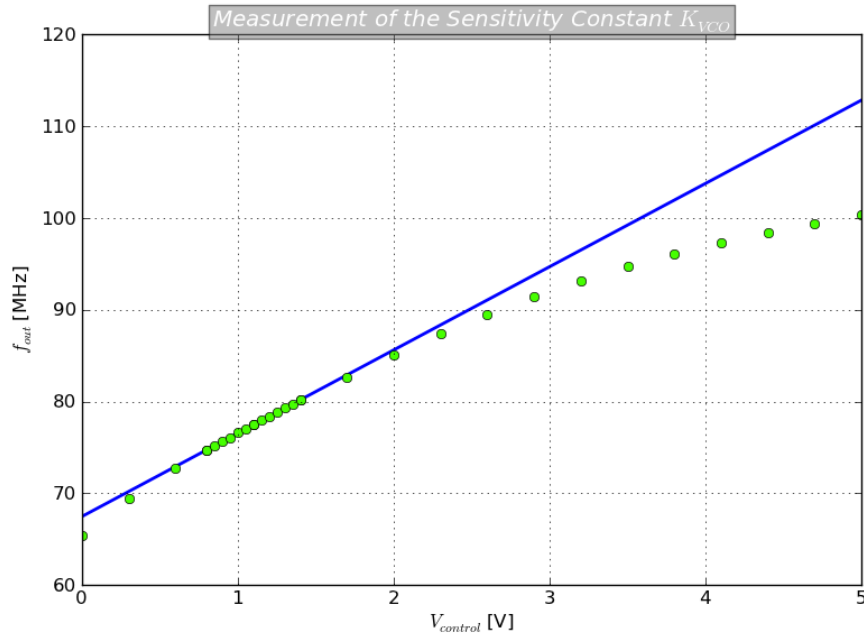


will need a longer time to compensate the error.

For a linear dependence $\Delta f \propto K_{VCO} \Delta V_{control}$, such that a certain change in the VCO's output frequency is always accomplished by the same change in the filter voltage.

The measurement of the VCO's sensitivity constant is shown in figure 4.3.

Figure 4.3 Measurement of the VCO sensitivity constant K_{VCO} . The control voltage of the VCO is varied. The output frequency can be observed as a peak on a spectrum analyzer.



In the region of $V_{control} = 0.75 \dots 2.2V$ ($f \approx 72 \text{ MHz} \dots 85 \text{ MHz}$) the dependence of the VCO output frequency on the control voltage is found to be linear with a sensitivity constant of

$$K_{VCO} = \frac{\Delta f}{2\pi \Delta V_{control}} = \frac{1}{2\pi} (9.07 \pm 0.05) \frac{\text{MHz}}{\text{V}}.$$

Thus the output voltage of the VCO can be written as

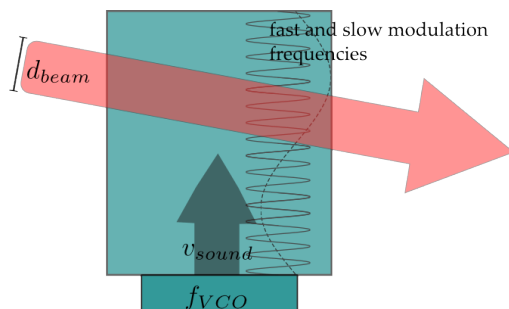
$$f_{out} = K_{VCO} \cdot V_{control}.$$

4.3.3 Modulation Bandwidth of the Oscillators

To obtain a phase locked signal, the phase of the oscillator has to be modulated to compensate for measured deviations from the reference. Each device that can be modulated in its output frequency has a characteristic modulation bandwidth in which this can be done.

The origin of the AOMs modulation bandwidth can be explained as indicated in figure 4.4. For large modulation frequencies, the effect averages out over the beam diameter.

Figure 4.4 An optical beam of diameter d_{beam} transverses the diffraction grating created in an AOM-crystal for a driving voltage modulated around the carrier frequency. The carrier frequency transverses the beam with the acoustic sound velocity v_{sound} .



From the time t_{cross} with which the acoustic wave transverses the beam, the bandwidth frequency BW_{AOM} (with period time T_{BW}) is antiproportional to the beam size [4]

$$t_{cross} \approx \frac{d_{beam}}{v_{sound}} \quad \frac{1}{2}T_{BW} > t_{cross} \quad \Rightarrow \quad \frac{v_{sound}}{2d_{beam}} \approx BW_{AOM}.$$

For the modulation to be transferred to the beam efficiently, the beam diameter d_{beam} inside the AOM has to be chosen as small as possible. As the diffraction of the beam on the refractive index grating is a Bragg scattering process, it is based on constructive interference, which will result in a smaller diffraction efficiency for smaller beam diameters.

Table 4.1: Dependence of diffraction efficiency and modulation bandwidth from the AOM datasheet [7]. .

Beam diameter	125 μm	200 μm	400 μm
Modulation Bandwidth BW_{AOM}	19 MHz	12 MHz	6 MHz
Diffraction Efficiency	65 %	80 %	90 %

As a trade off between diffraction efficiency and modulation bandwidth a beam diameter of about 200 μm should be chosen.

For the used VCO model the expected modulation bandwidth is determined by electronic low pass filters and $BW_{VCO} = 5$ MHz is given in the datasheet as typical value.

4.3.4 Measurement of the Modulation Bandwidth

With the sensitivity constant K_{VCO} of the VCO, its output voltage can be written as

$$V_{out} \propto \sin(\phi(t)) = \sin\left(2\pi \int K_{VCO} \cdot V(t) dt\right).$$

If the input voltage has a constant DC- and a modulation (*mod*) AC-part the VCO output will be

$$V_{out} \propto \sin\left(2\pi f_{carrier} t + \underbrace{\frac{K_{VCO} \cdot V_{mod}}{f_{mod}}}_{=:m} \cdot \sin(2\pi f_{mod} t)\right).$$

The strength of the modulating signal is given by the modulation index m .

The modulated spectrum is described by Bessel functions, which appear as sidebands to the carrier at multiples of the modulation frequency f_m

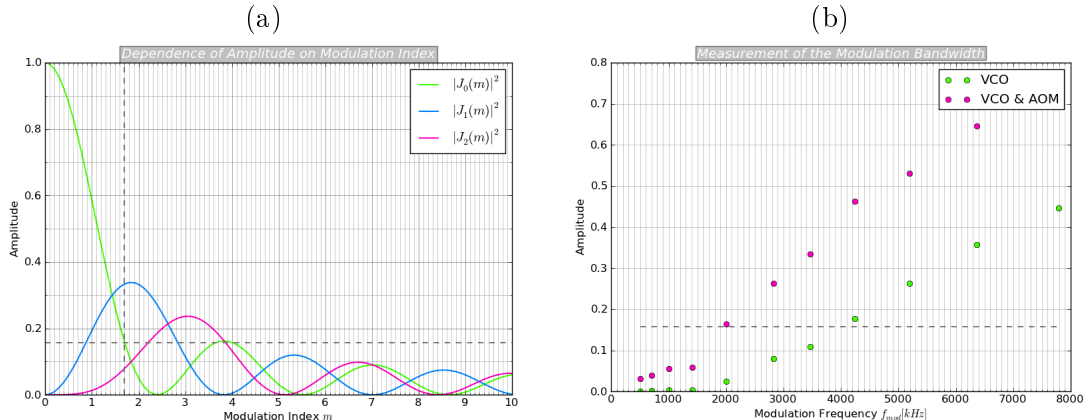
$$e^{i(\omega t + m \sin(\omega_m t))} = e^{i\omega t} \sum_{n=-\infty}^{\infty} J_n(m) e^{in\omega_m t}.$$

The carrier amplitude is given by the $J_{n=0}(m)$ -function, which can be displayed on a spectrum analyzer. When a modulation of strength m is applied, the carrier amplitude decreases. Vice versa the suppression of the carrier can be used to determine the modulation index m , as suggested in [41].

When the bandwidth limit is approached the resulting modulation begins to deviate from the modulation index m calculated from the used modulation frequency f_{mod} and voltage V_{mod} . When the modulation index m decreases to $\frac{1}{\sqrt{2}} = 0.7$ of the desired value the bandwidth limit is reached.

As an initial value a suppression following from a modulation index of approximately $m = 2.4$ is chosen. Now the modulation frequency f_{mod} is increased the ratio $f_{mod}/V_{mod} \propto \beta$ is kept constant. The carrier amplitude seen on the spectrum analyzer is recorded and set into ratio with the unmodulated $J_0^2(0)$ amplitude. The result for a purely electronic circuit, containing only the VCO, and a circuit which contains VCO and AOM can be seen in figure 4.5.

Figure 4.5 Measurement of the modulation bandwidth of VCO and AOM: The amplitude of the carrier for different modulation frequencies f_{mod} at a constant modulation index m (b). The change in the carrier amplitude with the modulation index m is described by $|J_0(m)|^2$ (a). The modulation index will decrease due to reaching the bandwidth limit.



From figure 4.5 (a) follows that the point where the modulation index reaches $0.7 \cdot 2.4 = 1.68$ the amplitude of the carrier has reached 15.7 % of its initial amplitude. In figure 4.5 (b) it can be seen that the amplitude of 15.7 % of the initial amplitude indicates a bandwidth of

$$BW_{VCO} \approx 4.1 \text{ MHz} \quad BW_{AOM\&VCO} \approx 2 \text{ MHz.}$$

4.3.5 AOM as Dead Time Element

The electronic control signal is transferred to the optical signal by modulation of the soundwave which is travelling through the acousto optical modulator. The soundwave speed of $4.2 \text{ mm}/\mu\text{s}$ ($\sim 1.4 \cdot 10^{-5}c$, c : speed of light) is very small compared to the signal speed on electronic lines ($\sim 0.6 \cdot c$) and optical paths ($\sim c$).

Depending on the way from the transducer to the focussed optical beam the signal will experience a delay. Additionally it needs time to transit the beam diameter d which will appear as a rise time.

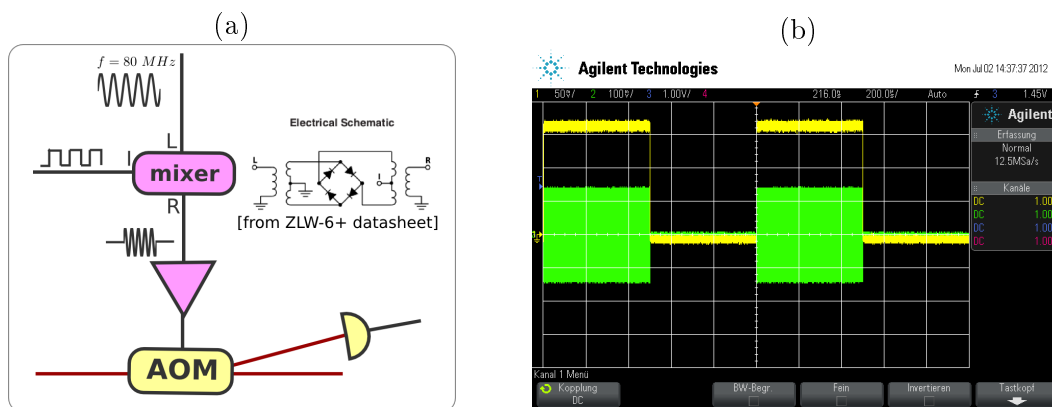
Therefore, the AOM is acting as a delay line in the setup, described by a transfer function of a dead time element [23]

$$\propto e^{-sT_{\text{travel, AOM}}}.$$

For measurement of the travelling time a gated 80 MHz voltage generated with a mixer is used, as shown in figure 4.6. Usually the L and R port of the mixer are used as inputs for AC voltages and the I port provides their multiplied output. To gate an oscillating signal with a square voltage, the DC voltage has to be applied to the I port, since the transformer stages inside the mixer react only to voltage changes³.

The used setup for the delay time measurement is shown in figure 4.6.

Figure 4.6 Measurement of the signal travelling time inside the AOM: A gated 80 MHz signal is generated with a mixer and the intensity in the first diffraction order is monitored (a). The gated 80 MHz signal (green) and intensity in the first diffraction order (yellow) are observed on an oscilloscope (b).



This method measures only the delay caused by the AOM, while the VCO might cause dead time as well. By driving the VCO with a square voltage its frequency will jump between 80 MHz (center frequency of the AOM) and about 72 MHz. Operation at the lower frequency causes the intensity in the first diffraction order to change, since it is

³The control of the signal amplitude by the mixer has a small switching time of 30 ns compared to an element like the Voltage Controlled Attenuator (for instance VCA ZX73-2500) with switching times of 14 to 25 μs . It can be used for intensity stabilization and control with a high bandwidth.

away from the AOM center frequency.

By comparing the delay measured with this method to the delay measured with the mixer, a delay of 35 ns can be attributed to the VCO.

With both methods the AOM can be realigned to optimize the travelling time and one obtains (figure 4.7) before and after realignment an overall (VCO+AOM) delay time of

$$\tau_{delay, before} = 480 \text{ ns} \quad \tau_{delay, after} = 270 \text{ ns} .$$

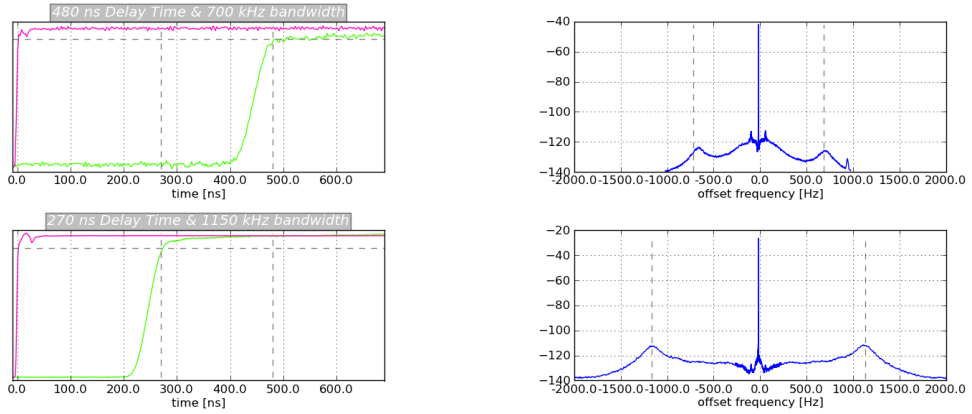
As demonstrated in section 2 the dead time element will cause the phase margin of the PLL to shrink by adding a factor $e^{i2\pi f_{offset}\tau_{delay}}$ to the open-loop transfer function $G(s)$, which causes a shift of the servo bump. The measured servo bump positions are shown together with the measured delay times in figure 4.7. The servo bumps show up at

$$SB_{before} = 700 \text{ kHz} \quad SB_{after} = 1150 \text{ kHz} .$$

This indicates that the transfer functions of the other elements have a large phase reserve and the loop needs an additional phase of about 110° to change the sign of $G(s)$ and create the servo-bump in the spectrum.

Figure 4.7 With the setup shown in figure 4.6 the delay of the intensity in the first diffraction order to the square voltage is measured (upper left $\tau_{delay, before} = 480 \text{ ns}$, lower left after realignment $\tau_{delay, after} = 270 \text{ ns}$).

Then the PLL is switched on again and the spectrum of the beat signals recorded. The servo-bump position is indicated as dashed line for the measurement with $\tau_{delay, before}$ (upper right) and $\tau_{delay, after}$ (lower right).



In figure 4.7 the signal does not show only a delay, but also a finite rise time. The rise time, that the signal needs to rise from 10 % to 90 % of its final value is connected to the beam diameter d inside the AOM crystal by [4]

$$T_{rise} = \frac{0.66d}{v_{sound}} .$$

The observed rise time of about $T_{rise} \approx 40 \text{ ns}$ gives with the sound velocity $v_{sound} = 4.2 \text{ mm}/\mu\text{s}$ a beam diameter of $d \approx 250 \mu\text{m}$ at which diffraction efficiency and modulation bandwidth show a good trade off (see table 4.1)

4.4 | Phase Frequency Detector

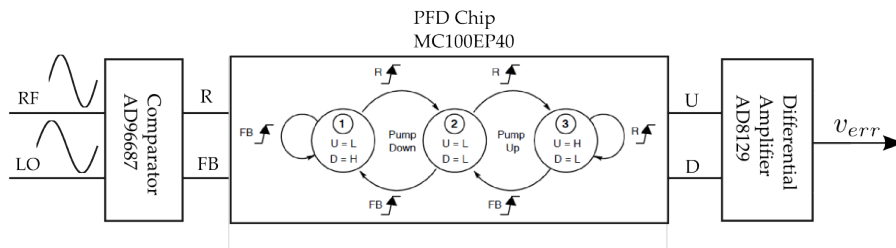
At the heart of a Phase Locked Loop lies the Phase Frequency Detector, which compares the instantaneous signal with the reference. It will create an error-voltage which is connected to the found difference. This error signal is provided to the filter.

The Phase Frequency Discriminator (PFD) is based on a design from Professor Marco Prevedelli (Università di Bologna).

PFD Working Principle

The internal setup of the PFD is shown in figure 4.8. It has two inputs (RF and LO) which are digitalized by a comparator. The actual PFD chip is represented by its logic diagram from the datasheet. The output of the PFD chip is subtracted by a differential amplifier. Its output voltage v_{err} contains the phase and frequency information between RF and LO.

Figure 4.8 Internal setup of the PFD designed by Professor Marco Prevedelli (Università di Bologna). The logic diagram of the PFD chip is taken from the datasheet [9]).



The logic model of the PFD chip tells when its output U , D pins will be in a low L or high H state. This depends on the rising edges on the input channels R and FB .

Assuming that the initial state of the chip is state 2 ($U = L$, $D = L$) it will change to state 1 and change $D = H$ if first a rising edge on the FB channel is registered and to state 3 ($U = H$), if the rising edge appears first on the reference input R . It will stay in the respective state until a rising edge on the opposite pin is measured and return to the initial state 2.

The signal on different stages in the PFD is shown in figure 4.9.

The phase detector output has a periodicity of the frequency difference between RF and LO input.

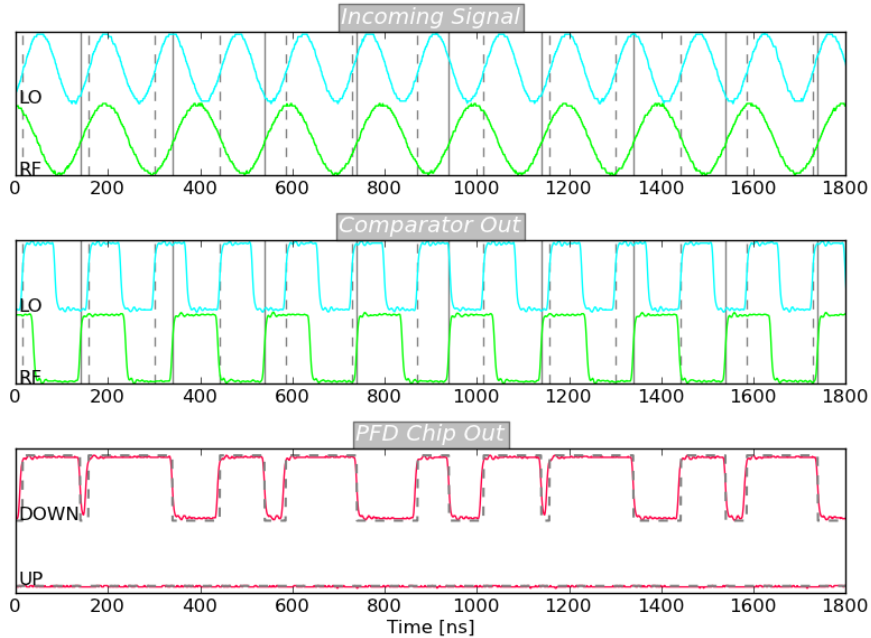
The differential amplifier (DA) will subtract the output of the up and down pin of the PFD chip:

$$DA_{out} = UP - DOWN$$

When integrated this voltage can be used as a feedback for the local oscillator. In the case shown in figure 4.9 the output v_{err} will be a negative voltage with period of the frequency difference. The voltage controlled oscillator will therefore decrease its frequency upon receiving the negative voltage as feedback. As the frequency of the local oscillator decreases in turn the periodicity of the error signal will decrease until the frequency of local oscillator and reference is the same.

If the frequency drops further, below the one of the reference, the PFD will be in pump up mode and the feedback voltage is positive, such that the frequency is increased again. When local oscillator and reference have the same frequency a frequency lock has been achieved.

Figure 4.9 The first (upper) plot shows the measured incoming signals at the LO and RF port. LO has a larger frequency than RF. The second plot shows the measured comparator output for the LO and RF signals. The rising edges of the comparator output are indicated by vertical lines. The third plot shows the measured output of the PFD at the UP and DOWN port and in dashed lines the expectation according to the logic model of the PFD chip.



PFD Measurement of Sensitivity Constant

Once the frequency lock has been achieved, the error voltage has to contain information about the phase difference of local oscillator and reference. Since there is no more frequency difference, the PFD output voltage will not have a periodicity, but it is a DC voltage proportional to the phase difference.

In the case of no phase difference, the rising edges perfectly coincide and UP and DOWN pin will both be low. When the phase of the reference advances a bit, the device will be pulled into Power-Up mode and the UP pin will be high till the rising edge of the local oscillator is registered. The integrated differential voltage UP-DOWN will then increase to a positive DC value.

As the phase advance increases the UP pin will stay longer in its higher state. When the phase advance is a 180° , the up pin will be all the time in its upper state and the averaged differential output will be

$$DA_{out} = V_{high} - V_{low} = 400 \text{ mV}$$

where V_{high} and V_{low} can be found in the PFD chip (Model MC100EP140) datasheet. When the reference lags the local oscillator the output voltage will be negative until it saturates for -180° phase difference at -400 mV .

The differential amplifier has a gain constant of $G = +10$ and the observed output is expected to vary between $\pm 4 \text{ V}$.

How the PFD output voltage changes with the phase difference is given by the "phase detector constant" K_ϕ [V/°]. By knowing this value one can connect the PFD output

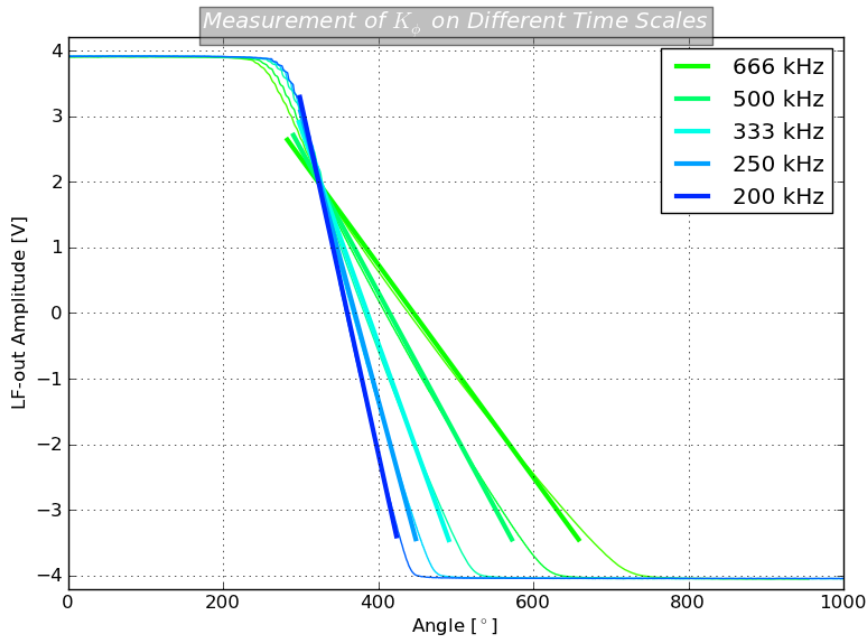
voltage in lock with the residual phase fluctuations. Furthermore, the transfer function of the PFD in the phase locked loop is given by K_ϕ .

K_ϕ can be estimated to vary between its maximum values at ± 4 V for a phase change of 360°

$$K_\phi^{estimation} = G \left(\frac{2(V_{high} - V_{low})}{360^\circ} \right) = 10 \cdot \frac{800 \text{ mV}}{360^\circ} = 22.2 \frac{\text{mV}}{^\circ}.$$

To measure the phase detector constant K_ϕ the two DDS channels are used as input. The output voltage of the PFD is monitored while a phase ramp from 0° to 360° is applied to one DDS channel. The ramping time t_{ramp} is written as a parameter into the RAM of the DDS and is therefore known ⁴ The recorded signal is the PFD output voltage versus time, which can be rescaled to PFD output voltage versus angle by applying a factor $360^\circ/t_{ramp}$. The result is shown in figure 4.10.

Figure 4.10 Measurement of the phase detector constant K_ϕ . Parameter is the ramp time t_{ramp} or equivalently frequency $f_{ramp} = \frac{1}{t_{ramp}}$.



In general the phase detector constant K_ϕ shows a frequency dependence, i.e. $K_\phi = K_\phi(f)$ [34]. The variations of K_ϕ for ramping times in the 100 kHz region were found to be the largest and are shown in the figure. From several K_ϕ measurements for ramps occurring on different time scales a mean value of

$$K_\phi = (31 \pm 13) \frac{\text{mV}}{^\circ} = (1.8 \pm 0.7) \frac{\text{V}}{\text{rad}}$$

is found.

⁴Its value can be controlled by giving both DDS channels as input signals on a mixer. The mixed signal will indicate the ramping time by one full oscillation.

4.5 | Filter: PID Controller

A PID controller has three parts which provide the control voltage depending on the error voltage by acting Proportional ($K_P \cdot v_{error}(t)$) to it, on its change (Derivative $K_D \frac{d}{dt} v_{error}(t)$) or to its duration (Integral $K_I \int v_{error}(t) dt$). In the Laplace domain it can be written as [23, page 373].

$$v_{control} = \left(K_P + K_D \cdot s + K_I \frac{1}{s} \right) v_{error} = K_P \left(1 + \frac{1}{T_I s} + T_D s \right) v_{error}, \quad (4.4)$$

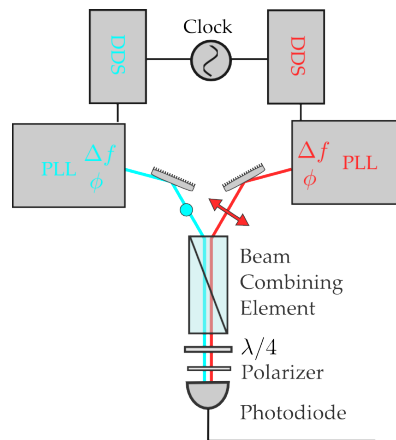
In the used controller (Vescent; model: D2-125) each of the three parameters K_P , T_I and T_D can be set independently to more than ten different values and the system response is dependent for each of them on the settings for the other two values. This offers a large parameter space for the tuning.

The goal is to tune the PID controller in a fashion that it will lead to a fast and stable response. This can be done by applying a quick change in one of the reference phases, such that the corresponding circular polarization should respond with an equivalent change in its phase.

A schematic of the setup used for tuning of the PID controller is shown in figure 4.11. For balanced intensities the resulting signal behind the $\lambda/4$ plate is linearly polarized, with a rotation angle θ , which is determined by the relative phase of the circular polarizations. Change of the relative phase will cause a rotation of the linear polarization that can be observed on a photodiode behind a polarizer as intensity variation. The dependence of the measured intensity on the rotation angle θ is not linear, since it is described by a $\cos^2(\theta)$ -function.

By rotation of the polarizer transmission axis to an angle of 45° to the polarization axis of the linear polarization, the expression can be expanded, so that the measured intensity change is proportional to the phase change in the circular polarization.

Figure 4.11 Each of the DDS reference channels controls one linear polarization via the PLL. The $\lambda/4$ plate translates the orthogonal linear into circular polarizations.



K_I on the PID controller is set to a small value, since the voltage controlled oscillator already includes an integrating part. The results of the tuning procedure are shown in figure 4.12.

Figure 4.12 A phase step is applied to one of the DDS channels and the system response is measured: The intensity change on the photodiode in figure 4.11 and the error signal from the PFD are monitored.

1) $K_I \approx 0, K_D = 0, K_P \approx 0$

Even before the step response the system doesn't show a steady zero error. The set value for the step is not reached

2) $K_P \uparrow$

The proportional action is increased, while integral and derivative part are kept zero. The system shows a large overshoot and oscillates around the set value. It comes to a steady value after about $50 \mu s$.

3) $K_D \uparrow$

By increasing K_D the system experiences more damping due to the derivative action on the change of the error signal. The settling time and the overshoot decrease. Still the rise time is large.

4) $K_P \uparrow$

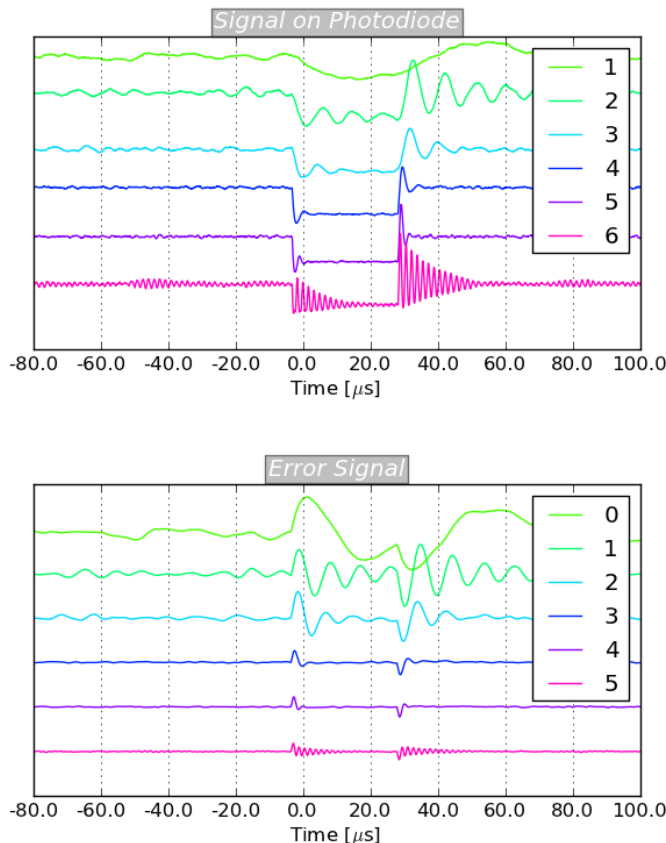
By increasing the proportional part the rise time of the system can be decreased, such that a sharper edge, which is more similar to a step response, becomes visible.

5) $K_D \uparrow$

Increasing K_D again shows again a decreased overshoot and a faster settling time. Increasing K_P and K_D iteratively will bring the system closer to the desired response.

6) *Critical Settings*

When K_P is increased to a point where the open-loop transfer function $G(s)$ of the system shows unstable behaviour the oscillations can no longer be damped. The gain has to be decreased till they can be fully damped out.



The proportional part has a coarse and a fine control, with a gain constant relative to the input error signal. The coarse gain can be varied in seven steps from -40 to +32 dB.

Around each step a fine tuner ± 6 dB can be used. From the settings of coarse and fine gain follows a proportional gain of

$$K_P \approx 5.$$

In general the transfer function of a PID controller has to take into account the limited bandwidth of the device as well. The used PID controller has a bandwidth of 10 MHz, which will have a small effect on the loop compared to the bandwidth of AOM and VCO (section 4.3).

4.6 | Summary

Each element in the phase locked loop has been characterised in this section regarding its transfer function and performance.

The references for both phase locked loops are realized by a Direct Digital Synthesis (DDS) solution, which offers the possibility for phase- and frequency-modulation and high relative phase stability of the output signals (section 4.1).

The achievable phase stability is limited by the signal to noise ratio of the detection on the photodiode. A minimum optical power of $53 \mu\text{W}$ per beam contributing to the beat signal (section 4.2) is estimated. This value holds for perfect beam overlap and intensity balance.

Controlled oscillator is the VCO and AOM combination with a sensitivity constant given by K_{VCO} . As the most crucial point the dead time caused by the travelling of the sound signal through the Tellurium Dioxide crystal inside the AOM is identified (section 4.3). The modulation bandwidth of VCO and AOM is discussed and measured by the carrier suppression during a modulation process.

By knowledge of the PFD constant K_ϕ , the achieved stability of the phase lock can be estimated conveniently by monitoring the error signal on an oscilloscope. When changes occur in the PLL, such as a frequency ramp of the reference, the PFD output indicates how well the optical signal follows the respective reference or if the lock is lost at some point.

The used filter is a PID controller which offers a large parameter space and a high bandwidth of 10 MHz. The tuning procedure for the controller is described in section 4.5.

$$K_\phi = (1.8 \pm 0.7) \frac{\text{V}}{\text{rad}} \quad K_{VCO} = \frac{1}{2\pi} (9.07 \pm 0.05) \frac{\text{rad}}{\text{s} \cdot \text{V}} \quad T_{dead} \approx 270 \text{ ns} \quad K_P \approx 5$$

5 | Analysis and Results

5.1 | Characterisation of the Phase Locked Loop

From the transfer functions and characteristics of the single components measured in chapter 4 the system transfer function $H(s)$ is calculated. $H(s)$ can be measured with help of the system step response and compared to the calculated transfer function.

5.1.1 Calculation of the System Transfer Function

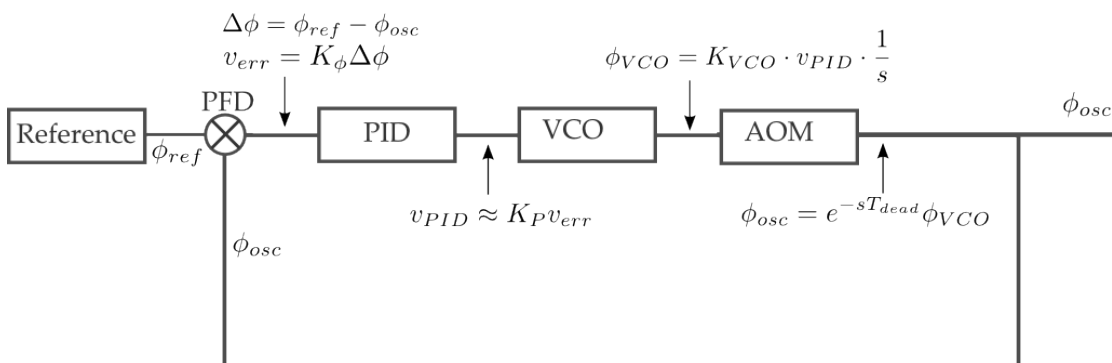
The open loop transfer function $G(s)$, introduced in section 2 is obtained by multiplication of the transfer-functions of the single components.

The dead time caused by the AOM is approximated by [23, page 312]

$$e^{-sT_{\text{dead}}} \approx \frac{1}{T_{\text{dead}}s + 1}.$$

Furthermore is assumed that the proportional gain K_P gives the main contribution to the PID controllers transfer function (section 4.5).

Figure 5.1 Diagram of the phase locked loop with the main transfer functions.



The open loop transfer function is obtained by the product:

$$G^{approx.}(s) \approx \frac{K_{\phi}K_PK_{VCO}}{s(T_{\text{dead}}s + 1)} = \frac{\mathcal{K}}{s(T_{\text{dead}}s + 1)} \quad \mathcal{K} = K_{\phi}K_PK_{VCO}. \quad (5.1)$$

From this the system transfer function can be calculated (section 2)

$$H(s) = \frac{G(s)}{1 + G(s)} \Rightarrow H^{approx.}(s) = \frac{\frac{\mathcal{K}}{T_{\text{dead}}}}{s^2 + 2 \cdot \sqrt{\frac{\mathcal{K}}{T_{\text{dead}}}} \cdot \frac{1}{2\sqrt{T_{\text{dead}}\mathcal{K}}}s + \frac{\mathcal{K}}{T_{\text{dead}}}}. \quad (5.2)$$

By identifying $\omega_n^2 = \mathcal{K}/T_{\text{dead}}$ and $\zeta = \frac{1}{2\sqrt{T_{\text{dead}}\mathcal{K}}}$ equation 5.2 can be written in the “standard form of a second order system” [29, page 176]:

$$H^{2nd\ order}(s) = \frac{\omega_n^2}{s^2 + 2\zeta\omega_n s + \omega_n^2}. \quad (5.3)$$

A second order system with with a system transfer function of the form of equation 5.3 can be described by just two parameters, the

damping ζ and natural frequency ω_n .

Since all system parameters have been measured or estimated in chapter 4 (page 49) the natural frequency and the damping can be calculated from these

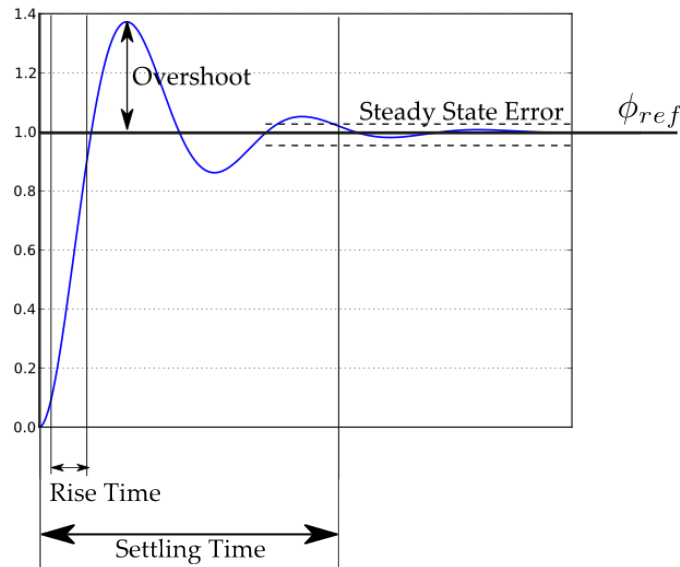
$$\zeta^{calc} = \frac{1}{2\sqrt{T_{dead}\mathcal{K}}} = (0.27 \pm 0.05) \quad \omega_n^{calc} = \sqrt{\frac{\mathcal{K}}{T_{dead}}} = (7 \pm 1) \text{ MHz}. \quad (5.4)$$

5.1.2 Method: Step Response Characteristics

The quality of the step response can be quantified by four parameters:

- **Rise Time** The output rises beyond 90 % of the desired value for the first time. The rise time should be as short as possible, such that the system responds fast and minimizes the difference to the reference again.
- **Overshoot** Peak level in the step response compared to the set value. Since the desired shape is a step, the overshoot should be as small as possible.
- **Settling Time** The time it takes to converge to the steady state. A common definition is to define the signal as settled when it stays within the 2 % or 5 % region of the set value [29].
- **Steady State Error** The difference between the steady-state and the desired output for $t \rightarrow \infty$.

Figure 5.2 Illustration of a typical step response function with characterising parameters.



From the phase step response the system transfer function can be obtained:

In the Laplace domain a unit step of the reference signal $\phi_{ref}(s)$ is described by

$$\phi_{ref}(s) = \mathcal{L}\{\phi_{ref}(t)\}^{\text{unit step}} = \int_0^{\infty} e^{-st} dt = \frac{1}{s},$$

which gives a connection of controlled oscillator and system transfer function

$$H(s) = \frac{\phi_{osc}(s)}{\phi_{ref}(s)} \Leftrightarrow \phi_{osc}(s) = \frac{1}{s} H(s).$$

Additionally it can be used that taking the derivative in the time domain leads to multiplication with a factor s in the Laplace domain, then

$$H(s) = \mathcal{L}\left\{\frac{d}{dt}\phi_{osc}(t)\right\}(s). \quad (5.5)$$

A stable system will converge to a steady state and the derivative $\frac{d}{dt}\phi_{osc}(t)$ will approach zero for $t \rightarrow \infty$. Therefore the Laplace transform can be replaced by the Fourier transform in this case [23].

5.1.3 Step Response Characteristics of a Second Order System

For a second order system overshoot and settling time can be directly related to the system parameters ω_n and ζ .

The expression for the step response in the time domain is obtained by Laplace transforming the step response with help of equation 5.5. It is given as [29, page 177]

$$C(s) = H(s)\frac{1}{s} \quad C(t) = \mathcal{L}^{-1}\{C(s)\} = 1 - e^{-\zeta\omega_n t} \left(\cos\omega_d t + \frac{\zeta}{\sqrt{1-\zeta^2}} \sin\omega_d t \right), \quad (5.6)$$

with $\omega_d = \omega_n\sqrt{1-\zeta^2}$.

Maximum Overshoot

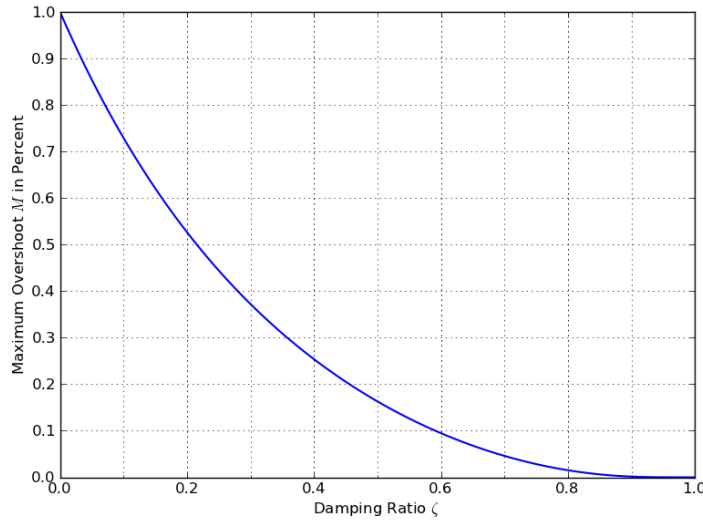
At the point of the maximum overshoot the function $C(t)$, which describes the step response, reaches its maximum value. This is the case for $\omega_d t_M = \pi$ (and odd integer multiples).

The resulting overshoot in percent is

$$M = C(t_M) - 1 \stackrel{t=\pi/\omega_d}{=} e^{-(\zeta/\sqrt{1-\zeta^2})\pi}$$

The maximum overshoot depends only on the damping ratio ζ and the dependence is shown in figure 5.3.

Figure 5.3 For a second order system the damping ratio ζ can be directly obtained from the overshoot in the step response.



Settling Time

The step response $C(t)$ given in equation 5.6 has an envelope $1 - e^{-\zeta\omega_n t}$. Since the oscillating part will always stay within the envelope, the settling time can be expressed in terms of the envelope function. To stay within the 2% region around the set value the signal needs the settling time [29, page 183]

$$e^{-\zeta\omega_n t_{settle}} \approx 0.02 \quad \Rightarrow \quad t_{settle} \approx \frac{4}{\zeta\omega_n}. \quad (5.7)$$

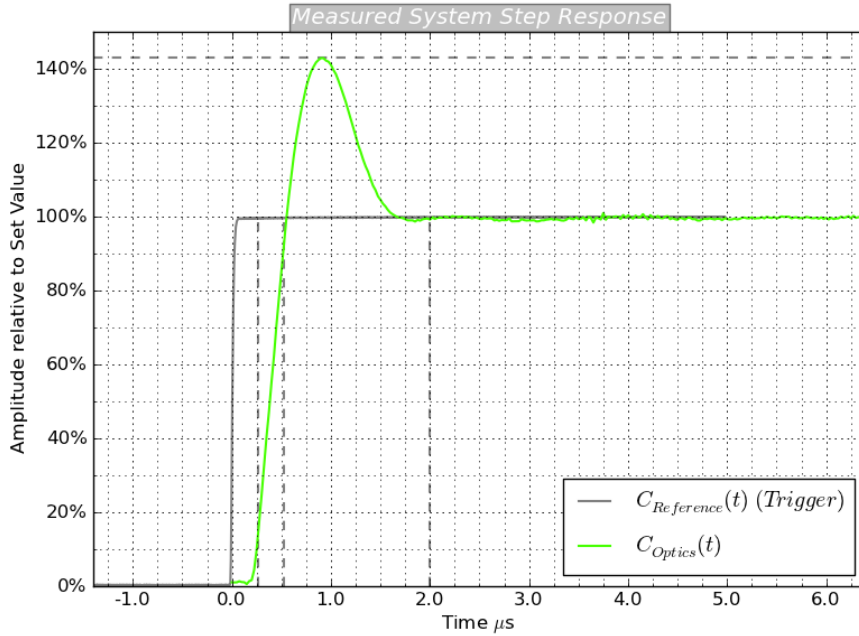
Both, settling time and overshoot reach better values for larger damping ratio, the optimum region for ζ lies around $\zeta_{opt} = 0.76$ [29, page 183].

For a second order system the natural frequency ω_n and the damping ζ can be calculated from overshoot and settling time of the step response.

5.1.4 Measurement of the Step Response

Basically the step response is already used for the tuning of the PID controller with the setup introduced on page 47, but in a very qualitative way. With the same setup as used on page 47 the rotation of the resulting linear polarization, i.e. the system step response can be observed when a phase step is applied to one of the reference channels. The recorded phase step response of the optical system is shown in figure 5.4.

Figure 5.4 A phase step $0 \rightarrow 20^\circ$ is applied to one of the reference channels. A part of the references is used as a trigger signal relative to which the delay of the step response of the PLL is measured.



The rise time to the 10 % value $t_{10\%} = 260$ ns is approximately the dead time expected for the system.

From the measured overshoot and settling time the parameters for the description as a second order system can be calculated

$$M = (43 \pm 2)\% \xrightarrow{\text{Figure 5.3}} \zeta = 0.26 \pm 0.02$$

$$t_{settle} = (2 \pm 0.25)\mu s \xrightarrow{\text{Equation 5.7}} \omega_n = (7.7 \pm 1.0) \text{ MHz}$$

These values can be compared to the ones obtained from the approximation as a second order system calculated in equation 5.4 (page 51):

$$\begin{aligned} \omega_n^{\text{step response}} &= (7.7 \pm 1) \text{ MHz} & \omega_n^{\text{calc.}} &= (7 \pm 1) \text{ MHz} \\ \zeta^{\text{step response}} &= (0.26 \pm 0.02) & \zeta^{\text{calc.}} &= (0.27 \pm 0.05). \end{aligned}$$

The agreement between the calculated second order system parameters and the ones obtained from the step response is remarkable. For the approximation as a second order system four parameters are still contained in the open-loop transfer function (K_ϕ , K_P , K_{VCO} and T_{dead}) and the PID controller and the dead time transfer function are only

described in approximation. These approximations seem valid and the measured parameters should all be in the right order of magnitude. Otherwise such an agreement would be unlikely.

The description as a second order system is convenient. For instance from equation 5.4 (page 51) follows that the damping parameter $\zeta \propto 1/\sqrt{T_{\text{dead}}}$. This explains why the overshoot M (figure 5.3) can not be eliminated in the tuning process.

5.1.5 Transfer Functions of the Phase Locked Loop

The un-approximated transfer function from which bandwidth and phase stability can be calculated, is obtained from the step response of the phase locked loop.

To investigate the exact influence of the AOM-dead time, the step response of the circuit with AOM is compared to the one of the purely electronic loop:

In this case the output signal of the VCO does not drive the AOM, but its output is directly connected to the PFD, i.e. it substitutes the beat signal recorded on the photodiode.

The AOM contributes the largest amount of the dead time T_{dead} , compared to which the dead time in the electronic loop without AOM is negligible, i.e.

$$\text{electronic loop: } e^{-sT_{\text{dead}}} \approx 1.$$

In the schematic (figure 5.1, page 50) the oscillator VCO+AOM would for this case be only the VCO.

By comparison of the electronic loop without AOM and the full phase locked loop ("optical" in the following) the influence of the dead time can be quantified.

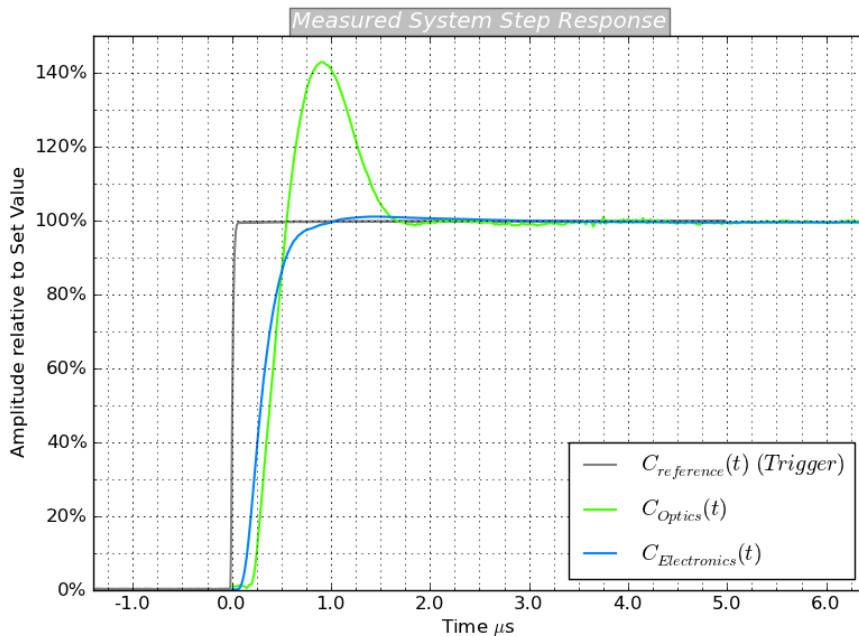
System Transfer Function $H(s)$

The phase step response for the electronic loop only (situation without AOM) and the optical loop is shown in 5.5. The step response for the optical system is the same as shown in figure 5.4.

For the electronic loop without AOM the overshoot is only $M = 2\%$ which indicates a damping value of $\zeta \approx 0.78$. This step response shows a short settling time of about 800 ns into the 2 % set value region. It indicates good tuning of the PID controller since the settling time has an absolute minimum at $\zeta = 0.76$ [23, page 183].

Remarkable is that the optical signal crosses the 90 % value at the same time with the electronic signal, even though it crosses the 10 % value 100 ns later. This again shows the low damping of the optical signal compared to the electronic one.

Figure 5.5 Step response function of the electronic loop without AOM and the full loop with AOM.



The system transfer function $H(s)$ is obtained by Fourier transformation of the derivative as shown on page 52

$$H(s) = \mathcal{F} \left\{ \frac{d}{dt} C(t) \right\}.$$

Figure 5.6 Derivative of the step response functions of electronic circuit without AOM and optical circuit with AOM.

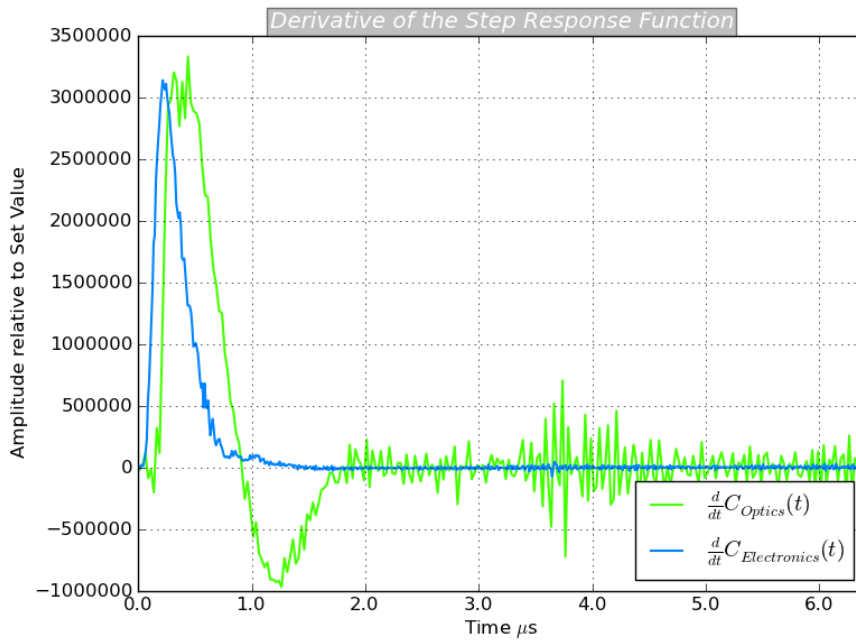
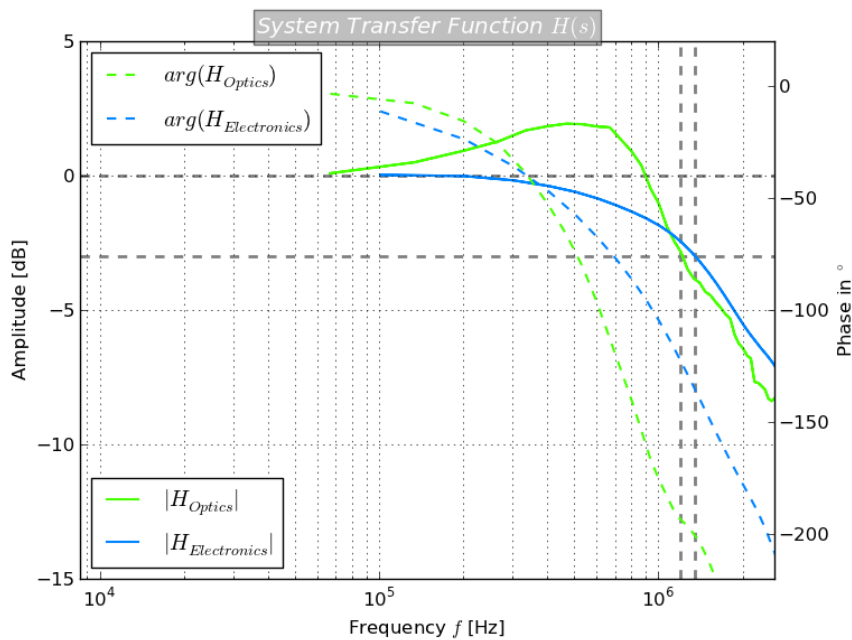


Figure 5.7 From the step response the transfer function $H(s)$ is calculated for the electronic circuit without AOM and optical circuit with AOM.



The -3 dB value from the system transfer function indicates the bandwidth of the loop. It can be found at

$$f_{\text{electronics}}^{-3dB} = 1.35 \text{ MHz} \quad f_{\text{optic}}^{-3dB} = 1.2 \text{ MHz}$$

and is therefore not very different to the one obtained for the electronics alone. The largest influence of the AOM consists in the phase decrease by the dead time. At 1 MHz the phase of the system transfer function with the AOM is decreased by 70° compared to the one where only the electronics with small dead times contribute.

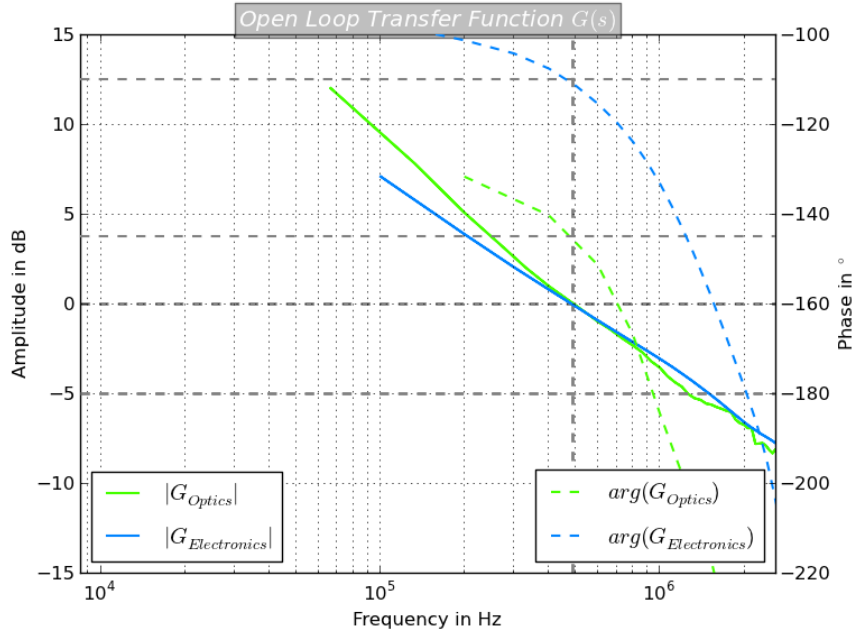
Open Loop Transfer Function $G(s)$

From the system transfer function $H(s)$ the open loop gain can be calculated

$$G(s) = \frac{H(s)}{1 - H(s)}. \quad (5.8)$$

Its absolute value and phase are plotted in figure 5.8.

Figure 5.8 Open-loop transfer function obtained from equation 5.8 and the measurement of $H(s)$ by the step response function.



The crossing frequency for which the open loop gain $|G(s)|$ is unity, lies at 487 kHz. The stability of the system depends on the phase margin at this point, which can be read off from the plot as

$$\varphi_{\text{electronics}}^{\text{margin}} = 180^\circ - 110^\circ = (70 \pm 2)^\circ \quad \varphi_{\text{optics}}^{\text{margin}} = 180^\circ - 145^\circ = (35 \pm 2)^\circ.$$

The value for the phase margin of the optics estimated by the overshoot in the step response was $(27 \pm 2)^\circ$, which is not in agreement, but very close to the actual value.

The additional dead time caused by the AOM was measured in section 4.3 to be $T_{\text{AOM, dead}} = (270 \text{ ns} - 35 \text{ ns}) = 235 \text{ ns}$. At the cross frequency this should cause an additional phase compared to the electronic circuit of

$$\Delta\varphi_{\text{expected}}^{\text{additional}} = 2\pi \cdot 487 \text{ kHz} \cdot 235 \text{ ns} \approx 40^\circ \quad \Delta\varphi_{\text{measured}}^{\text{additional}} = 145^\circ - 110^\circ = 35^\circ,$$

which is approximately the value found in figure 5.8.

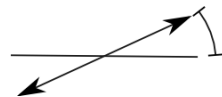
5.2 | Resulting Frequency Controllability

An actual transport sequence with the direct synthesis scheme would involve a frequency ramp in one of the reference channels, such that the circular polarizations have a resulting frequency difference Δf .

This would lead to a phase difference $\Delta\varphi$ which is linear in time

$$\Delta\varphi(t) \propto \int_0^t \Delta f dt' = \Delta f t.$$

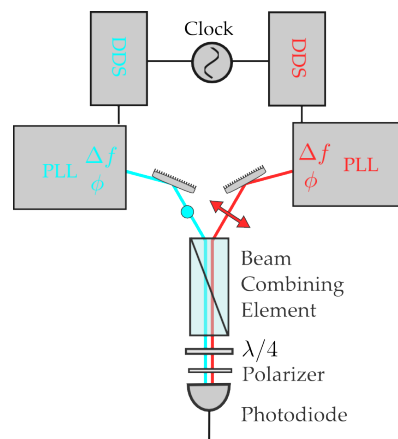
Overlapping two circular polarization creates a linear polarization (see page 9). The relative phase $\Delta\phi$ between the circular polarizations determines the rotation angle θ of this linear polarization:



$$\vec{e}_{\text{lin}, \theta} = \frac{1}{\sqrt{2}} (e^{i\Delta\varphi} \vec{e}_{\sigma+} + \vec{e}_{\sigma-}), \text{ where } \theta = \frac{\Delta\phi}{2}.$$

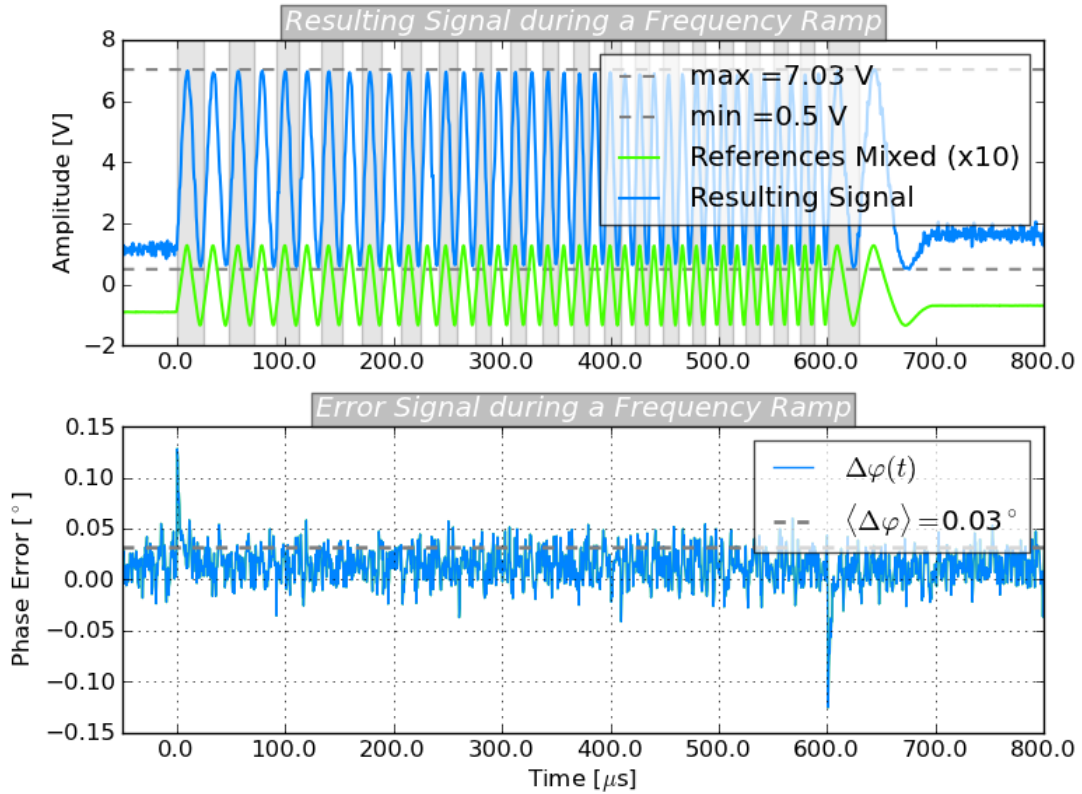
A frequency difference Δf between the two circular polarizations therefore causes a continuous rotation of the linear polarization, that can be measured with the setup shown in figure 5.9.

Figure 5.9 Setup for the measurement of the rotation of the linear polarization: Each of the DDS reference channels controls one circular polarization. Overlapping the circular polarizations creates linear polarization. Changes in the relative phase of the circular polarization can be monitored by placing a polarizer and a photodiode behind the quarter wave plate.



Initially both DDS channels run on 80 MHz, then a frequency ramps up to $\Delta f = 250\text{kHz}$ and down after about $600 \mu\text{s}$ is driven. A part of the DDS output is monitored together with the generated linear polarization and the error signal of the ramped channel. The result is shown in figure 5.10.

Figure 5.10 In the setup shown in figure 5.9 a frequency ramp is applied to one of the references. "References Mixed(x10)": A small part of each reference is used to monitor the frequency ramp. For this the reference channels are multiplied by a mixer and the resulting signal is low pass filtered. This leads to a signal oscillating at their frequency difference to each other. "Resulting Signal": The signal recorded on the photodiode. Its maximum and minimum values are indicated by dashed lines. Lower Plot: To see if the lock is lost at any point the error signal (PFD output) of the ramped channel is monitored during the ramp.



When the reference starts the frequency ramp the error signal rises up to about five times of its rms value. A zoom into the error signal shows that after $5 \mu\text{s}$ the optical signal follows the reference signal, so the error has been tracked out. The larger error at the beginning of the sequence might be due to adjusting the I -part of the PID controller not to a high enough value. Nevertheless, one should notice, that the achieved rms phase stability of the optical to the DDS signal in this measurement is exceptionally good and the excursion is one the order of a tens of a degree.

The intensity dependence on the polarization angle θ follows $\cos^2(\theta)$. Every turning of 180° of the tuning angle is indicated by a white or a gray bar in figure 5.10. Expected is a rotation of the polarization with half the frequency detuning Δf between the reference channels. In the middle of the ramp one can measure the time span (a white and a gray bar) for a full rotation of 360° and finds a rotation frequency of roughly 125 kHz as expected.

Since the reference channels are mixed the resulting signal oscillates with the cosine of the sum and the difference frequency, where the sum frequency of 160 MHz exceeds the oscilloscope bandwidth and is not visible therefore.

An important point to note is that only the overlapped and intensity balanced part of the σ^+ and the σ^- beams will result in the turning linear polarization, while the other part will

prevent the signal from reaching the absolute minimum near zero when the polarization of the resulting linear polarization is perpendicular to the one of the polarizer. Another possibility to produce such a signal, would be that the turning of the polarization is malfunctioning in the fashion, that only a part of the beam is actually phase controlled and the spatial distribution of σ -polarizations with different phases would result in the underground. Especially in the situation where the modulation happens on short time scales this might happen.

This can be excluded in the following way: The spatial quality of each circular polarization is monitored with a beam profile camera behind the analyzer. This is done by blocking the other, orthogonal polarization and rotation of the analyzer. For a perfect circular polarized beam, no intensity variation is visible as discussed in chapter 3. If the beam intensity changes uniformly and within the upper limit calculated in the characterization of the quarter wave plate, each beam can be considered to have a good spatial quality. Now both channels are opened and the analyzer is rotated slowly, while the intensity is monitored again with the photodiode. If the upper and the lower limit (i.e. the visibility of the signal) is the same as for rotation of the light polarization itself on the shorter timescale, only the imperfect overlap of the beams is causing the underground and not loss of phase control by the PLL.

In this measurement the visibility during the frequency ramp is 86.7 % and was checked with the method above to be within 2-3% of this value for manual rotation of the analyzer.

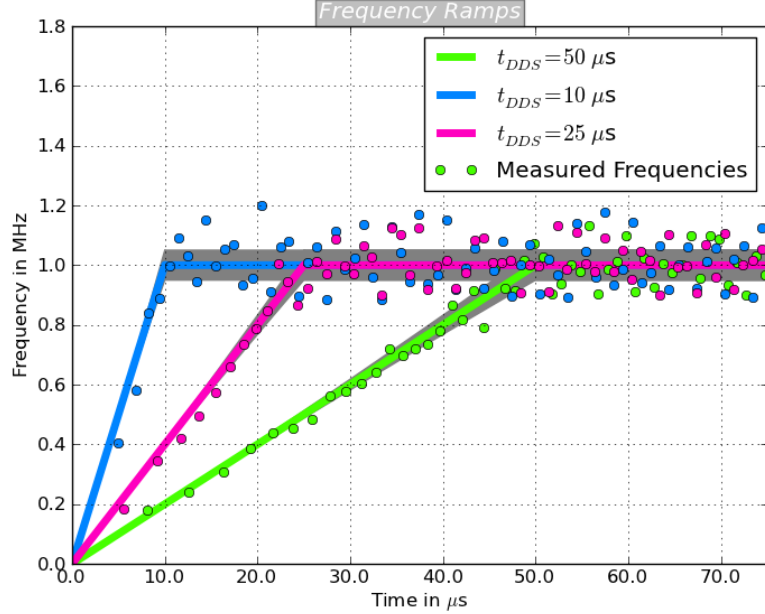
Following $f(t)$

It is interesting to follow the evolution of the instantaneous frequency for ramps on the relevant time scale of μs . The desired final frequency would be about 100 kHz in experiments where atoms should be transported (see section 1.2.3). The problem is, that a 100 kHz signal performs only one oscillation in $10 \mu s$, therefore it is difficult to track the instantaneous frequency with this final frequency.

Instead a final frequency of 1 MHz is chosen. If the loop can follow this frequency ramp in $10 \mu s$, it is also able to follow a 100 kHz ramp in the same time. The measurement result is shown in figure 5.11.

Overall the found frequencies of the resulting signal follow the expectation from the function implemented into the reference. Since typical frequency detuning Δf lies in the order of $1/10$ of the detuning tested here (see section 1.2.3), it can be inferred that the PLL is able to follow the desired frequency ramps.

Figure 5.11 The solid lines indicate the frequency-vs-time function written into the RAM of the DDS. Three different ramp times t_{DDS} to the frequency difference of $\Delta f = 1$ MHz are measured. The optical signal is expected to follow this reference signal. The oscillations of the signals during the ramp (as in figure 5.10) are recorded. From them the instantaneous frequency can be extracted. The found frequencies for the respective ramps are inserted as point in this figure. The expected fluctuations of the found frequencies due to the limited time resolution of the oscilloscope are indicated by the grey shaded areas around the desired paths.



5.3 | Resulting Phase Stability

5.3.1 Methods for Phase Noise Measurements

The power spectral phase noise density with and without stabilization can be measured with different methods [34]. Each method offers different advantages and is applicable in certain phase- and amplitude-noise regions. Two of them are used in the following.

5.3.1.1 Phase Noise Measurement with the Signal Spectrum

The spectrum of an ideal waveform $\propto \sin(\omega_0 t)$ is a δ -peak at the carrier frequency ω_0 which contains all the signal power

$$S_{ideal}(t) = \sin(\omega_0 t) \Rightarrow S_{ideal}(f) = \delta(\omega_0).$$

Now, if one supposes a phase modulation $\phi(t)$ at a frequency f_m and with amplitude m the resulting signal is

$$S_{mod}(t) = \sin(\omega_0 t + \underbrace{m \sin(2\pi f_m t)}_{\phi(t)}).$$

For this the mean square phase deviation can be calculated as

$$\langle \phi^2 \rangle = \lim_{T \rightarrow \infty} \frac{1}{T} \int_{-T/2}^{T/2} |\phi(t)|^2 dt = \frac{m^2}{2}.$$

The modulated spectrum $S_{mod}(f)$ is described by Bessel functions, which appear as sidebands to the carrier at multiples of the modulation frequency f_m . If the modulation is

small enough the higher order Bessel coefficients become negligible and the modulated signal can be written as

$$e^{i(\omega t + m \sin(\omega_m t))} = e^{i\omega t} \sum_{n=-\infty}^{\infty} J_n(m) e^{in\omega_m t} \stackrel{m < 0.4}{\approx} e^{i\omega t} \left[\frac{m}{2} e^{-i\omega_m t} + 1 + \frac{m}{2} e^{i\omega_m t} \right].$$

In this case two sidebands with power $m^2/4$ in each will appear. This power will be missing in the carrier. The amplitudes of the sidebands and the carrier are connected via the modulation index m by

$$\frac{P_{\text{single sideband}}}{P_{\text{carrier}}} = \frac{m^2}{4} = \frac{\langle \phi^2 \rangle}{2}.$$

A continuous noise spectrum can be "build up" by small modulations at different frequencies.

From this one can find a connection between the mean square phase deviation and integration over the normalized signal spectrum seen on the spectrum analyzer

$$\langle \phi^2 \rangle = \frac{\int_{\text{both sidebands}} P(\nu) [\text{dBm/Hz}] d\nu}{P_{\text{carrier}}} = \frac{2 \int_{\text{one sideband}} P(\nu) d\nu}{P_{\text{carrier}}} = 2 \int_{\text{one sideband}} P(\nu) [\text{dBc/Hz}] d\nu.$$

The unit dBc means that this spectrum has been normalized to the carrier amplitude. Alternatively this can be written in a "power fraction in carrier"-form [31]

$$\eta = e^{-\langle \phi^2 \rangle} = \frac{P_{\text{carrier}}}{\int_{-\infty}^{\infty} P(\nu) [\text{dBm/Hz}] d\nu}.$$

Conventionally the power located in the 1 Hz region around the carrier frequency is regarded as the carrier power. Therefore this region should be measured with a bandwidth of 1 Hz. It would take a long measurement time to acquire the whole spectrum - up to offset frequencies of some MHz - with such high resolution. Usually only the region around the carrier is measured with 1 Hz resolution. Then the span is increased and with it the resolution bandwidth RBW. In the end all measured spectra are normalized to their respective RBW value and combined as shown in appendix A.

The limit in which this approximation is still valid ($m < 0.4$) means that the suppression of phase noise signal compared to the carrier has to be better than -14 dB for all frequencies. This implies sufficient frequency stability, such that the carrier frequency stays at the same value.

Furthermore, this method is sensitive to amplitude fluctuations. In the case of the used external-cavity diode laser the amplitude noise is negligible compared to the noise added by elements in the optical path. To differ between amplitude and phase noise an I-Q measurement method can be used [34].

Another limit to this measurement method is the free dynamic range of the spectrum analyzer. The free dynamic range at a certain offset frequency gives the smallest signal that can be displayed together with a carrier of a certain strength. The effect of the dynamic range limit will be shown on page 67.

5.3.1.2 Phase Noise Measurement via the PFD output

If two input signals to the Phase Frequency Discriminator are frequency locked, the error voltage provided by the PFD is proportional to their phase difference. The used PFD provides the error signal on two outputs HF and LF. The difference between them is that LF (low frequency) contains a low pass filter. By comparing HF and LF it can be tested

up to which frequency offset their output is identical. Then error signal HF or LF can be used to obtain the phase noise spectral density

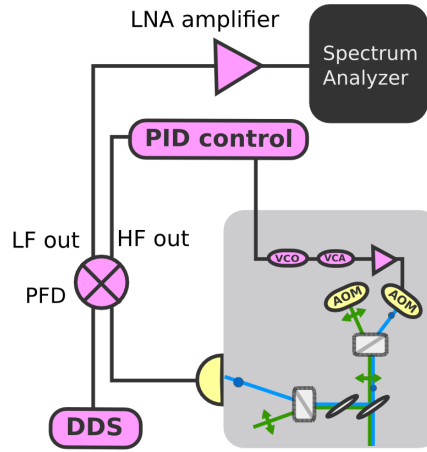
$$S_{\phi}(f) = |\mathcal{F}\{\phi(t)\}|^2$$

by measurement of the power spectral density of the output signal with a spectrum analyzer

$$S_V(f) = |\mathcal{F}\{V(t)\}|^2.$$

A possible setup is shown in figure 5.12.

Figure 5.12 Setup for the measurement of the relative phase noise between the oscillator and reference in locked condition: The HF output of the PFD is used to maintain the phase lock, the LF output for the phase noise measurement.



One advantage of this method compared to the beat signal method is that no carrier is present since for zero phase difference the voltage drops to zero as well. This avoids large requirements on the dynamic range of the spectrum analyzer. Furthermore, the output signal of the PFD shows only phase fluctuations between the signals and has no sensitivity to amplitude fluctuations.

On the other hand the measurement takes now place in the region around 0 Hz, where the spectrum analyzer has a large intrinsic $1/f$ noise peak.

Hence in this method a low noise pre-amplifier \triangleright is used. To obtain a meaningful result the noise floor of the spectrum analyzer and pre-amplifier and the amplification factor \triangleright have to be taken into account in the analysis.

The amplification constant of the low noise pre-amplifier can be measured by e.g. generating a low frequency (200 kHz) sinusoidal signal and observing one time the amplified version and one time the un-amplified version on the spectrum analyzer. The amplification can then be read of in dB.

The measurement of the system noise floor is done by termination of the amplifier input with its input impedance of 50Ω . The noise spectrum is recorded, so that it can be subtracted from the measured phase noise spectrum. The noise floor should be measured every time a phase noise spectrum is recorded: Spurious signals can vary in amplitude by up to 20 dB, depending on placing of components, cables and chosen amplification factor [34]

$$S_V(f) = |\mathcal{F}\{\phi(t) \cdot K_\phi \cdot \triangleright\}|^2 = K_\phi^2 \cdot \triangleright^2 \cdot |\mathcal{F}\{\phi(t)\}|^2.$$

To obtain the power spectral density with a high resolution and normalized to a 1 Hz bandwidth, several spectra with different spans are recorded and combined as shown in appendix A.

Finally the rms phase noise $\langle\phi^2\rangle$ is obtained by considering that it is connected to the spectral distribution by integration¹

$$\langle\phi^2\rangle = \int_{-\infty}^{\infty} S_\phi(f)df = 2 \cdot \int_0^{\infty} S_\phi(f)df.$$

Since the PFD measures the phase difference between the two input channels, their relative rms deviation $\langle\phi\rangle$ is given by contributions of local oscillator and reference

$$\langle\phi^2\rangle = \sqrt{\langle\phi_{LO}^2\rangle + \langle\phi_{REF}^2\rangle},$$

which are not common mode.

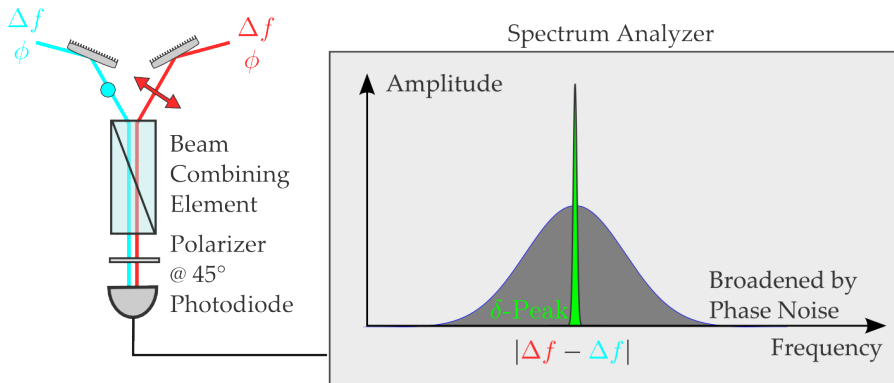
5.3.2 Phase Noise Measurements

To determine the quality of the lock, the phase noise spectral density $S_\phi(f)$ in lock is compared to the initial phase noise without lock. To obtain spectra the methods above are used.

Initial Phase Noise Spectrum

To determine the initial phase noise, a beat signal between the two interferometer arms is recorded as shown in 5.13. The AOM in each arm is driven directly (without phase locked loop) with the respective DDS channel. The resulting beat signal is centered at the carrier frequency, i.e. the frequency difference between the two AOMs.

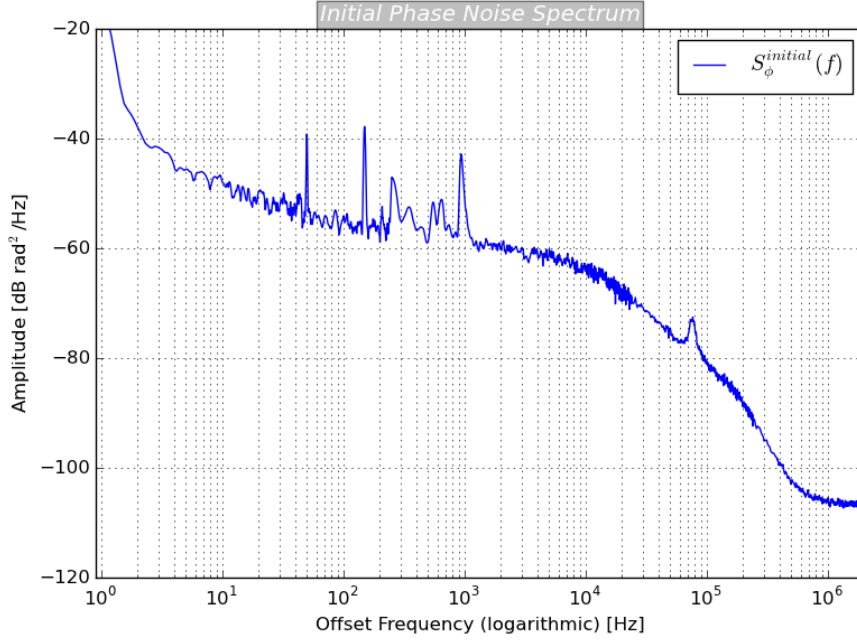
Figure 5.13 The (initial) phase noise between the interferometer arms is recorded with the beat signal spectrum.



With the signal spectrum method from section 5.3.1.1 the initial phase noise spectral density $S_\phi^{initial}(f)$ can be determined from the recorded beat signal. The result is shown in figure 5.14.

¹Actually the filter used by the spectrum analyzer is of a Gaussian form with a width given by the resolution bandwidth. The peak at 0 Hz will therefore "mask" the phase noise in this region, i.e. the spectral distribution will always be the one of the filter shape. Taking this into account, the integration starts at a lower limit of 1.2 Hz.

Figure 5.14 Measured phase noise spectrum $S_{\phi}^{initial}$.



The spectral distribution of the phase noise $S_{\phi}^{initial}(f)$ shows prominent spurious peaks at 50 Hz, which is caused by power supplies.

By integration over the whole spectrum an rms phase noise of

$$\langle \phi \rangle^{initial} \approx 12.5^{\circ}$$

is obtained. The largest part of the phase noise is concentrated in the region of up to 10 kHz, where acoustic and vibrational frequency are strong [28].

Critical for the state-dependent transport is the phase noise which occurs in the experimental time scale² of about 500 μ s, or equivalently a frequency of $f_{exp} = \frac{1}{500 \mu s} \approx 2$ kHz. In the relevant time scale starting from 2 kHz a rms phase noise of $\langle \phi \rangle_{2 \text{ kHz to } 1 \text{ MHz}} \approx 8.5^{\circ}$ is contained. According to the estimation in section 1.2.4 (page 11) the needed stability is better than

$$\langle \phi \rangle_{goal} \leq 1.7^{\circ}.$$

Relative phase noise of the reference channels

The phase noise of the resulting, phase locked signal is measured with the PFD method. It is obtained from the relative fluctuations of the reference channels to each other $\langle \phi \rangle_{DDS}$ and the fluctuations of the optical signal against each reference channel $\langle \phi \rangle_{opt. \text{ vs } DDS}$. The PFD method only measures phase fluctuations between two signals, which are not common mode. Therefore, each channel could still show large phase fluctuations, but when they are performed in both measured signal at the same time, they will not appear in the measurement.

The phase noise of each single channel could basically be measured with the signal spectrum method introduced in section 5.3.1.1. The measurement method relies on expression of the phase noise level relative to the carrier strength. It would be expected that the

²This is approximately the coherence time [18].

spectrum of one of the DDS channels shows a very strong carrier and only a small phase noise.

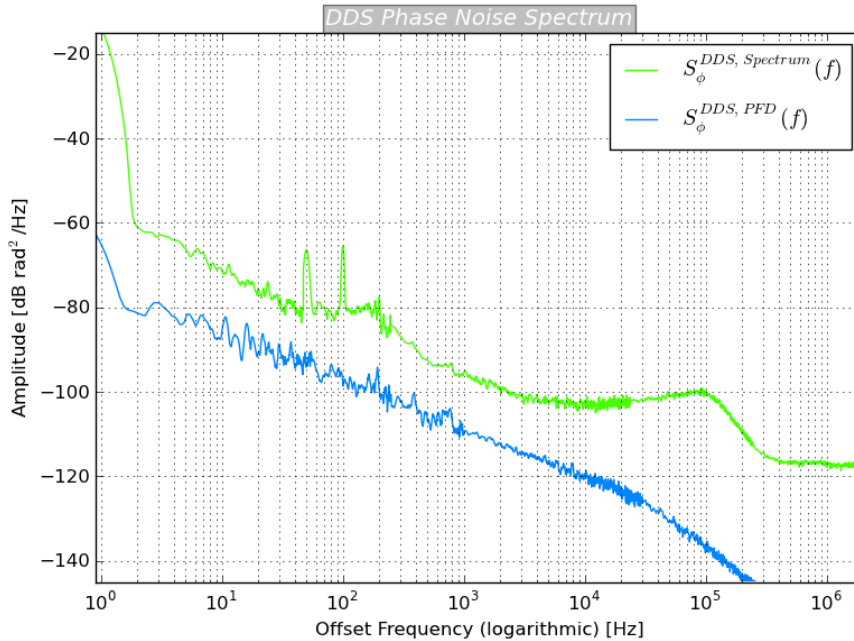
The measurement $S_{\phi}^{DDS, Spectrum}(f)$ is shown in figure 5.15. The observed spectrum has the shape of the dynamic range, which can be found in the datasheet of the used spectrum analyzer (Agilent N9010A). The dynamic range gives the smallest signal that is observable on the spectrum analyzer when a strong carrier is present. When the spectrum method is used it has to be verified that the observed signal lies significantly above the dynamic range limit, otherwise the measurement method does not give valid results.

The relative phase noise between the reference channels can be measured by using them as LO and RF input for the PFD. The measured rms noise values is composed of the rms phase noise of each single channel as

$$\langle\phi\rangle_{DDS} = \sqrt{\langle\phi^2\rangle_{ref\ 1} + \langle\phi^2\rangle_{ref\ 2}}.$$

The measurement is shown in figure 5.15

Figure 5.15 $S_{\phi}^{DDS, Spectrum}(f)$ shows the spectrum of one DDS channel on the spectrum analyzer. The function follows the dynamic range, which can be found in the datasheet of the used spectrum analyzer (Agilent N9010A). The relative phase noise between the reference channels is measured with the PFD method resulting in the phase noise spectrum $S_{\phi}^{DDS, PFD}(f)$.



From integration over the spectrum $S_{\phi}^{DDS, PFD}(f)$ follows a relative phase noise between the reference channels of

$$\langle\phi\rangle_{DDS} = 0.037^{\circ}.$$

When this is equally attributed to both channels, this gives a phase noise of each reference channel

$$\langle\phi\rangle_{ref\ 1} = \langle\phi\rangle_{ref\ 2} = \frac{1}{\sqrt{2}}0.037^{\circ} = 0.026^{\circ}.$$

From the datasheet [8] of the used DDS model a relative phase noise of 0.022° is expected. The slightly higher value might be attributed to the fact that the used clock signal does not have the optimum amplitude.

Relative Phase Noise of the Optical Signal to the Reference

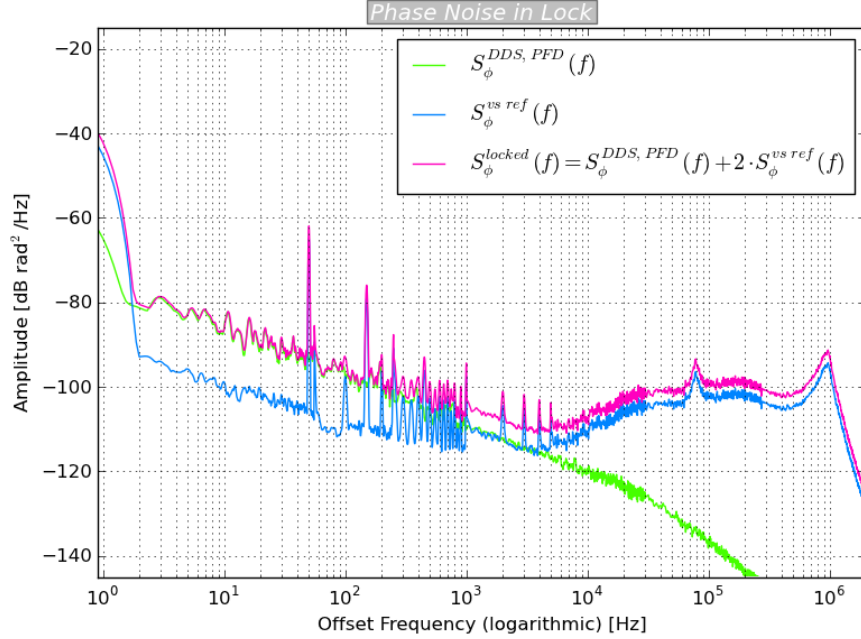
The second part of the resulting phase noise between the lattice beams is the fluctuation of each phase locked optical signal against its reference channel $S_{\phi}^{vs\ ref}(f)$. This means that the residual error signal in lock has to be monitored in the setup shown in figure 5.12.

The phase noise of the resulting signal is the relative phase noise $S_{\phi}^{DDS, PFD}(f)$ of the reference channels to each other and the fluctuation of the optical signal against each reference $S_{\phi}^{vs\ ref}(f)$. Therefore, the phase noise spectrum in lock $S_{\phi}^{locked}(f)$ is given as

$$S_{\phi}^{locked}(f) = S_{\phi}^{DDS, PFD}(f) + 2 \cdot S_{\phi}^{vs\ ref}(f).$$

The result is shown in figure 5.16.

Figure 5.16 The phase noise spectrum $S_{\phi}^{locked}(f)$ is obtained from the relative reference fluctuations $S_{\phi}^{DDS, PFD}(f)$ and the fluctuation of both optical signals against their reference $S_{\phi}^{vs\ ref}$.



From integration over the spectrum $S_{\phi}^{vs\ ref}(f)$ follows that the phase noise of the optical channels against their respective reference is $\langle\phi\rangle_{opt\ vs\ ref} = 0.7^{\circ}$.

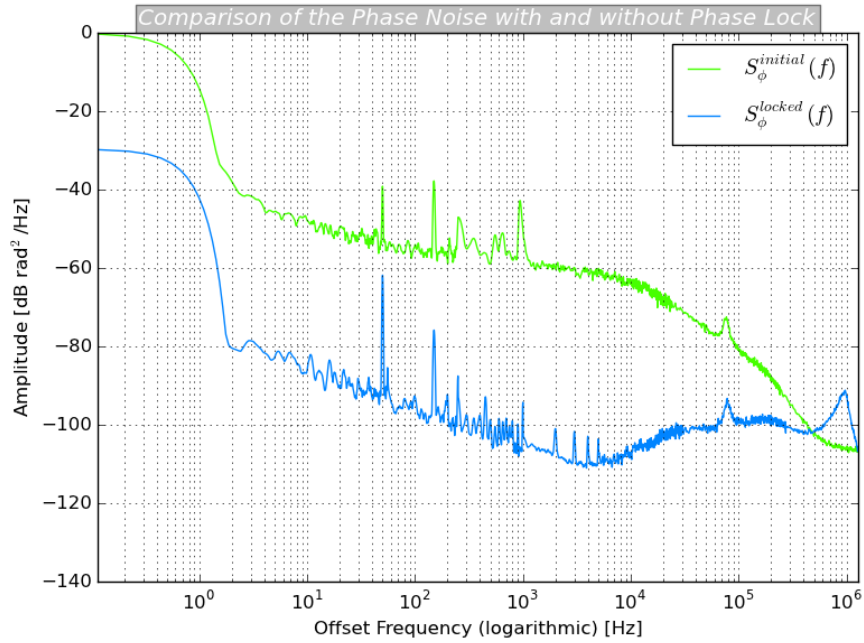
For the overall rms phase noise of the resulting signal follows an rms phase noise of

$$\langle\phi\rangle = \sqrt{\langle\phi^2\rangle_{DDS} + 2\langle\phi^2\rangle_{opt\ vs\ ref}} = 0.99^{\circ} \leq \langle\phi\rangle_{goal} = 1.7^{\circ}.$$

The obtained value for the phase noise is smaller than the estimated value for which heating processes due to displacement are suppressed.

For comparison the initial phase noise $S_{\phi}^{initial}(f)$ and the phase noise in lock $S_{\phi}^{locked}(f)$ are shown in figure 5.17.

Figure 5.17 Comparison of the initial phase noise $S_{\phi}^{initial}(f)$ to the phase noise spectrum in lock $S_{\phi}^{locked}(f)$.



The relative phase noise of about 1° between the locked beams can be compared to the values achieved with other phase lock schemes:

Phase locked loops based on a piezo mounted mirror typically reach stabilities of 3° [21]. When additionally a set of tipping Brewster windows is inserted, stabilities between $0.1 \dots 0.9^{\circ}$ can be reached [22, 37]. Regarding these values the found relative phase stability for the set up phase locked loop is acceptable.

6 | Conclusion and Outlook

Goal of the thesis was the setup and characterisation of a new scheme for state dependent transport based on the interferometrically stable overlap of two independent conveyor belts. It was estimated that a phase stability of better than $\langle\phi\rangle \approx 1.7^\circ$ degree is needed to perform experiments like a quantum walk and a single atom interferometer successfully with this setup (see section 1.2.4). Besides the relative phase stability two points that need to be investigated before a test on ultra cold atoms are

- **the intensity stabilization:** the intensity of the circular polarizations was not stabilized during this thesis. Fluctuations in the lattice beam intensity causes the trapping depth to vary and needs to be investigated.
- **the mode matching:** the rotation of the linear polarization tested in section 5.2 shows the missing mode matching between the overlapped circular polarizations.

The main point of this thesis is the test of phase stabilization and control in a prototype setup, i.e. it does not contain the ultra cold atoms.

To achieve interferometric stability and control over relative phase and frequency a phase locked loop as introduced in chapter 2 for each arm is set up. Two to each other phase stable direct digital synthesizers provide the reference signals, each for one phase locked loop. They offer the possibility to implement various phase and frequency tuning patterns. The resulting scheme for the phase stabilized superposition of the state dependent conveyor belt is shown in figure 2.7 and requirements on each element were estimated and measured.

To prevent polarization crosstalk in the phase locked loop and the resulting optical lattice the orthogonality of the lattice beams has to be ensured. Orthogonality is distorted by beam splitting elements and glass plates with an angular deviation in the alignment (see chapter 3). For creation of the error signal for the phase locked loop the orthogonally combined beams need to be splitted again in their components. A birefringent Wollaston prism with high extinction ratio compared to a coated polarizing beam splitter is used to separate the beams again (see section 3.1).

A quarterwave plate is used to create circular polarized light from the orthogonal linear polarizations. An estimation (section 3.2) for the tolerable retardance error is based on comparison of the trapping frequency variation during transport. The estimation shows that the tolerable retardance error is $\lambda/450$, which is better than the retardance error for a non-customized quarterwave plate of $\lambda/40 \dots \lambda/320$, but achievable [42].

From analysis of the system transfer function (see section 5.1) it becomes obvious that the delay time caused mainly by the signal travelling time through the AOM (see section 4.3) decreases the phase margin. The system is still stable, but the large delay prevents complete tunability which is needed to achieve the optimum step response with smaller overshoot. This is typical for the insertion of dead-time elements into a loop [23].

One way to circumvent this problem is to choose an AOM with a larger speed of sound. For instance Lithium Niobate offers a transition time through the crystal which is only

60 % of the one in Tellurium Dioxide, which was used in this case. Another and more powerful way is to insert an electronic compensation, called a Smith predictor [23, page 531].

The found similarity in the phase locked loop behaviour to a second order system (see section 5.1.4) opens a convenient way for tuning and optimization, since the response is primary determined by just two parameters.

As a result for the characterisation of the phase locked loop it can be stated, that its response is understood and can be connected to the second order transfer function resulting from the measured system parameters. It can be improved by insertion of a dead time compensation.

The quality of the phase locked loop expresses itself in the resulting phase noise suppression. Two different ways to measure the relative phase noise spectrum of the lattice beams were presented and the resulting relative phase noise between the lattice beams is approximately 1° (see section 5.3). A large part of the residual phase noise has its origin in the servo-bump feature introduced in section 2.4. Since the height of the servo-bump is dependent on the damping of the system, this value can be improved further in the same way as the step response of the system.

Nevertheless, already now the achieved phase stability is comparable to the values achieved with piezo based lock schemes. However, typical switching times for phase control in piezo based setups lie in the order of tens of milliseconds [21, 37, 16] and are therefore large compared to the switching time in the order of μs achieved in the direct synthesis setup.

Acknowledgements

Many things in this year of my master thesis in the AG Meschede happened for which I want to thank some people: First of all I want to thank Professor Dieter Meschede and Dr. Andrea Alberti for giving me such a great project as master thesis. In my feeling there were many different aspects about which I could learn something. Professor Weitz has to read all of what I learned as my second advisor and I want to thank him for spending the time for this.

One of the things I find really worth mentioning about being a master student in the AG Meschede is that one learns to present the respective project. For instance as poster at the DPG meeting in Stuttgart or just in the group meetings. I also appreciated the possibility to participate in the workshops in Munich and Bonn.

Furthermore, Professor Artur Widera and Achim Rosch gave me the chance to give a talk in their groups in Kaiserslautern and Cologne.

Besides my project, I set up the direct digital synthesizer for the Cavity QED project with Sebastian Manz and Rene Reimann and working with them till late at night was – against my expectation regarding working at night– really nice.

Thanks to Fien Latumahina, Ilona Jaschke and Annelise von Rudloff-Miglo for organizing everything from orders over pencils to thesis printing and especially for the institute away-day where we visited Zeche Zollverein together.

The proof-reading of parts of my thesis by Andreas Steffen, Tobias Kampschulte, Rene Reimann, Carsten Robens and Stefan Brakhane were done in such an attentive way that I hope all unprotected \LaTeX blanks have been found. Thanks to Dr. Wolfgang Alt for his direct way of pointing out kick-able sections of the thesis.

A | Stitching Phase Noise Spectra for Different Resolution Bandwidth

Displayed by the spectrum analyzer is the average power found in a frequency interval of width $\sim P_{\text{average}}/\text{RBW}$. Since the resolution bandwidth changes from spectrum to spectrum, the spectra are always referenced to a certain RBW value.

The used Frequency Span S , resolution bandwidth RBW and number of recorded points $\#$ are connected by a constant k

$$\# = k \cdot \frac{S}{\text{RBW}}.$$

In the end each data point represents a frequency interval $S/\#$ and the spectrum analyzer will choose the respective resolution bandwidth RBW which is optimized for the chosen span, such that the spectrum can be acquired in the minimum time with optimized information content. In case of the Agilent N9010A the factory preset is ~ 1000 points. This value can be changed to from 1 – 40 000 points. Nevertheless, since RBW, $\#$ and S are connected, the spectrum analyzer is used with its auto-settings for a chosen span.

Figure A.1 Several spectra with different resolution bandwidth/ spans are recorded. The Gaussian filter used by the spectrum analyzer is clearly visible in the logarithmic scale.

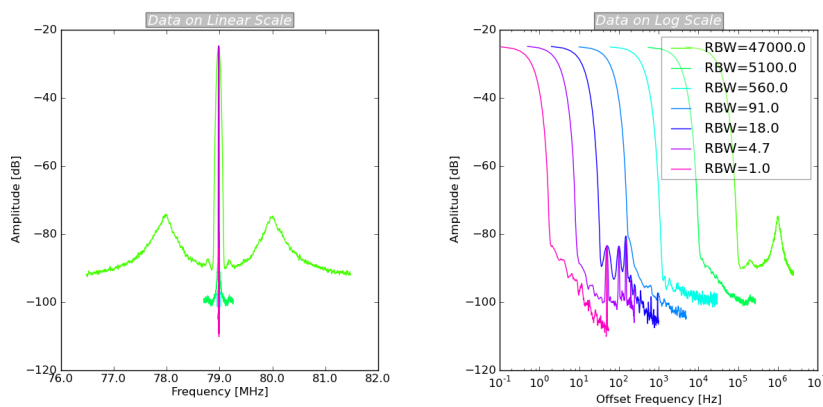


Figure A.2 To obtain the average power in a 1 Hz bandwidth, the measured spectra are normalized to the respective RBW value.

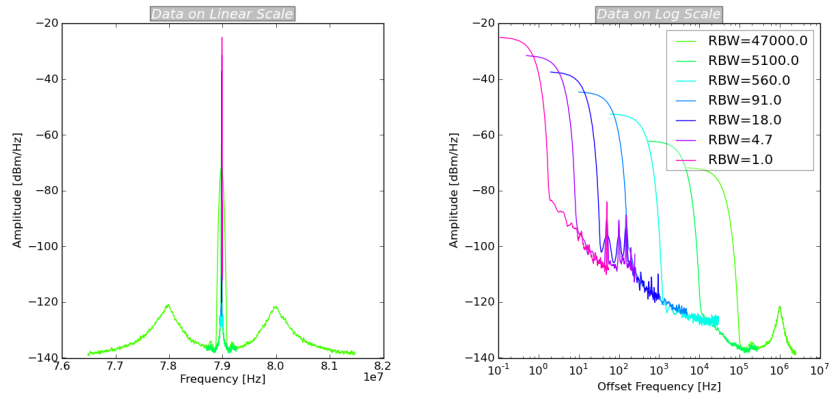
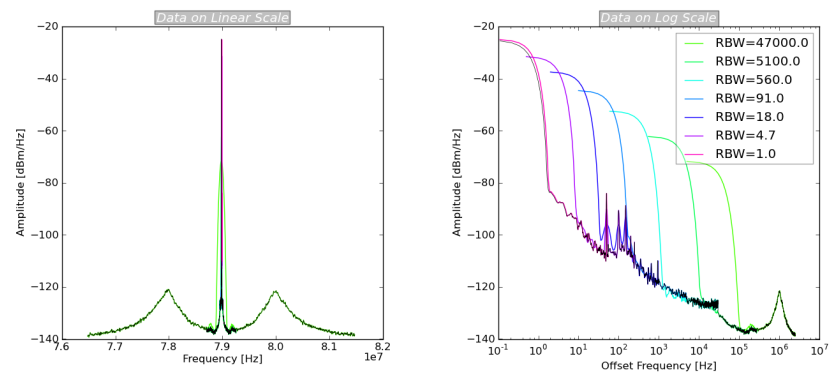


Figure A.3 Now a stitched function can be found, that begins at the data with the largest span and jumps to the data track with the higher resolution as soon as it is available, till it reaches the curve with 1 Hz resolution bandwidth. This function can be used for further analysis.



Bibliography

- [1] Y Aharonov, L. Davidovich, and N. Zagury. Quantum random walks. *Physical Review A*, 48(2):1687, 1993.
- [2] Stephen Alexander. *Optical Communication Receiver Design*. SPIE - The International Society for Optical Engineering, 1997.
- [3] D W Allan. Time and frequency (time-domain) characterization, estimation, and prediction of precision clocks and oscillators. *IEEE Transactions on Ultrasonics, Ferroelectrics and Frequency Control*, 34(6):647–654, 1987.
- [4] AOM. Application note – modulator model 3000 series. Technical report, Crystal Technologies.
- [5] Andrew M Childs, David Gosset, and Z A K Webb. Universal computation by multi-particle quantum walk. *arXiv*, pages 1–54, 2012.
- [6] G De Las Cuevas, W Dür, M Van Den Nest, and M A Martin-Delgado. Quantum algorithms for classical lattice models. *New Journal of Physics*, 13(9):21, 2011.
- [7] Datasheet. Acousto-optical modulator Model 3080-122. Technical report, Crystal Technologies.
- [8] Datasheet. Direct Digital Synthesizer AD9954. Technical report, Analog Devices.
- [9] Datasheet. PFD Chip MC100EP140. Technical report, ON Semiconductor.
- [10] Ivan H Deutsch, Gavin K Brennen, and Poul S Jessen. Quantum Computing with Neutral Atoms in an Optical Lattice. *Fortschritte Der Physik*, 48(9-11):925–943, 2000.
- [11] Richard P Feynman. Simulating Physics with Computers. *International Journal of Theoretical Physics*, 21:467–488, 1982.
- [12] William (Case Western Reserve University Dept. of Physics) Fickinger. A Michelson-Morley Centennial Symposium. *Modern physics in America*, 1987.
- [13] Leonid Förster. *Microwave control of atomic motion in a spin dependent optical lattice*. Phd thesis, University of Bonn, 2010.
- [14] Sebastian Hild. *Resolved Raman sideband cooling in a doughnut-shaped optical trap*. Master thesis, University of Bonn, 2011.
- [15] J D Jackson. *Classical Electrodynamics*, volume 67. Wiley, 1999.
- [16] Gregor Jotzu, Tim J Bartley, H B Coldenstrodt-Ronge, Brian J Smith, and Ian A Walmsley. Continuous phase stabilization and active interferometer control using two modes. *arXiv11011906J*, page 3, 2011.

- [17] Michał Karski, Leonid Förster, Jai-Min Choi, Andreas Steffen, Wolfgang Alt, Dieter Meschede, and Artur Widera. Quantum Walk in Position Space with Single Optically Trapped Atoms. *Science*, 325(5937):7, 2009.
- [18] Michał Karski. *State-selective transport of single neutral atoms Michał Karski*. Phd thesis, University of Bonn, 2010.
- [19] Julia Kempe. Quantum random walks - an introductory overview. *Contemporary Physics*, 44(4):20, 2003.
- [20] VE Korepin and FHL Essler. Exactly solvable models of strongly correlated electrons. *arXiv*, pages 1–8, 1994.
- [21] Vishnu Vardhan Krishnamachari, Esben Ravn Andresen, Søren Rud Keiding, and Eric Olaf Potma. An active interferometer-stabilization scheme with linear phase control. *Optics Express*, 14(12):5210–5215, 2006.
- [22] Guo-Wei Li, Sheng-Jhe Huang, Hsu-Sheng Wu, Shiang Fang, De-Sheng Hong, Tarek Mohamed, and Dian-Jiun Han. A Michelson Interferometer for Relative Phase Locking of Optical Beams. *Journal of the Physical Society of Japan*, 77(2):024301, January 2008.
- [23] Jan Lunze. *Regelungstechnik 1*. Springer, 7. neu bea edition, 2008.
- [24] L S Ma, P Jungner, J Ye, and J L Hall. Delivering the same optical frequency at two places: accurate cancellation of phase noise introduced by an optical fiber or other time-varying path. *Optics letters*, 19(21):1777–9, November 1994.
- [25] Olaf Mandel, Markus Greiner, Artur Widera, Tim Rom, Theodor W Haensch, and Immanuel Bloch. Coherent transport of neutral atoms in spin-dependent optical lattice potentials. *Physical Review Letters*, 91(1):4, 2003.
- [26] Olaf Mandel, Markus Greiner, Artur Widera, Tim Rom, Theodor W Hänsch, and Immanuel Bloch. Controlled collisions for multi-particle entanglement of optically trapped atoms. *Nature*, 425(6961):937–940, 2003.
- [27] H J Metcalf and P Van Der Straten. Laser cooling and trapping of atoms. *Journal of the Optical Society of America B*, 20(5):887, 2003.
- [28] C W Nelson, A Hati, D A Howe, and Senior Member. Common-Arm Counterpropagating Interferometer for Measurement of Vibration-Induced Noise in Fibers. *IEEE Photonics Technology Letters*, 23(21):1633–1635, 2011.
- [29] Katsuhiko Ogata. *Modern Control Engineering*, volume 17. Prentice Hall, 2001.
- [30] M. Bass (Editor) Optical Society of America (Author). *Handbook of Optics (II): Devices, Measurements, and Properties*, 1995.
- [31] M Prevedelli, T Freearde, and T W Hänsch. Phase locking of grating-tuned diode lasers. *Appl Phys B*, 60(2):241, 1995.
- [32] Fritz Riehle. *Frequency Standards*. WILEY-V C H VERLAG GMBH, Weinheim, 2004.
- [33] Dominik Schrader, Stefan Kuhr, Wolfgang Alt, and M Martin. An optical conveyor belt for single neutral atoms. *arXiv*, 2001.

- [34] R P Scott, C Langrock, and B H Kolner. High-dynamic-range laser amplitude and phase noise measurement techniques, 2001.
- [35] Spec. Sheet. Photodetector PDA10A. Technical Report 973, Thorlabs, 2011.
- [36] Jacob F Sherson, Christof Weitenberg, Manuel Endres, Marc Cheneau, Immanuel Bloch, and Stefan Kuhr. Single-atom-resolved fluorescence imaging of an atomic Mott insulator. *Nature*, 467(7311):68–72, 2010.
- [37] Bor-Wen Shiau, Tzu-Ping Ku, and Dian-Jiun Han. Real-Time Phase Difference Control of Optical Beams Using a Mach–Zehnder Interferometer. *Journal of the Physical Society of Japan*, 79(3):034302, March 2010.
- [38] Andreas Steffen, Andrea Alberti, Wolfgang Alt, Noomen Belmechri, Sebastian Hild, Michał Karski, Artur Widera, and Dieter Meschede. Digital atom interferometer with single particle control on a discretized space-time geometry. *Proceedings of the National Academy of Sciences of the United States of America*, 109(25):9770–4, June 2012.
- [39] Leticia Tarruell, Daniel Greif, Thomas Uehlinger, Gregor Jotzu, and Tilman Esslinger. Creating, moving and merging Dirac points with a Fermi gas in a tunable honeycomb lattice. *Nature*, 483(7389):302–305, 2012.
- [40] Philipp Treutlein, Tilo Steinmetz, Yves Colombe, Benjamin Lev, Peter Hommelhoff, Jakob Reichel, Markus Greiner, Olaf Mandel, Arthur Widera, Tim Rom, Immanuel Bloch, and Theodor W Hänsch. Quantum Information Processing in Optical Lattices and Magnetic Microtraps. *Fortschritte Der Physik*, 54(8-10):15, 2006.
- [41] VCO. Voltage controlled oscillator, Application note. Technical Report 4, mini circuits.
- [42] Waveplate. Precision Photonics.
- [43] D J Wineland and W M Itano. Laser cooling of atoms. *Physical Review A*, 20(4):1521–1540, 1979.

Erklärung der Selbstständigkeit

I hereby certify that the work presented here was accomplished by myself and without the use of illegitimate means or support, and that no sources and tools were used other than those cited.

Bonn, Oktober 14th, 2012

Anna Hambitzer